

Electronic Transport in Quantum Matter Systems

Dissertation

zur

Erlangung der naturwissenschaftlichen Doktorwürde
(Dr. sc. nat.)

vorgelegt der

Mathematisch-naturwissenschaftlichen Fakultät

der

Universität Zürich

von

Daniel Destraz

von

Basel BS

Promotionskommission

Prof. Dr. Johan Chang (Vorsitz und Leitung der Dissertation)

Prof. Dr. Andreas Schilling

Dr. Benoît Fauqué

Zürich, 2020

Abstract

The research of different materials and their properties is a central part of modern physics and materials science. Our modern technology would be unthinkable without the enormous variety of phenomena in solids. These phenomena are of different kinds such as electronic, thermal, optic, and mechanical. They are mostly based on quantum mechanical properties, i.e. properties of the basic building blocks such as electrons, atoms, and photons. In the present work investigations into multiple such quantum phenomena are presented, in which the focus is set on transport properties.

In thin superconducting films the region around the critical transition is strongly influenced by superconducting fluctuations. In thin NbN films it could be shown how the superconducting fluctuations influence the Hall effect and cause a sign change in the Hall resistance. At the other extreme of the phase diagram under very high magnetic fields and at lowest temperatures a quantum phase transition could be shown. In even thinner films the appearance of the pseudogap and of topological vortex pair separations leads to even more extensive behaviour and multiple sign changes in the Hall resistance. Thin films of NbN with their similarity to cuprate high temperature superconductors are good candidates to learn more about the still enigmatic properties of the cuprates, especially the pseudogap.

In the material $\text{Ca}_{1.8}\text{Sr}_{0.2}\text{RuO}_4$ the proof for a quantum critical point could be established, in contrast to earlier publications. With this a connection to the related material $\text{Sr}_3\text{Ru}_2\text{O}_7$ could be made. Further parallels to the structurally identical superconductor Sr_2RuO_4 complete the picture.

In the topological semimetal PrAlGe the influence of the Berry curvature on the Hall and Nernst effects was investigated. Here it could be shown that the topological influences in absence of a magnetic field are hidden due to the formation of domains. After the application of a magnetic field the anomalous transport properties emerge for which an excellent agreement with theoretical calculations could be shown.

Zusammenfassung

Das Erforschen verschiedener Materialien und ihrer Eigenschaften ist ein zentraler Bestandteil der modernen Physik und Materialwissenschaften. Unsere moderne Technologie wäre ohne die enorme Vielfalt an Phänomenen in Festkörpern undenkbar. Diese Phänomene sind verschiedenster Natur, wie beispielsweise elektronisch, thermisch, optisch und mechanisch. Sie basieren dabei meistens auf quantenmechanischen Eigenschaften, d.h. Eigenschaften der grundlegenden Bausteine wie Elektronen, Atomen und Photonen. In der vorliegenden Arbeit werden Untersuchungen zu verschiedenen solcher Quantenphänomenen aufgezeigt, wobei das Hauptaugenmerk auf deren Transporteigenschaften liegt.

In dünnen supraleitenden Filmen ist die nähere Umgebung des kritischen Übergangs stark beeinflusst durch supraleitende Fluktuationen. In dünnen NbN-Filmen konnte gezeigt werden, wie die supraleitenden Fluktuationen den Hall-Effekt beeinflussen und dabei zu einem Vorzeichenwechsel des Hall-Widerstandes führen. Am anderen Extrem des Phasendiagramms, unter sehr hohen Magnetfeldern und bei tiefsten Temperaturen, konnte ein Quantenphasenübergang gezeigt werden. In noch dünneren Filmen führt das Auftreten der Pseudolücke und von topologischen Vortex-Paar-Separationen zu noch umfangreichem Verhalten und mehreren Vorzeichenwechseln des Hall-Widerstandes. Dünne Filme aus NbN sind mit ihrer Ähnlichkeit zu Kuprat-Hochtemperatur-Supraleitern gute Kandidaten, um mehr über die immer noch rätselhaften Eigenschaften der Kuprate zu lernen, insbesondere innerhalb der Pseudolücke.

Im Material $\text{Ca}_{1.8}\text{Sr}_{0.2}\text{RuO}_4$ gelang im Gegensatz zu früheren Veröffentlichungen der Nachweis eines quantenkritischen Punktes. Damit konnte ein Bezug zum verwandten Material $\text{Sr}_3\text{Ru}_2\text{O}_7$ hergestellt werden. Weitere Parallelen zum strukturgleichen Supraleiter Sr_2RuO_4 vervollständigen das Bild.

Im topologischen Halbmetall PrAlGe wurde der Einfluss der Berry-Krümmung auf den Hall- und Nernst-Effekt untersucht. Dabei konnte gezeigt werden, dass die topologischen Einflüsse in der Abwesenheit eines Magnetfeldes aufgrund von Domänenbildung versteckt sind. Nach dem Anlegen eines Magnetfeldes treten die anomalen Transporteigenschaften hervor, wobei eine ausgezeichnete Übereinstimmung mit theoretischen Berechnungen gezeigt werden konnte.

Contents

Abstract	iii
Zusammenfassung	v
List of Abbreviations	xi
List of Symbols	xiii
Latin Symbols	xiii
Greek Symbols	xv
1 Introduction to Quantum Matter	1
1.1 Materials Research	1
1.2 Quantum Criticality	2
1.3 Superconductivity	5
1.3.1 High-Temperature Superconductors	5
1.3.2 Superconducting Fluctuations	9
1.4 Topological Effects	10
1.4.1 Weyl Semimetals	10
1.4.2 BKT Transition	13
1.5 Scope of the Thesis	14
2 Methods and Models	15
2.1 Resistivity and Hall Effect	15
2.1.1 Measurement Procedure	15
2.1.2 Making Electrical Contacts	18
2.1.3 Drude Model	18
2.1.4 Sommerfeld Model	19
2.1.5 Ordinary Hall Effect	21
2.1.6 Anomalous Hall Effect	22
2.2 Nernst and Seebeck Effect	23
2.3 Magnetometry	26

2.3.1	Overview	26
2.3.2	SQUIDs	27
2.3.3	AC Magnetization	28
2.4	Cryostats	29
2.5	X-Ray Diffraction: Laue Method	30
2.6	Models for Superconducting Fluctuations	31
3	Hall Effect Study of the Superconducting Fluctuations in a Thin Film of NbN	35
3.1	Introduction	35
3.2	Methods	37
3.3	Experimental Results	38
3.4	Discussion	45
3.5	Conclusions	50
4	Superconducting Fluctuations in Ultrathin NbN Films	51
4.1	Introduction	51
4.2	Methods	53
4.3	Results and Discussion	54
4.4	Conclusions	60
5	High-Field Electronic Transport in NbN Films	63
5.1	Introduction	63
5.1.1	Quantum Critical Scaling	63
5.1.2	Superconducting Fluctuations	65
5.2	Methods	66
5.3	Results and Discussion	67
5.3.1	Quantum Critical Scaling	67
5.3.2	Alternative View on the Transition	70
5.3.3	Hall Effect	71
5.4	Conclusions	73
6	Observation of a Quantum Critical Point in $\text{Ca}_{1.8}\text{Sr}_{0.2}\text{RuO}_4$	75
6.1	Introduction	75
6.2	Methods	81
6.3	Results and Discussion	81
6.4	Conclusions	90
7	Magnetism and Topological Effects in PrAlGe	91
7.1	Introduction	91
7.2	Methods	94

7.3	Results on Transport and Magnetism	95
7.3.1	Resistivity, Hall, DC Magnetization, Seebeck, and Nernst . .	95
7.3.2	Magnetoresistance	101
7.3.3	AC Magnetization	103
7.4	Theoretical Results	105
7.5	Neutron Scattering	108
7.6	Discussion	110
7.7	Conclusion	116
8	Summary and Outlook	117
	Acknowledgements	119
	Publications	121
	Bibliography	123

List of Abbreviations

AC	alternating current
ACMS	AC Measurement System (by Quantum Design)
AL	Aslamazov-Larkin
ARPES	angle-resolved photoemission spectroscopy
BCS	Bardeen-Cooper-Schrieffer
BEC	Bose-Einstein condensate
BKT	Berezinskii-Kosterlitz-Thouless
CDW	charge density wave
DC	direct current
DOS	density of states
FC	field cooled
MPMS	Magnetic Property Measurement System (by Quantum Design)
MT	Maki-Thomson
PND	powder neutron diffraction
PPMS	Physical Property Measurement System (by Quantum Design)
PSI	Paul Scherrer Institute
QCP	quantum critical point
QP	quasiparticle
QPT	quantum phase transition
SANS	small angle neutron scattering
SC	superconducting
SDW	spin density wave
SOC	spin-orbit coupling
SQUID	superconducting quantum interference device
WHH	Werthamer-Helfand-Hohenberg
ZFC	zero field cooled

List of Symbols

Latin symbols

A	cross section or multiplicative factor
B	(external) magnetic field
B^*	ghost critical field
B_c	critical field
B_{c2}	upper critical field
B_s	saturation field
D	diffusion constant
d	thickness
E	electrical field
e	elementary charge, 1.602×10^{-19} C, or Euler's number
E_F	Fermi energy
f	Fermi-Dirac distribution
Gi	Ginzburg-Levanyuk number
H	magnetizing field
h	Planck constant, 6.626×10^{-34} J s, or height
\hbar	reduced Planck constant, 1.055×10^{-34} J s
I	electric current
j	electric current density
\vec{k}	reciprocal space vector
k_B	Boltzmann constant, 1.381×10^{-23} J K $^{-1}$
k_F	Fermi wave-vector
l	length
ℓ	mean free path
ℓ_B	magnetic length
M	magnetization
m	mass or magnetic moment

N	Nernst signal or density of states
N^A	anomalous Nernst signal
n	charge carrier density or integer number
p	charge carrier density of positive charge carriers
\vec{p}	momentum
q	charge
\vec{q}	scattering vector
R	resistance
R_{\square}	sheet resistance
R_H	Hall coefficient
S	Seebeck signal
T	temperature
t	time or $T^{-1/z\nu}$
T^*	pseudogap temperature
T_{BKT}	Berezinskii-Kosterlitz-Thouless temperature
T_c	critical temperature
T_F	Fermi temperature
T_g	glass transition temperature
V	voltage or volume
v	velocity
v_F	Fermi velocity
w	width
z	dynamical exponent

Greek Symbols

α	thermoelectric tensor or dimensionless number
β	dimensionless factor
ϵ	$= \ln(T/T_c)$, or energy
Θ	Debye temperature
Θ_H	Hall angle
Θ_R	Debye temperature obtained from resistivity measurements
κ	heat conductivity tensor or $-\mathrm{d} \ln(T_c)/\mathrm{d}\mu$
λ	wavelength or electron-phonon coupling constant
μ	mobility or chemical potential
μ_B	Bohr magneton, $9.274 \times 10^{-24} \text{ J T}^{-1}$
μ_H	Hall mobility
ν	Nernst coefficient or correlation length exponent
ν_H	$= \Delta\sigma_{xy}/B$
ξ	correlation length
π	ratio of a circle's circumference to its diameter
ρ	resistivity
ρ_0	zero temperature resistivity
ρ_{xx}	longitudinal resistivity
ρ_{xy}	transverse (Hall) resistivity
ρ_{xy}^A	anomalous Hall resistivity
σ	conductivity or spin
σ_{xx}	longitudinal conductivity
σ_{xy}	transverse (Hall) conductivity
σ_{xy}^A	anomalous Hall conductivity
τ	correlation time or mean life time or time constant
χ	magnetic susceptibility
Ω	Berry curvature
ω	angular frequency
Ω_c	cyclotron frequency
ω_c	cyclotron frequency

Chapter 1

Introduction to Quantum Matter

The topic of this thesis covers different areas of materials research. It focuses on transport properties, especially the Hall effect. All materials investigated can be considered to be quantum materials, which means that their properties can only be understood through quantum physics. For this reason the first chapter gives a broader overview and an introduction to different concepts of condensed matter physics with a focus on what is relevant for later chapters of this thesis. Any mathematical equations are avoided and left for later chapters.

1.1 Materials Research

A big factor in the advancement of human civilization has been the discovery and mastery of new materials and the understanding of new effects and behaviours in materials, which often lead to new technological innovations. This is so important that entire archaeological ages are named after the most advanced materials used. From the stone age, where wood, stones, and animal parts were used to make tools, clothes, and weapons to the Bronze Age and the Iron Age, where humans learned to use metals to make tools and weapons. This development has in modern times also been reflected in the awarding of many Nobel prizes for the discoveries of new materials and new material properties. More modern developments lead to the widespread use of computers and related gadgets such as cell phones. Certain discoveries could quickly be used in applications, such as the giant magnetoresistance which is used in the read heads of hard disks. Other discoveries, such as graphene, still await their industrial scale utilization.

The greatest leap forward in our understanding of materials came through quantum theory and its applications on electrons in crystalline lattices. It forms the basis for understanding the differences of insulator and metals and their varia-

tions in the form of semiconductors or semimetals, essential factors in our modern technology.

Many modern challenges require new technologies based on novel electronic properties. In order to combat climate change, renewable energies from solar or wind based power generation needs to be stored in batteries. In computer technology, great efforts are being made to build quantum computers. These computers are based on quantum effects such as superposition of quantum states, to solve certain problems much faster than a traditional electronic computer.

Currently some of the main focuses on materials research are in the areas of superconductivity, materials with strongly correlated electrons, and topological materials.

1.2 Quantum Criticality

The concept of phase transitions originates from thermodynamics. Such phase transitions take place at finite temperatures and are driven by changes in a control parameter such as temperature, magnetic field, pressure, or doping. Examples are plentiful, such as the every day experience of freezing or boiling water, to more abstract concepts like the superconducting transition or the appearance of an ordered ferromagnetic state upon reduction in temperature in certain materials. Such phase transitions are linked to the destruction of an order state. Quantum phase transitions are phase transitions occurring at $T = 0$. They originating purely from quantum mechanics due to competing phases of the ground state [1]. In a quantum phase transition (QPT) it is quantum fluctuations linked to Heisenberg's uncertainty principle that destroy the ordered phase. Ordered phases can be described by an order parameter, which is finite in the ordered phase and zero in the disordered state. A clear example is the magnetization in ferromagnets. For other phase transition, it is sometimes very difficult to find the order parameter. Like classical phase transitions, QPTs can be of different order. QPTs of first order, with an abrupt change in properties, are less interesting than the transitions of higher order, also termed continuous transitions with influences extending in a large area of the phase diagram. In this section we discuss mainly the continuous transitions.

Figure 1.1 shows two schematics for the two types of possible quantum critical points (QCPs), illustrated as red dots. The QPT occurs for zero temperature at the end of an ordered phase (blue). This ordered phase is either present only at $T = 0$ (left panel) or in an extended region in the phase diagram (right panel). In the first case, no phase transition can ever be observed experimentally, as zero temperature can not be reached. In the second region the classical part of the phase transition

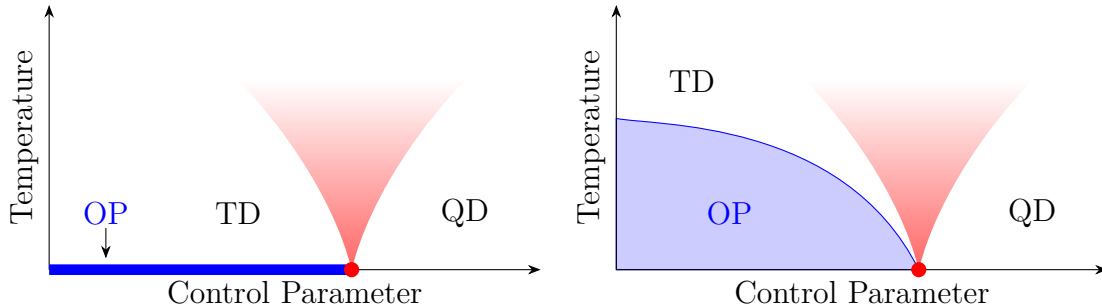


Fig. 1.1 Illustration of the position of a quantum critical point (red dot) at the end of an ordered phase (OP, blue) and the quantum critical region in which its effects extend (red shaded region). The ordered phase can either be a pure $T = 0$ ground state (left panel) or an extended phase (right panel). The regions outside the quantum critical region are either thermally disordered (TD) or quantum disordered (QD). Adapted from Ref. [1].

can be reached, depending on the temperature range available in the measurement setup, and the QCP is the unreachable endpoint of the finite-temperature classical phase transition. The region of the phase diagram in which influences of the QCP can be measured is shaded in red. Depending on the material this region can be narrower or wider [2]. Outside of the quantum critical region and the ordered phase, the system is influenced by either thermal disorder or quantum disorder for two sides of the QCP. These two regimes also indicate how the ordered phase is destroyed. In the case of thermal disorder, thermal fluctuations of the order parameter can be observed. In the case of quantum disorder, the fluctuations observed are quantum fluctuations of the order parameter. In this regime the system at finite temperature and at absolute zero are very similar.

In the quantum critical region, both the thermal and quantum fluctuations are of significance. Experimentally it is characterized by power law behaviour of quantities such as the correlation length ξ and the correlation time τ as well as observables like the heat capacity. This region is also governed by non-Fermi liquid behaviour. An example of this is shown in figure 1.2. Fermi liquid behaviour is found to the left and right of the QCP, while at the QCP a strong deviation is observed. This is indicated by the exponent ϵ in $\rho \propto T^\epsilon$, which has the Fermi liquid value of 2 away from the QCP while in the quantum critical region influenced by the QCP it has a value of 1.

One experimental challenge is the accessible temperature range. Since the quantum critical point is a single point residing at $T = 0$, which can experimentally never be reached, all experiments are conducted at finite temperatures and only observe the fluctuation effects in the region influenced by the QCP. All results on

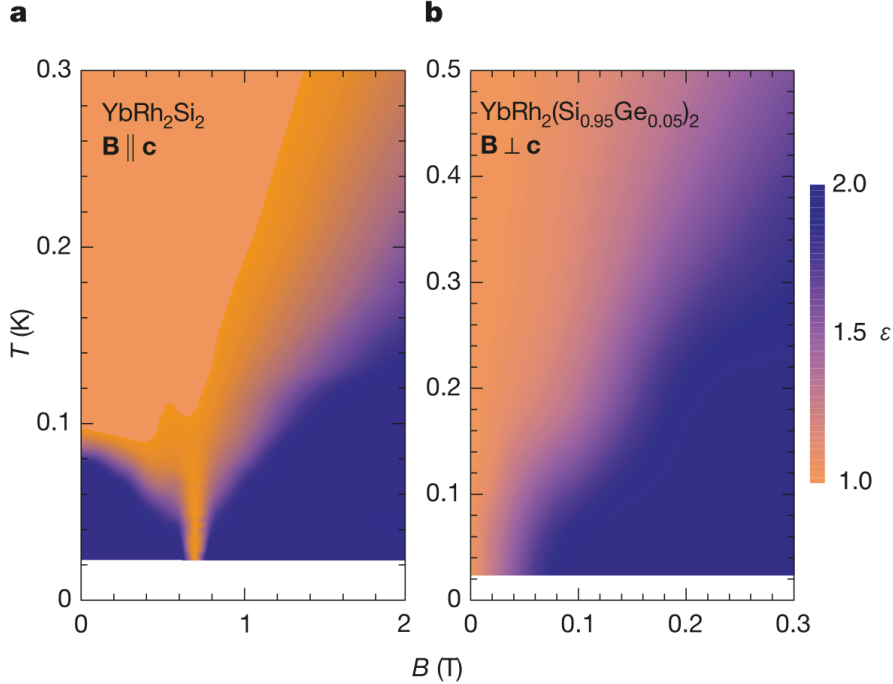


Fig. 1.2 Quantum critical behaviour of the resistivity in two heavy fermion compounds. The exponent ϵ of $\rho \propto T^\epsilon$ changes from the Fermi liquid value of 2 away from the QCP to a value of 1 at the QCP. The fan-like structure of the quantum critical region is clearly visible. Taken from Ref. [2].

the QCP itself are thus only extrapolations to zero temperature. In the case of an ordered phase for $T = 0$ only, the observations of a quantum critical region is the only way of gathering experimental evidence of such an unreachable ordered ground state.

The fluctuations observed in the disordered state are fluctuations of the order parameter. The correlations of these fluctuations of the order parameter increase as the critical point is approached. At the QCP they diverge. In order to quantify the correlation of the fluctuations, the correlation length ξ and the correlation time τ are used. Close to the QCP ξ is the only relevant length scale and τ is the only relevant time scale. At the QCP both quantities diverge. The fluctuations are now present on all time and length scales which means the system becomes scale invariant, implying that the microscopic details of the system are irrelevant. The critical exponents describing the divergence of the relevant quantities are independent of the system under investigation and describe entire universality classes according to the symmetry of the order parameter and the dimension d of the system. This makes easy model systems very valuable for investigating entire universality classes on a simple example system.

Quantum phase transitions are linked to classical phase transitions in the way that quantum phase transitions in d dimensions can be mapped to classical phase transitions in $d + z$ dimensions, where z is the dynamic critical exponent and is often = 1. The quantum-to-classical crossover in phase transitions at nonzero temperature is thus equivalent to a dimensional crossover. Upon reaching the limit $\tau/\hbar > 1/k_B T$ the perceived dimensionality changes from $d + z$ to d . Nevertheless, quantum phase transitions and classical transitions are not the same and not all properties of a quantum system can be obtained from the classical theory.

1.3 Superconductivity

Superconductivity was discovered by Heike Kamerlingh Onnes in 1911 in his laboratory at the University of Leiden [3–6]. It is a state of matter which can carry a current without dissipation ($R = 0$) and which displays the Meissner effect as a perfect diamagnet ($\chi = -1$). The superconducting phase is limited by different parameters such as temperature, magnetic field, and current density. It is achieved by a macroscopic coherence of the electron wave function. The mechanism leading to superconductivity was described in 1957 by Bardeen, Cooper, and Schrieffer [7, 8]. This theory is termed the BCS theory after its discoverers. It describes how an attractive interaction between electrons forms Cooper pairs [9] and leads to superconductivity. In classical superconductors, this attractive interaction between electrons is mediated by phonons.

1.3.1 High-Temperature Superconductors

For a long time the known superconductors consisted of metals, of which those with relatively high T_c often contained Nb. The discovery of high temperature superconductivity in the cuprate $\text{La}_{2-x}\text{Ba}_x\text{CuO}_4$ in 1986 by K. A. Müller and J. B. Bednorz [10] thus came as a great surprise, as these ceramic materials are bad conductors. This discovery sparked a hunt for ever increasing T_c , which soon led to the discovery of YBCO. The current record T_c in a cuprate without external pressure is held by HgBaCaCuO , discovered in 1993 by A. Schilling, with its T_c of slightly above 130 K [11]. In the conventional phonon-mediated superconductors the compound MgB_2 with $T_c = 39$ K [12] is already above the limit of what was thought to be the maximum reachable T_c according to BCS theory [13]. Figure 1.3 gives an overview of the different critical temperatures of various materials.

The cuprate superconductors are located close to insulating antiferromagnetic states. Since antiferromagnetism is usually obtained from repulsive interactions between electrons, while superconductivity depends on an induced attraction be-

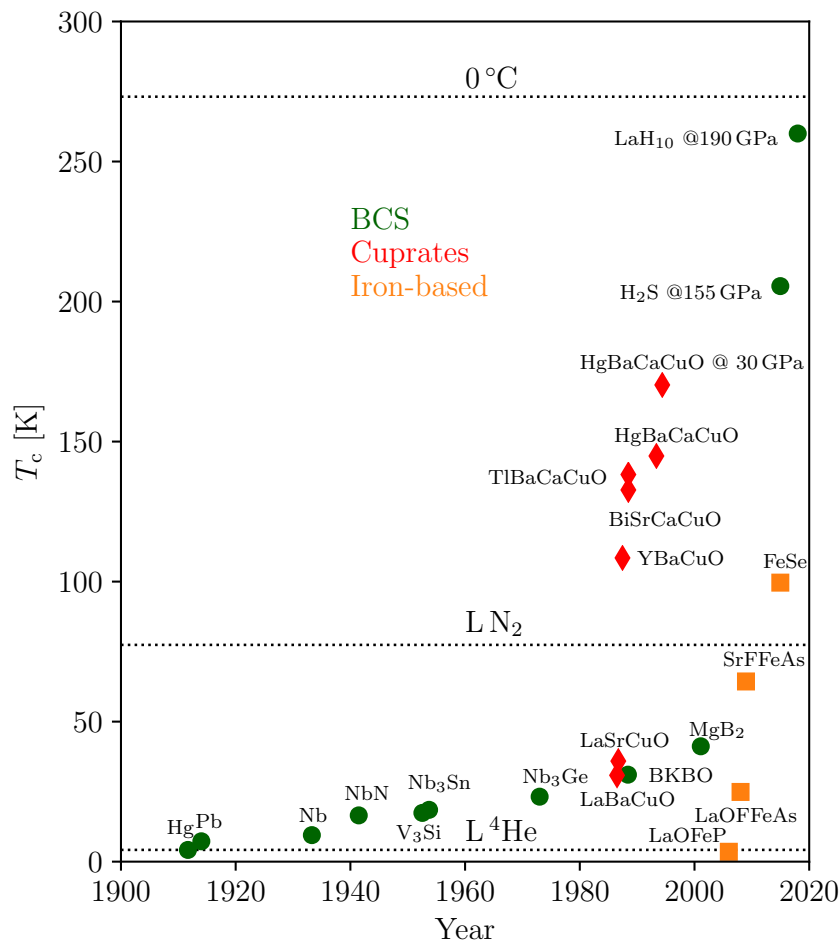


Fig. 1.3 Critical temperatures of different superconducting compounds plotted as function of the time of their discovery. Three important temperatures are indicated by dotted lines. Adapted from Ref. [14].

tween electrons in order to form Cooper pairs. This apparent paradox makes the cuprates a very interesting class of materials.

The phase diagram is shown in figure 1.4 [15] and given as a function of hole doping, which is created by changing the charge reservoir layers between the Cu-O planes. Electrons from the Cu-O layers can then move into the charge reservoir layers, thus creating holes in the Cu-O layers. The cuprates accommodate a very rich phase diagram. For low doping an antiferromagnet is found. Starting at a doping p_{\min} superconductivity emerges and remains until a doping p_{\max} after which a Fermi liquid is established. Outside the superconducting dome two interesting normal-state phases are found. The first is a so-called strange metal, which is dominated by strong electron correlations and generally not well under-

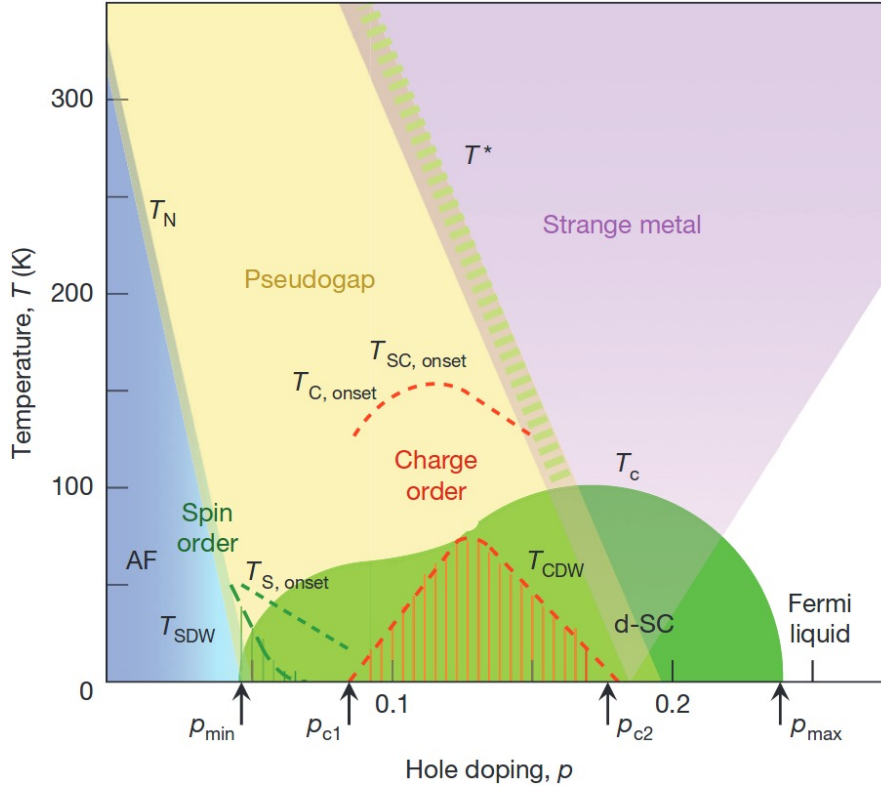


Fig. 1.4 The phase-diagram of the cuprates. The superconducting region, limited by T_c is drawn in green. The pseudogap phase (yellow), limited by T^* dominates the low doping region while a strange metal is found in the overdoped region. For very low doping, an antiferromagnetic (AF) phase is found, while for high doping a Fermi liquid is recovered. Within the pseudogap phase a small region is subject to charge density waves (CDW). Taken from Ref. [15].

stood. In resistivity measurements a linear behaviour on temperature is found up to extremely high temperatures [16]. This phase could also be connected to a quantum critical point. In the underdoped region one of the greatest puzzles in the cuprates emerges as the occurrence of the so called pseudogap phase. It extends to temperatures far above the superconducting transition and manifests itself as a depletion in the density of states which can be observed, for example, by scanning tunneling spectroscopy (STS) [17] or angle resolved photoemission spectroscopy (ARPES) [18]. Examples of STS spectra and ARPES intensities of BSCCO2212 are shown in figure 1.5. Other measurements are also capable of seeing the effects of the pseudogap, such as resistivity or Nernst effect measurements [19]. In the Fermi surface it manifests itself as Fermi arcs because of the gapped nodal regions. An explanation for the reduction of the density of states is the pairing

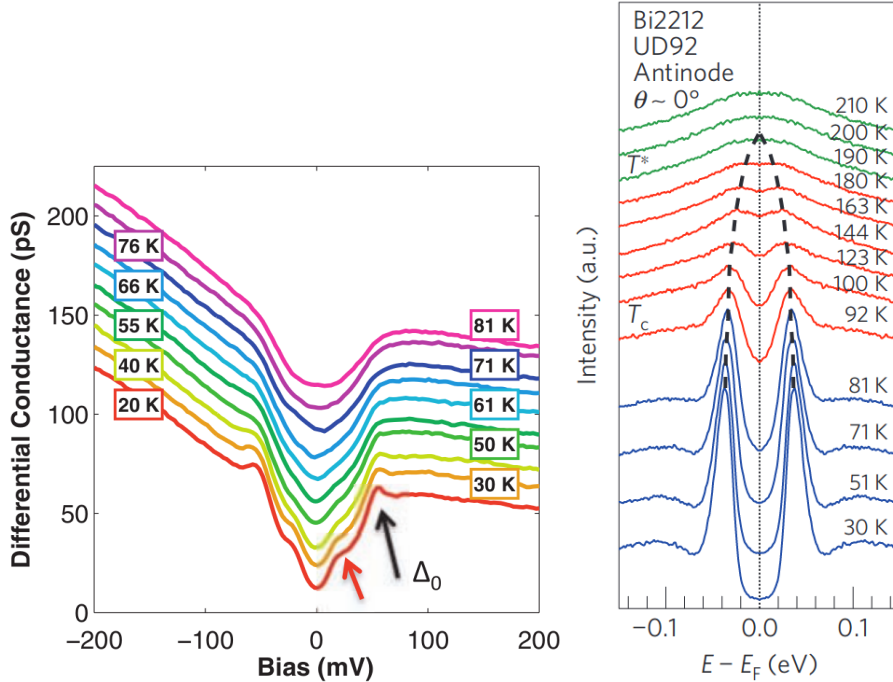


Fig. 1.5 Depletion in the density of states in the pseudogap phase in underdoped BSCCO2212 measured by STS (left panel) and ARPES (right panel). Above T_c (61 K in the left panel and 92 K in the right panel) the effect of the pseudogap is seen, extending up to much higher temperatures. Taken from Refs. [18] and [17].

of electrons into Cooper pairs. These pre-formed Cooper pairs are not yet phase coherent and do thus not yet conduct current without resistance. The pseudogap region is furthermore subject to different types of orders, such as charge order, spin order, and charge density waves, which are related to the parent compound's antiferromagnetism and Mott physics [15, 20]. The pseudogap phase thus poses many questions as to its origin and to its meaning [21].

In the end, the record for the highest T_c went back to the conventional BCS superconductors, when superconductivity with $T_c = 203$ K was discovered in sulfur hydride under very high pressure of ≈ 155 GPa [22]. This record was surpassed shortly after by lanthanum hydride with a T_c of around 250 K at pressures of ≈ 170 GPa [23, 24]. This temperature corresponds to about -23°C and room temperature superconductivity now seems again to be within grasp, at least under pressure. Despite the lost records, cuprates still offer plentiful possibilities for new discoveries and even after more than 100 years of superconductivity it is still a very active area of research. Other long standing problems in superconductivity besides the cuprates include the so-called heavy fermion superconductors discovered in

1979 [25] and the more recently discovered iron pnictides [26], another class of high-temperature superconductors next to the cuprates.

1.3.2 Superconducting Fluctuations

The superconducting transition at T_c is not a step function from the normal state resistivity to 0 but instead a gradually accelerating decrease in resistivity. In many superconductors, especially the cuprates, the transition is widened due to inhomogeneities and defects in the crystals. But even in clean materials influences of superconductivity can be seen above T_c . These influences are caused by fluctuations of superconductivity, where for a short time phase-coherent Cooper pairs exist, before they decay again. These fluctuations generate a second conduction channel, thus reducing the resistivity even above T_c . Superconducting fluctuations occur in the normal state, usually only in the vicinity of T_c , but occasionally even far from T_c [27]. A good introduction into the topic can be found in a book by Larkin and Varlamov [28].

Besides the resistivity, superconducting fluctuations can influence many different properties of a superconductor, such as the Hall effect, magnetization [29], Seebeck effect [30], and Nernst effect [30–33]. The fluctuations manifest themselves again predominantly in the smearing of the superconducting transition due to precursor effects above T_c .

Results from superconducting fluctuations can even be useful in fields beyond condensed matter physics. For example the Aslamazov-Larkin theory [34] has been used for descriptions of quark matter [35] and the superconducting fluctuations in the Nernst effect have been linked to black holes [36].

The superconducting order parameter describes superconductivity within the superconducting phase. Outside of the superconducting phase, the superconducting condensate of Cooper pairs does not exist. There are two ways in which superconductivity can be destroyed, originating from the superconducting order parameter $\psi = |\psi_0| e^{i\phi}$. The first is when the pairing amplitude $|\psi_0|$ goes to 0, in the absence of which the phase loses its meaning. In the first case the Cooper pairs exist for a short time before decaying again. During their brief existence they influence different physical properties. This case is called the amplitude fluctuating or Gaussian case. The second case is when the phase coherence of ϕ is lost while the amplitude remains finite. In this second case the Cooper pairs still exist, but can not become superconducting, except in the form of phase fluctuations in which the permanently existing Cooper pairs will gain phase coherence for a short time before losing it again. During their short lifetime these fluctuations influence again the material's normal state properties. This second case is termed phase fluctuating scenario. The observed influence on measured quantities is different to

the case of amplitude fluctuations. By investigating superconducting fluctuations one can thus learn about the mechanism that causes superconductivity and about what mechanisms destroy superconductivity above T_c .

The pseudogap is a typical region in which phase fluctuations are expected due to the pre-formed Cooper pairs, although it is not necessarily the case that the pseudogap leads to phase fluctuations. The link between the two effects is due to a low phase stiffness [37], which is linked to a low superfluid density. The superfluid density in turn decreases with decreasing T_c , as evidenced by Uemura's law [38]. A question arising from these considerations is whether superconductivity can set in at T^* if the phase can somehow be stabilized.

1.4 Topological Effects

In mathematics the field of topology considers objects to be equivalent if they can continuously be deformed into one another. An example would be that a coffee cup and a donut are the same (they both have one hole), while a muffin is different (no holes). This concept is of great use in physics, where integer numbers can be assigned to certain conceptual objects, which can be tweaked and changed only in ways that leave this integer number constant. The introduction of such topological concepts into physics was recently rewarded by awarding the 2016 Nobel prize in physics to David Thouless, Duncan Haldane, and John Kosterlitz. In recent years a lot of research has focused on topological effects in condensed matter systems. Great successes were made especially on the theoretical side while the experimental verification of the predictions is often a challenge. The most famous examples of topological materials include topological insulators, Dirac and Weyl semimetals, and topological superconductors, which are topologically different from the Bose-Einstein condensate of Cooper pairs [39]. The quantum Hall effect with its quantized conductivity plateaus is another example present in two-dimensional materials.

1.4.1 Weyl Semimetals

In the case of Dirac or Weyl semimetals, the topology originates from the electronic band structure of the material, where around certain nodes, termed Dirac or Weyl nodes, a linear dispersion relation is observed. This is similar to the two-dimensional material Graphene, which also exhibits linear dispersion around the Fermi level. The topological Dirac and Weyl semimetals are the three-dimensional analogue of Graphene.

In Weyl semimetals the Weyl points are the sources and sinks of the Berry curvature, a property equivalent to the magnetic field in momentum space. These sources and sinks correspond to Weyl points of positive and negative chirality, respectively. Weyl points of different chirality must always appear in pairs. Such Weyl points can only appear in the presence of either the breaking of time reversal symmetry or the breaking of inversion symmetry. Without such symmetry breaking, the Weyl points of different chirality are degenerate and a Dirac semimetal is obtained. The Chern number is the accumulated Berry curvature on a plane in the Brillouin zone and takes on different integer values, depending on the location of the plane with respect to the location of the Weyl nodes. In a system with two Weyl nodes the Chern number of a plane intersecting the line connecting the two nodes is 1 while the Chern number is 0 if the plane does not intersect the connecting line.

Closely related to the topological semimetals are topological insulators, which are characterized by an insulating bulk and a conducting surface, independently of the surface details. The common origin of topological insulators and semimetals is found in the band inversion [40,41] and explained in figure 1.6. The inversion of bands together with spin orbit coupling leads to an opening of an energy gap. In the case of topological insulators, the gap is present everywhere, while in the case of the semimetals the gap closes with a linear dispersion at certain points. This band inversion is what leads to the conducting surface in topological insulators and distinguishes topological insulators from ordinary band insulators that do not exhibit a band inversion. The concept of topological insulators is taken to the next level by higher order topological insulators, in which only one-dimensional edges are conducting while the bulk and the surface are insulating [42,43].

Weyl fermions were predicted in 1929 by Hermann Weyl [44] as a massless solution for the Dirac equation used in high-energy physics. All fermionic particles in nature are Dirac fermions, as no massless fermions could ever be observed. Weyl semimetals are thus a further example of the realization of theoretical possibilities of elementary particles in the form of quasiparticles in condensed matter systems.

The Weyl nodes within the bulk of a Weyl semimetal have an important effect on the surface of these materials. The projections of the Weyl nodes onto the surface are the end points of so-called Fermi arcs. These arcs are open Fermi surfaces on the surface of the sample and can be observed experimentally with ARPES. This has been shown first in TaAs [45–47]. Figure 1.7 shows experimental ARPES data on TaAs with clear Fermi arcs originating from the projections of the Weyl nodes. Scanning Tunneling Microscopy (STM) is another method of investigating the surface states [48,49], but less direct than ARPES as the Fermi arcs appear in reciprocal space while STM probes the real space.

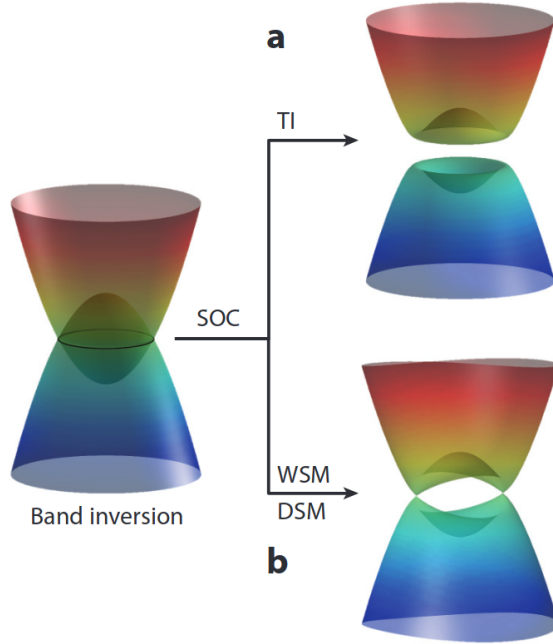


Fig. 1.6 Topological bandstructure. Band inversion and spin orbit coupling (SOC) lead to topological insulators (TI) or Weyl and Dirac semimetals (WSM and DSM), depending on whether the system is gapped everywhere or gapless in certain points. Taken from Ref. [41].

Other intriguing effects on transport properties originate from the Adler-Bell-Jackiw anomaly, or simply the chiral anomaly [50–52]. It manifests itself as a negative magnetoresistance in the case of a nonzero value of the scalar product $\vec{E} \cdot \vec{B}$, which leads to an imbalance of left and right handed electrons. This effect could be observed in the prototypical TaAs [53], which is, however, not without any doubt, as the observed phenomenon could also be explained by current jetting, an inhomogeneous current distribution [54]. The regular magnetoresistance ($\vec{E} \perp \vec{B}$) is usually expected to be positive and very high due to a large carrier mobility. Other influences on transport properties are the anomalous Hall effect and the anomalous Nernst effect, which can be very large compared to regular ferromagnets.

Weyl semimetals can be classified into type I and type II depending on whether the Lorentz symmetry is respected or not [55]. In type II Weyl-semimetals the Weyl cones are tilted such that the Fermi surface is no longer point-like. The Weyl node appears at the boundary between electron and hole pockets.

Weyl semimetals are expected to lead to useful devices in applications. The large magnetoresistance could be exploited in electronic devices. Other effects based on the spin orbit coupling and the large Berry curvature could lead to

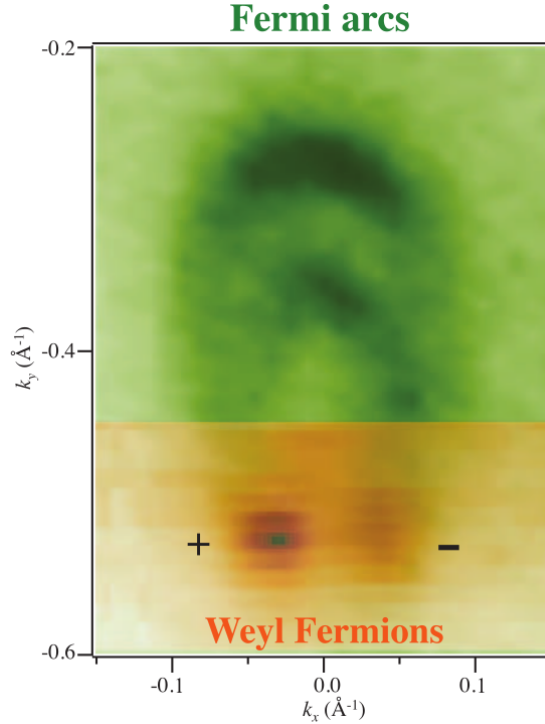


Fig. 1.7 Fermi arcs and Weyl nodes in TaAs measured using ARPES. The green color map shows the surface state Fermi surface map. The bulk Fermi surface is superimposed in orange. Taken from Ref. [45].

applications in spintronics devices. As the field of Weyl semimetal is still young, future developments, although hard to predict, are expected to be plentiful.

1.4.2 BKT Transition

Another well-established topological effect is the occurrence of a Berezinskii-Kosterlitz-Thouless (BKT) transition. Since the original works of Berezinsky [56,57] and Kosterlitz and Thouless [58,59] this theory has had a great impact on solid state physics and beyond. It is a two-dimensional phase transition in the XY-model, a spin model with $U(1)$ symmetry. The main ingredient in the BKT transition are vortex-antivortex pairs. At the phase transition, whose temperature is called T_{BKT} , these pairs are broken up into free vortices and antivortices (vortices of opposite sign). The vortex-antivortex pairs have lower energy than the free vortices, while the free vortices have higher entropy, leading to the competition of the two states. A requirement for the BKT transition is an interaction potential between vortex-antivortex pairs that is logarithmic in their separation. The BKT transition can be seen as a phase transition of infinite order, as no singularities are observed in any derivatives of thermodynamic quantities.

The vortex proliferation breaks the phase coherence of the Cooper pairs. Furthermore, separated vortices are subject to movement with an applied current in the sample, which as a dissipative process leads to a higher resistance. This vortex movement is perpendicular to the current, thus the vortices move in the direction of the Hall channel. The resistivity in this regime is then given by an exponential dependence on the temperature separation to T_{BKT} . Another test for the BKT transition is the dependence of the voltage on the current. As opposed to the standard Ohm's law the current dependence of the voltage is given by an exponent of 3 below the BKT transition and 1 above. It is furthermore marked by the superfluid density discontinuously reaching zero.

Observation of BKT transition has also been achieved in atomic gasses [60], Josephson junction arrays [61], superconducting interfaces between insulating oxides [62, 63], and liquid gated interfaces [64]. On the insulating side in the superconductor insulator transition in NbTiN films a BKT transition of charges could be observed as the duality to the vortex BKT transition on the superconducting side [65].

1.5 Scope of the Thesis

This thesis covers a range of materials exhibiting the different quantum effects introduced in this introductory chapter. After an overview of the experimental concepts and the experimental methodology in chapter 2 the investigations of this thesis are laid out. In chapters 3 and 4 the influence of superconducting fluctuations in thin films of NbN are investigated and further extended to the quantum region at very low temperatures and high fields in chapter 5. Chapter 6 describes the discovery of a quantum critical point in $\text{Ca}_{1.8}\text{Sr}_{0.2}\text{RuO}_4$ through resistivity measurements. Finally, in chapter 7 the predicted Weyl semimetal PrAlGe is investigated in detail by various techniques.

Chapter 2

Methods and Models

Research in condensed matter physics uses various techniques to investigate the different properties of interest. Of special importance are bulk measurements such as resistivity, thermoelectricity, and magnetization. In this chapter the measurement methods and apparatuses relevant for this thesis are presented. Furthermore different models for the various transport effects encountered are explained.

2.1 Resistivity and Hall Effect

2.1.1 Measurement Procedure

Ohm's law describes the relation between current and voltage as

$$V = RI, \tag{2.1}$$

where R is the resistance. Its microscopic version, independent of the sample geometry, relates the local current density and electric field through the resistivity ρ or the conductivity $\sigma = \rho^{-1}$:

$$E = \rho j \quad \text{and} \quad \sigma E = j. \tag{2.2}$$

Here the electric field and the current density can both be seen as vectors, in which case the resistivity and conductivity are tensors, each represented by a matrix which can be written as

$$\rho = \begin{pmatrix} \rho_{xx} & \rho_{xy} \\ \rho_{yx} & \rho_{yy} \end{pmatrix} \quad \text{and} \quad \sigma = \begin{pmatrix} \sigma_{xx} & \sigma_{xy} \\ \sigma_{yx} & \sigma_{yy} \end{pmatrix}. \tag{2.3}$$

Using the symmetries $\rho_{xx} = \rho_{yy}$ and $\rho_{xy} = -\rho_{yx}$ and equivalent relations for σ , which are valid for isotropic materials, this can be simplified to

$$\rho = \begin{pmatrix} \rho_{xx} & \rho_{xy} \\ -\rho_{xy} & \rho_{xx} \end{pmatrix} \quad \text{and} \quad \sigma = \begin{pmatrix} \sigma_{xx} & \sigma_{xy} \\ -\sigma_{xy} & \sigma_{xx} \end{pmatrix}. \quad (2.4)$$

As σ and ρ are the inverse elements of one another, the relation between the elements can be obtained by performing a matrix inversion and using $\sigma = \rho^{-1}$. This results in

$$\sigma_{xx} = \frac{\rho_{xx}}{\rho_{xx}^2 + \rho_{xy}^2}. \quad (2.5)$$

Usually $\rho_{xx} \gg \rho_{xy}$, which is the case for low magnetic fields or the absence of magnetic fields, and the equation simplifies to the well known formula

$$\sigma_{xx} = \frac{1}{\rho_{xx}}. \quad (2.6)$$

For the Hall component the equation becomes

$$\sigma_{xy} = -\frac{\rho_{xy}}{\rho_{xx}^2 + \rho_{xy}^2}, \quad (2.7)$$

which simplifies to

$$\sigma_{xy} = -\frac{\rho_{xy}}{\rho_{xx}^2} \quad (2.8)$$

if $\rho_{xx} \gg \rho_{xy}$. It is interesting to note here that σ_{xy} is proportional to ρ_{xy} and opposite in sign, contrary to the longitudinal case. Furthermore, in the $\rho_{xx} \gg \rho_{xy}$ case the ratio of the resistivities and conductivities is the same up to a minus sign:

$$\frac{\rho_{xy}}{\rho_{xx}} = -\frac{\sigma_{xy}}{\sigma_{xx}}. \quad (2.9)$$

The geometrical configuration used for resistivity and Hall measurements is shown in figure 2.1. The longitudinal and transverse resistances are calculated as

$$R_{xx} = \frac{V_x}{I_x} \quad \text{and} \quad R_{xy} = \frac{V_y}{I_x}. \quad (2.10)$$

It is important to connect the wires with the correct polarity. In the case of the longitudinal resistivity a sign mistake becomes obvious immediately, but in the case of the Hall resistivity both signs are possible, depending on the charge carriers. A reversed polarity might then lead to incorrect results. If done correctly, the sign of the Hall resistivity will reflect the sign of the charge carriers.

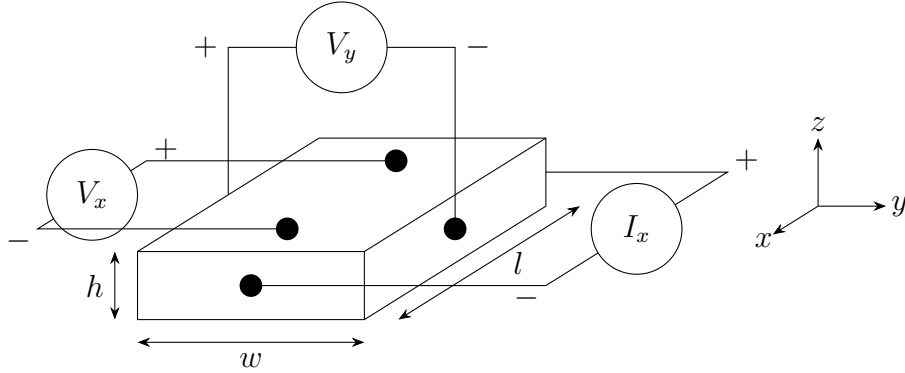


Fig. 2.1 Measurement geometry of a combined resistivity and Hall measurement. The magnetic field is usually applied in z -direction. Upon application of a current I_x , voltages V_x and V_y appear along and across the sample, respectively. Care is needed not to reverse the polarity of the V_y measurement. All negative poles point towards the positive direction of the coordinate axis, while the positive poles point towards the negative direction.

The Hall angle is a quantity used to describe the relative magnitude of the Hall and longitudinal resistivities. It is defined as the ratio of the two resistivities and, provided that $\rho_{xy} \ll \rho_{xx}$, is equal to the ratio of the conductivities:

$$\tan \Theta_H = \frac{\rho_{xy}}{\rho_{xx}} \approx \frac{\sigma_{xy}}{\sigma_{xx}}. \quad (2.11)$$

The measurement always records V and I , from which R can be calculated and subsequently converted into ρ according to

$$\rho_{xx} = R_{xx} \frac{A}{l}, \quad (2.12)$$

valid for rectangular cuboids, where $A = hw$ is the cross section through which the current flows and l is the separation of the voltage leads. The equivalent conversion for the Hall resistivity only depends on the height of the sample:

$$\rho_{xy} = R_{xy} h. \quad (2.13)$$

It is thus easier to measure the Hall effect in a thin sample than in a thick sample of the same material, as a constant material parameter ρ_{xy} implies inverse proportionality of h and R_{xy} .

2.1.2 Making Electrical Contacts

In order to connect wires to a sample, electrical contact needs to be established between the two objects. Good contacts for the samples used in this thesis typically have a resistance on the order of $1\ \Omega$ when measured with a multimeter. A further requirement is to have sufficient mechanical stability for the contacts to hold on to the sample under stress. A typical method for contacting is to use silver wires or gold wires that are soldered to the regular wires or connectors of the measurement setup on one side and glued to the sample with conducting glue, usually based on silver, on the other end. This can be in the form of silver paint, silver paste, or two component silver epoxy. Depending on the exact product used it will solidify within a few minutes at room temperature or it needs to be heated in a furnace to higher temperatures for some time. A further advantage of heating the contacts in a furnace is that some diffusion of the silver into the sample can take place which improves the resistive properties of the contacts. If no good contact is established after this process, a further way to reduce the resistance is to apply short high-voltage pulses across the contact. This often leads to very good results. Which exact process leads to the best result on a given sample is often a process of trial and error.

2.1.3 Drude Model

A simple model to describe the resistivity is the Drude model, first formulated by Drude in 1900 [66–68]. It made use of the new discovery of the electron in cathode tube experiments by J. J. Thomson in 1897 [69, 70]. The model was later extended by Hendrik Lorentz [71–73]. It assumes that the electrons can be described as a classical gas and undergo constant collisions with the atom cores.

The classical equation of motion for such a system is given by

$$m\dot{\vec{v}} = -e\vec{E} - \frac{m\vec{v}_D}{\tau}, \quad (2.14)$$

where \vec{v}_D is the drift velocity [74]. The first term on the right hand side causes the electrons to accelerate, while the second term acts as a form of friction in the opposite direction. The stationary case is obtained by setting $\dot{\vec{v}} = 0$, from which follows that

$$\vec{v}_D = -\frac{e\tau}{m}\vec{E} = -\mu\vec{E}. \quad (2.15)$$

In the second equality we introduce here the mobility $\mu = e\tau/m$. Together with $\vec{j} = nq\vec{v}_D$ one obtains

$$\vec{j} = \frac{ne^2\tau}{m}\vec{E}. \quad (2.16)$$

The comparison to equation 2.2 then yields the well known result

$$\sigma = \frac{ne^2\tau}{m}, \quad (2.17)$$

the Drude conductivity, arguably the greatest achievement of the Drude theory.

The Drude model also successfully describes related phenomena such as the Hall effect and the magnetoresistance and it partially explains the Wiedemann-Franz law. One of the biggest shortcomings of the Drude model is its strong overestimation of the electronic heat capacity.

2.1.4 Sommerfeld Model

The Sommerfeld model takes the step from the classical to the quantum gas by respecting the Pauli exclusion principle and using the correct quantum statistics, i.e. the Fermi-Dirac distribution. It was established by Sommerfeld in 1927 [75–77].

The electrons move through a crystal with an average velocity $\langle \vec{v} \rangle$. The current density j can then be written as [74]

$$\vec{j} = -en\langle \vec{v} \rangle = -en\frac{\hbar\langle \vec{k} \rangle}{m} = -e\frac{1}{V}\sum_{\vec{k},\sigma}\frac{\hbar\vec{k}}{m} \quad (2.18)$$

where the sum goes over all occupied k -vectors and spins, which is just the Fermi sphere in the case of $\vec{j} = 0$. In thermal equilibrium the k -vectors point in all directions equally with $\langle \vec{k} \rangle^{\text{eq}} = 0$, thus preventing a current from flowing. Outside of equilibrium, the net current is caused by a different distribution of k -vectors which stems from a shift of the Fermi sphere. We can write the out-of-equilibrium current density as

$$\vec{j} = -en\frac{\hbar}{m}\left(\langle \vec{k} \rangle - \langle \vec{k} \rangle^{\text{eq}}\right) = -en\frac{\hbar\delta\vec{k}}{m}, \quad (2.19)$$

which can be interpreted as if every electron had the momentum $\delta\vec{k}$, thus recovering the ingredients of the Drude model and showing already here why the two result in the same conductivity. The momentum can change according to

$$\frac{d\langle \vec{k} \rangle}{dt} = \left. \frac{\partial \langle \vec{k} \rangle}{\partial t} \right|_{\text{force}} + \left. \frac{\partial \langle \vec{k} \rangle}{\partial t} \right|_{\text{scattering}}, \quad (2.20)$$

which vanishes in the stationary case. Similarly to the Drude model we can make a relaxation ansatz

$$\left. \frac{\partial \langle \vec{k} \rangle}{\partial t} \right|_{\text{scattering}} = -\frac{\langle \vec{k} \rangle - \langle \vec{k} \rangle^{\text{eq}}}{\tau} = -\frac{\delta \vec{k}}{\tau}. \quad (2.21)$$

The force term can be evaluated as

$$\vec{F} = -e\vec{E} = \frac{d\vec{p}}{dt} = \hbar \frac{\partial \langle \vec{k} \rangle}{\partial t}, \quad (2.22)$$

from which

$$\left. \frac{\partial \langle \vec{k} \rangle}{\partial t} \right|_{\text{force}} = -\frac{e\vec{E}}{\hbar} \quad (2.23)$$

can be obtained. From equation 2.20 we thus reach the result stating

$$\delta \vec{k} = -\frac{e\vec{E}}{\hbar} \tau, \quad (2.24)$$

which together with equation 2.19 results again in the Drude conductivity

$$\sigma = \frac{ne^2\tau}{m}. \quad (2.25)$$

In the Sommerfeld model the electrons undergoing the collisions that lead to the electrical resistivity propagate at the Fermi velocity. The mean free time between collisions, τ is related to the the Fermi velocity v_F via the mean free path ℓ according to

$$v_F = \frac{\ell}{\tau}. \quad (2.26)$$

The conductivities in the Drude and Sommerfeld model are the same despite the differences in the two theories. The origin of this is that in the Drude model a lot of electrons contribute with a small velocity to the conductivity, whereas in the Sommerfeld model, a small number of electrons contributes with a large velocity to the conductivity. In the case of more complicated Fermi surfaces, the picture changes and only the Sommerfeld model can still explain the properties. Further refinement of the model is obtained in terms of the Boltzmann transport equation and Fermi liquid theory.

2.1.5 Ordinary Hall Effect

The Hall effect was first discovered by Edwin Hall in 1879 [78]. It is also referred to as the ordinary Hall effect to distinguish it from other types of effects combined into the term Hall effect. The model to explain it is very simple and is based on classical physics. It states that when a current is applied to a material in a magnetic field and the magnetic field is not collinear to the current, then the current is deflected according to the Lorentz force given by

$$\vec{F} = q\vec{v} \times \vec{B}. \quad (2.27)$$

This leads to a charge build-up on one side of the material, which leads to an electric field across the sample. Once the force exerted on the charge carriers by this electric field cancels the Lorentz force, the equilibrium is reached. Assuming magnetic field, current and Hall voltage are perpendicular to each other, this happens at

$$qv_x B_z = qE_y, \quad (2.28)$$

which together with $E = -V/w$ and $j = nqv_D$ results in the Hall voltage

$$V_y = -\frac{j_x B_z w}{nq}. \quad (2.29)$$

The Hall coefficient R_H is calculated as

$$R_H = \frac{E_y}{j_x B_z} = \begin{cases} \frac{1}{nq} & \text{holes} \\ -\frac{1}{ne} & \text{electrons} \end{cases} \quad (2.30)$$

The sign of the Hall coefficient reflects the sign of the charge carriers. One remarkable result of this model is that, given a current in a specified direction, both types of charge carriers, i.e. electrons and holes, are deflected to the same side of the sample, as a reversal of the velocity and the charge lead to a force in the same direction. This is the reason for the sensitivity of the Hall effect to the sign of the charge carriers. The fact that the Hall effect in the single band picture essentially depends only on the charge carrier density, makes it an ideal type of measurement for investigating only a single variable.

The relation to the Hall resistivity can be obtained by combining equations 2.2 and 2.30, from which we see that

$$\rho_{xy} = R_H B, \quad (2.31)$$

which show us that the Hall resistivity increases linearly in field and is independent of temperature, at least not explicitly.

The Hall coefficient is related to the conductivity by the mobility, since, with $q = \pm e$,

$$|R_H \sigma_{xx}| = \left| \frac{1}{nq} \frac{ne^2 \tau}{m} \right| = \frac{e\tau}{m} = \mu, \quad (2.32)$$

or equivalently

$$\sigma_{xy} = \pm \mu B \sigma_{xx} = \pm \omega_c \tau \sigma_{xx}, \quad (2.33)$$

where $\omega_c = eB/m$ is the cyclotron frequency and $+$ is for holes and $-$ is for electrons.

The Hall effect is a useful physical phenomenon for applications. It is for example used in Hall effect sensors, where the magnetic field strength can be measured from a sensor with a known Hall coefficient. This is used as the compass in mobile phones. Another example are Hall effect thrusters used in space flight.

2.1.6 Anomalous Hall Effect

A special variant of the Hall effect, called the anomalous Hall effect, can be observed in certain materials with broken time-reversal symmetry, such as ferromagnets, where it arises from spin orbit coupling [79]. It was first discovered in 1881, again by Edwin Hall [80]. The anomalous Hall effect is related to the magnetization M in the sample but it is not merely a contribution of M to the overall magnetic field inside the sample. This variant of the Hall effect is independent of an external magnetic field. As long as the sample is magnetized, such as a ferromagnet, the effect appears. In contrast to the relatively easy explanation of the ordinary Hall effect, the explanation for the anomalous Hall effect took almost a century to be obtained. The reason for this is that the necessary concepts, such as topology and the Berry phase [81], have only been formulated in more recent times. An important step forward on the way came from the concept of the anomalous velocity, which is only related to the band structure and does not incorporate any scattering [82].

The combined effects of the ordinary and the anomalous Hall effects can for many ferromagnetic materials be written as

$$\rho_{xy} = R_H B_z + R_s \mu_0 M_z, \quad (2.34)$$

where R_s is the anomalous Hall coefficient, i.e. the parameter describing the effects due to spontaneous magnetization. It is more complicated to understand than R_H

and depends on many material specific parameters. Most importantly it depends on ρ_{xx} in form of a power law as $\rho_{xy}^A \propto \rho_{xx}^\beta$ [79].

The anomalous Hall effect is usually subdivided into several types, depending on its origin. These categories are typically the intrinsic contribution, side jump, and skew scattering. The intrinsic contribution stems from the band structure alone and is independent of any scattering processes. The anomalous Hall resistivity from this process is usually $\rho_{xy}^A \propto \rho_{xx}^2$ and σ_{xy}^A is independent of σ_{xx} . It is usually described in terms of the Berry curvature. The anomalous Hall effect in this picture is similar to an unquantized version of the quantum Hall effect. In the skew scattering process the anomalous Hall resistivity is caused by asymmetric scattering based on the spin orbit interaction of the electrons or the impurities. This leads to $\rho_{xy}^A \propto \rho_{xx}$. The third type is the side jump process, originating again from spin orbit coupling when electrons interact with the electric fields of the impurities upon approaching or leaving an impurity. It leads again to $\rho_{xy}^A \propto \rho_{xx}^2$. The skew scattering and side jump scenarios can also be grouped together as the extrinsic processes.

2.2 Nernst and Seebeck Effect

The two components of the thermoelectric effect, the Nernst [83] and Seebeck [84] effects, are closely related to the Hall resistivity and the longitudinal resistivity, but are based on a thermal gradient in the sample opposed to an electrical current. Both effects are based on a transport of entropy. Today these two effects are still of great value and offer much insight into important material properties [85, 86].

The Seebeck effect is the longitudinal version of the effect, while the Nernst is the transverse version. The Seebeck and Nernst signals are defined as

$$S = \frac{E_x}{\nabla_x T} \quad (2.35a)$$

$$N = \frac{-E_y}{\nabla_x T}, \quad (2.35b)$$

where S and N could also be written as S_{xx} and S_{xy} respectively. In a macroscopic setting the equations turn into

$$S = \frac{-\Delta V_x}{\Delta T_x} \quad (2.36a)$$

$$N = \frac{\Delta V_y/w}{\Delta T_x/l}, \quad (2.36b)$$

where w and l are the width and length of the sample. For the longitudinal case the geometry factors are l both above and below the fraction and thus cancel. The Seebeck signal is thus independent of the sample geometry. The sign convention is such that S reflects the sign of the charge carriers. In the case of the Nernst effect, the sign of N is more complicated to understand. The Nernst coefficient ν is simply the Nernst signal divided by the magnetic field:

$$\nu = \frac{N}{B}. \quad (2.37)$$

In order to get from the Hall effect to the Nernst effect, the electrical current is replaced by a temperature gradient. If in a further step the measurement of a transversal voltage difference is replaced with the measurement of a temperature difference this results in the thermal Hall effect, the transverse component of the heat conduction.

In more general terms the connection between the charge current j , the heat current j_Q , the electric field E , and the temperature gradient $\vec{\nabla}T$ is given by the two equations

$$\vec{j} = \sigma \vec{E} - \alpha \vec{\nabla}T \quad (2.38a)$$

$$\vec{j}_Q = T\alpha \vec{E} - \kappa \vec{\nabla}T \quad (2.38b)$$

and depends on the conductivity tensors σ (charge), κ (heat), and α (thermoelectricity). In the case of absence of a charge current ($\vec{j} = 0$) the first equation simplifies to

$$\vec{E} = \sigma^{-1} \alpha \vec{\nabla}T \quad (2.39)$$

which gives us the Nernst signal's dependence on σ and α :

$$N = \frac{\alpha_{xy}\sigma_{xx} - \alpha_{xx}\sigma_{xy}}{\sigma_{xx}^2 + \sigma_{xy}^2}. \quad (2.40)$$

The thermoelectric tensor is linked in turn to the conductivity tensor by the Mott relation

$$\alpha = \frac{\pi^2 k_B^2 T}{3 e} \left. \frac{\partial \sigma}{\partial \mu} \right|_{E_F}. \quad (2.41)$$

It quantifies the change in conductivity due to a changing chemical potential. In combining the equations 2.40 and 2.41 for the case where $\sigma_{xy} \ll \sigma_{xx}$ the Nernst effect can be linked to the Hall angle Θ_H (equation 2.11):

$$N = \frac{\pi^2 k_B^2 T}{3 e} \left. \frac{\partial \tan \Theta_H}{\partial \mu} \right|_{E_F}. \quad (2.42)$$

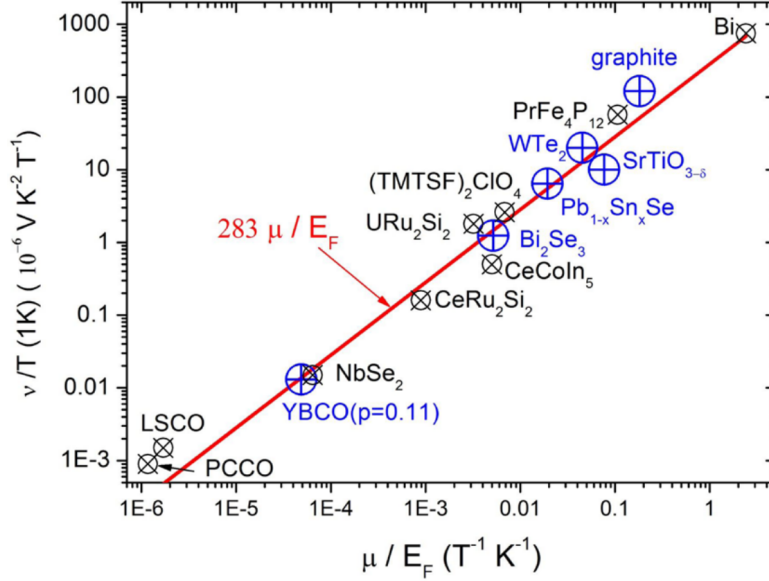


Fig. 2.2 The universality curve of the quasiparticle Nernst effect with a comparison to different materials. Taken from Ref. [86].

In the case of the Nernst coefficient this can further be simplified using equation 2.33 as

$$\nu = \frac{\pi^2 k_B^2 T}{3 m} \left. \frac{\partial \tau}{\partial \mu} \right|_{E_F} \quad (2.43)$$

or as

$$\nu = \frac{\pi^2 k_B^2 T}{3 e} \frac{\mu_H}{E_F} \quad (2.44)$$

under the assumption that $\partial \tan \Theta_H / \partial \mu$ at E_F can be linearized to $B\mu_H/E_F$. The Nernst coefficient thus depends on the mobility. A large mobility and a small Fermi energy are the ingredients for a large Nernst effect. Furthermore this equation defines a universality curve for the quasiparticle Nernst effect which can be expressed numerically as [85, 86]

$$\nu/T = (2.83 \times 10^{-4} \text{ V/K}) \mu_H/T_F. \quad (2.45)$$

This relation works very well for a wide range of materials, as shown in figure 2.2. This good agreement shows that the simplifications necessary to obtain the equation are justified and actually relevant in nature.

The Seebeck effect, on the other hand, can be quantified as

$$S = \frac{\pi^2 k_B}{2 e} \frac{T}{T_F} \quad (2.46)$$

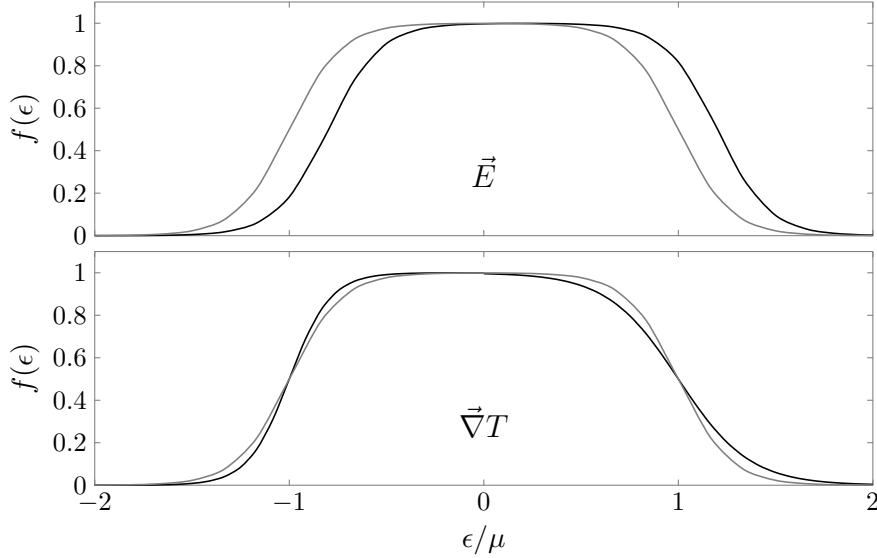


Fig. 2.3 The influence of an electric field (top) and a thermal gradient (bottom) onto the Fermi-Dirac distribution f (black lines). The unperturbed distribution is shown for comparison (grey lines). Negative energies correspond to opposite propagation directions. While the electric field moves the Fermi sphere, a thermal gradient distorts the distribution asymmetrically. Adapted from Ref. [87].

for a free electron gas for $T \ll T_F$. Using this equation to replace T_F in equation 2.44 and replacing the mobility with the Hall angle results in

$$N = \frac{2}{3} S \tan \Theta_H, \quad (2.47)$$

an equation valid for one band systems.

Figure 2.3 shows how a thermal gradient influences the Fermi-Dirac distribution throughout the sample compared to an electric field. While the electric field leads to a shift of the distribution, in the case of the thermal gradient the shape changes.

2.3 Magnetometry

2.3.1 Overview

Magnetometry is the measurement of magnetism and its effects. The quantity being measured is usually the magnetic moment m . Its SI unit is A m^2 or equivalently J T^{-1} . When talking about single atoms, the natural way of expressing it is in units of Bohr magnetons $\mu_B = 9.274 \times 10^{-24} \text{ J T}^{-1}$. The magnetic moment is

often defined through the torque a magnetic field exerts on it:

$$\vec{\tau} = \vec{m} \times \vec{B}. \quad (2.48)$$

Connected to the magnetic moment is the magnetization M , as the magnetic moment per volume

$$\vec{M} = \frac{d\vec{m}}{dV} \quad (2.49)$$

or, for a homogeneous sample, simply

$$\vec{M} = \frac{\vec{m}}{V}. \quad (2.50)$$

For most materials the magnetization is induced by an external magnetic field. The exceptions are ferromagnetic materials. Microscopically the magnetic moment of a sample originates from its electrons. It is a purely quantum mechanical result and stems from the spin and the orbital angular momentum of the electrons. The total magnetic moment of an atom is given by

$$m = g\mu_B \sqrt{j(j+1)} \quad (2.51)$$

with the Landé g -factor and the total angular momentum j .

2.3.2 SQUIDS

SQUIDS (superconducting quantum interference devices) [88] are one of the most precise method of measuring magnetic moments [89]. These devices make use of the Josephson effect [90, 91] in superconducting rings interrupted by two weak links. The magnetic flux through the ring has to be quantized. In order to comply with this quantum mechanical requirement, a current flows through the ring to adjust the flux to an allowed value. A change in flux from the external source is thus always reflected by a change in the voltage that is measured at the SQUID. This is the principle by which a SQUID translates a flux into a voltage.

The machine present in our laboratory making use of a SQUID is the Magnetic Property Measurement System (MPMS), manufactured by the company Quantum Design and able to reach 7 T. The measurement procedure is to move the sample vertically through a set of four pickup coils. Their assembly is shown in figure 2.4. The coils are arranged such that the two inner coils are close together and have the same winding direction. The two outer coils are spaced further apart and have an opposite winding direction. The total signal the four pickup coils collect is then

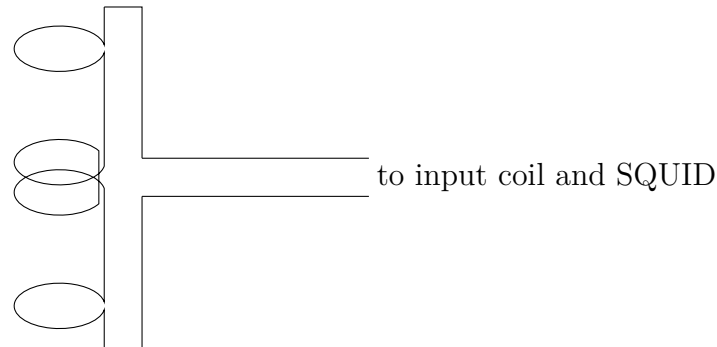


Fig. 2.4 A sketch of the second derivative gradiometer arrangement of the four pickup coils in the MPMS. The winding direction of the two middle coils is opposite to the winding direction of the two outer coils.

proportional to the second derivative in numerical calculations

$$f''(x) = \frac{f(x+h) - 2f(x) + f(x-h)}{h^2}. \quad (2.52)$$

For this reason this coil setup is referred to as a second derivative gradiometer. After the pickup-coils detect the signal it is then transported to an input coil where the SQUID sensor is located. This input coil then creates the magnetic field that is seen by the SQUID. This way, the actual SQUID sensor can be located in a better position than the sample space, with a constant low temperature.

2.3.3 AC Magnetization

In AC magnetometry the magnetic moment or magnetic susceptibility of a sample is measured upon application of a small AC magnetic field. This small AC field, usually with $B_{AC} \leq 10$ Oe, can be applied on top of a background DC field, which is often much larger than the AC field. In our laboratory such measurements can be performed with the AC Measurement System (ACMS) option of the PPMS. This measurement option is not based on a SQUID sensor and is expected to be less accurate, but this can be countered by longer measurement times.

The AC magnetic moment is usually defined as a complex quantity:

$$m = m' + im''. \quad (2.53)$$

The real part m' is the in-phase component of the AC magnetic moment and the imaginary part m'' is its out-of-phase component with respect to the external AC magnetic field. The same concept is also used for the related quantities of susceptibility and magnetization. Conducting AC magnetization measurements

has many advantages compared to the more common DC measurements [92]. The most important is that they can access the dynamic magnetic properties of a sample, i.e. the change of magnetism over time. The accessible time scales can be set by the AC frequency. Such measurements are of great importance for the investigations of spin glasses, phase transitions, and superparamagnetism. Since the AC susceptibility is a response function to the driving field, its real and imaginary component are linked through the Kramers-Kronig relations.

2.4 Cryostats

In order to reach low temperatures, cryostats are needed. Different methods are capable of reaching different temperatures. The cost and the limit of the sample size need to be taken into consideration when deciding for a method. Often cryostats use multiple layers, similar to an onion, where different methods are used for each layer. Typically, liquid nitrogen is used in the outermost layer, as it is cheap, readily available, and relatively easy to handle. In its liquid form it has a temperature of 77 K. The next layer is typically liquid helium, which is more expensive, but has a temperature of 4.2 K. Upon pumping on a helium reservoir temperatures of 1.8 K can be reached by reducing the vapour pressure, creating the next layer of the cryostat. This He reservoir is replenished by a constant inflow of He from the dewar one layer further out. Even lower temperatures can be reached by means of the isotope ^3He , being capable of cooling down to around 300 mK when pumping on the reservoir.

In the case of our laboratory, two PPMSs are available, which are cooled by liquid nitrogen and helium. An external inset based on ^3He is available. It is a closed cycle system in order to avoid loss of the very expensive ^3He .

Dilution refrigerators are among the cryostats able to reach the lowest temperatures for macroscopic samples. Temperatures well below 100 mK can be reached this way. A great advantage of this type of cryostat is that it can still cool continuously. Their working principle is based on a mixture of the two He isotopes ^4He and ^3He . When temperatures below 860 mK are reached a phase separation between the isotopes occurs. Inside the mixing chamber the ^3He flows from the concentrated ^3He rich phase into the diluted phase. The heat necessary for this dilution process to occur is what cools down the mixing chamber.

To reach even lower temperature, adiabatic demagnetization refrigerators can be used, which are able to achieve temperatures on the order of 1 mK. Usually, these refrigerators can not be used in a continuous manner, as the magnet needs to be remagnetized from time to time. For bulk samples the cooling becomes very

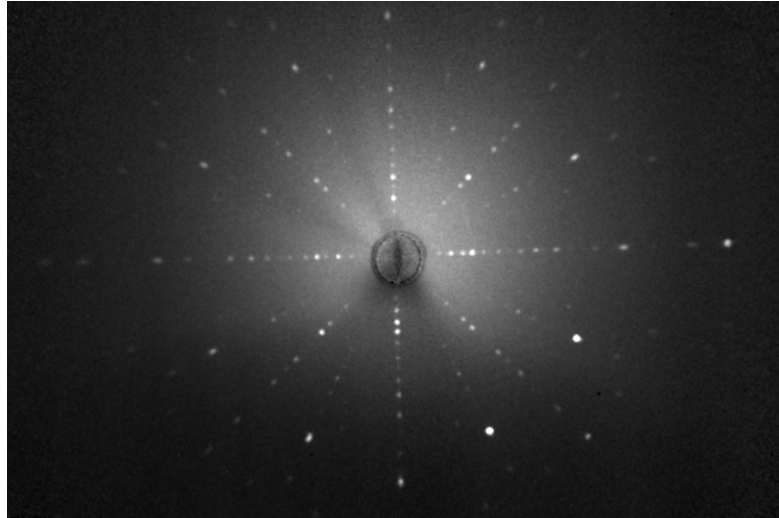


Fig. 2.5 Laue recording of $\text{Ca}_{1.8}\text{Sr}_{0.2}\text{RuO}_4$. The star shape indicates that the c -axis is parallel to the beam. Based on the angles between lines, the Ru-O direction can be distinguished from the Ru-Ru direction.

hard at this stage but for atomic gasses, temperatures in the pico kelvin range can be reached by laser cooling and forced evaporation cooling.

2.5 X-Ray Diffraction: Laue Method

The Laue method is an x-ray scattering technique to resolve the structure of crystals. It was described in 1912 by Max von Laue [93]. It explains how in certain points x-rays are scattered while in others they are not. In terms of equations the scattering occurs when conditions are met by the scalar product of the crystal vectors and the change in \vec{k} given by

$$\vec{a} \cdot \Delta\vec{k} = 2\pi h \quad (2.54a)$$

$$\vec{b} \cdot \Delta\vec{k} = 2\pi k \quad (2.54b)$$

$$\vec{c} \cdot \Delta\vec{k} = 2\pi l \quad (2.54c)$$

for integer numbers h , k , and l . Equivalently the scattering can also be described by Bragg's law

$$2d_{hkl} \sin \theta = n\lambda. \quad (2.55)$$

In this formula d_{hkl} describes the lattice plane separation in (hkl) direction, θ is the scattering angle, n is an integer, and λ is the wavelength.

Most of the time Laue scattering is used to orient crystals along desired crystal axes. A typical Laue image is shown in figure 2.5 for the material $\text{Ca}_{1.8}\text{Sr}_{0.2}\text{RuO}_4$. In order to identify the c -axis, the sample is rotated in all directions, until a star-shaped pattern emerges, which reflects the symmetry when looking along the c axis. This means that the plane perpendicular to the beam is the ab -plane. By cutting the sample or by grinding the sample with sandpaper, an oriented sample with surfaces parallel to the crystal planes is obtained. If other directions than the c -axis are desired, a computer program can be used to simulate the expected patterns for a given space group. The sample is then rotated until agreement between the calculated and observed patterns is obtained. The Laue diffraction pattern shown in the figure can also be used to distinguish the Ru-O direction and the Ru-Ru directions by comparing the angles between lines. The horizontal and vertical directions correspond to the Ru-O directions, while the diagonals correspond to the Ru-Ru directions.

2.6 Models for Superconducting Fluctuations

Superconducting fluctuations can be described in different theories. The main choice is whether the fluctuations are of the phase fluctuating or amplitude fluctuating kind. Amplitude fluctuations are the more prevalent type and usually present even in the case of phase fluctuations as an additional contribution. Different processes can contribute to the amplitude fluctuating scenario, also termed the Gaussian scenario [28, 94].

In the Aslamazov-Larkin model [34] Cooper pairs exist for a short time before decaying again. This Cooper pair life time is given by [28]

$$\tau = \frac{\pi\hbar}{8k_{\text{B}}T_c}\epsilon^{-1}, \quad (2.56)$$

with the definition

$$\epsilon = \ln\left(\frac{T}{T_c}\right) \quad (2.57)$$

for the measure of the distance of the temperature to the critical temperature.

The paraconductivity in this model can be expressed for different dimensions in the following way:

$$\Delta\sigma_{xy}^{3\text{D}} = \frac{e^2}{32\hbar\xi}\frac{1}{\sqrt{\epsilon}}, \quad (2.58)$$

$$\Delta\sigma_{xy}^{2\text{D}} = \frac{e^2}{16\hbar d}\frac{1}{\epsilon}, \quad (2.59)$$

$$\Delta\sigma_{xy}^{1D} = \frac{\pi e^2 \xi}{16\hbar A} \frac{1}{\epsilon^{3/2}}. \quad (2.60)$$

Upon increase in dimension the paraconductivity depends more weakly on ϵ . The general dependence is $\Delta\sigma_{xy}^{nD} \propto 1/\epsilon^{(4-n)/2}$. The dimensionality of the system thus plays a big role and lower dimensions usually display a stronger temperature dependence. In one and three dimensions, the coherence length ξ enters the equations, while for two dimensions it does not. Counterintuitively, in the one- and two-dimensional cases the paraconductivity depends on the geometry of the object under investigation by containing the wire cross-section A and the film thickness d .

In stacked materials such as the cuprates the layers can act as individual two-dimensional superconductors. The crossover between two and three dimensions based on interacting planes is described by the Lawrence-Doniach model. In it the paraconductivity is given by

$$\Delta\sigma_{xx} = \frac{e^2}{16\hbar d} \frac{1}{\sqrt{\epsilon(\epsilon+r)}}. \quad (2.61)$$

Depending on the size of the anisotropy parameter r in relation to ϵ the two- or three-dimensional AL contributions are recovered.

The AL fluctuations are accompanied by indirect contributions, i.e. contributions that do not originate from the fluctuating Cooper pairs directly, mainly the Maki-Thomson and the density-of-states corrections [28]. Depending on the material, these contributions have varying impact on the observed paraconductivity.

The Maki-Thomson fluctuations are a purely quantum mechanical correction term to the AL paraconductivity based on interactions of normal state quasiparticles with fluctuating Cooper pairs [95,96]. The MT contribution only influences transport coefficients due to its influences on the mean free path. The amplitude of this interaction is given by $g_{\text{eff}} = 1/\epsilon$. This leads to a fluctuation contribution which in two dimensions has the general form

$$\Delta\sigma_{xx}^{\text{MT}} \approx \frac{e^2}{8\hbar\epsilon} \ln \left(\frac{D\tau_\phi}{\xi^2(T)} \right) \quad (2.62)$$

with the dephasing time τ_ϕ and the diffusion constant D .

For layered superconductors it follows the form [94,97,98]

$$\Delta\sigma_{xx}^{\text{MT}} = \Delta\sigma_{xx}^{\text{AL}} \frac{2\epsilon}{\epsilon - \delta} \ln \left(\frac{\epsilon}{\delta} \frac{1 + \alpha + \sqrt{1 + 2\alpha}}{1 + \frac{\alpha\epsilon}{\delta} + \sqrt{1 + 2\frac{\alpha\epsilon}{\delta}}} \right), \quad (2.63)$$

with the pair-breaking parameter

$$\delta = \frac{\pi \hbar}{8k_B T \tau_\phi} \quad (2.64)$$

and the coupling parameter

$$\alpha = \frac{2\xi^2(0)}{d^2\epsilon}. \quad (2.65)$$

In the 2D limit this reduces to

$$\Delta\sigma_{xx}^{\text{MT}} = \Delta\sigma_{xx}^{\text{AL}} \frac{2\epsilon}{\epsilon - \delta} \ln\left(\frac{\epsilon}{\delta}\right). \quad (2.66)$$

An additional correction based on the density-of-states can become another factor of importance. When two electrons form a Cooper pair, there are now less electrons available in the regular conduction channel, leading to an increase in the resistivity. It can be calculated directly from the Drude formula (equation 2.17) as

$$\Delta\sigma_{xx}^{\text{DOS}} = -\frac{2n_s e^2 \tau}{m_e} \quad (2.67)$$

since the fluctuating Cooper pair density n_s above the transition is exactly half the number of missing electrons. The negative sign determines a decrease in conductivity. Without detailed microscopic considerations the behaviour as a function of ϵ can already be obtained and gives

$$\Delta\sigma_{xx}^{\text{DOS}} \propto -\ln \frac{2}{\sqrt{\epsilon} + \sqrt{\epsilon + r}}. \quad (2.68)$$

In the two-dimensional case the anisotropy parameter $r = 0$.

In the case of phase fluctuations an exponential resistivity behaviour is expected. In order to combine amplitude and phase fluctuations the dependence of $\Delta\sigma_{xx}$ on temperature can be expressed in an intermediate step by its dependence on the superconducting coherence length, the size of the fluctuating Cooper pair, which is $\Delta\sigma_{xx} \propto \xi^2(T)$ [99, 100]. The superconducting fluctuations are expected to diverge at T_c , which in the case of Gaussian fluctuations happens in form of a simple power law $\xi \propto \epsilon^{-1/2}$. Phase fluctuations, on the other hand, are expected to diverge exponentially. To fill in the gap between the two fluctuation regimes, a phenomenological interpolation model was suggested by Halperin and Nelson [99]. Their results states that

$$\Delta\sigma_{xx} = \frac{0.37}{b} \sigma_{xx}^n \sinh^2 \left(\sqrt{\frac{b\tau_c}{\tau}} \right), \quad (2.69)$$

where σ_{xx}^n is the normal state conductivity, b is a dimensionless constant of order unity,

$$\tau = (T - T_{\text{BKT}})/T_{\text{BKT}}, \quad (2.70)$$

and the measure of the distance of T_c to T_{BKT}

$$\tau_c = (T_c - T_{\text{BKT}})/T_{\text{BKT}}, \quad (2.71)$$

with T_c the standard BCS critical temperature and T_{BKT} the Berezinskii-Kosterlitz-Thouless temperature. In this scenario the film is only fully superconducting with $R = 0$ below T_{BKT} . In between T_{BKT} and T_c the system would be dominated by phase fluctuations. The limits of equation 2.69 are exponential for $b\tau_c/\tau \gg 1$ and the Aslamazov-Larkin behaviour ($1/\tau \approx 1/\epsilon$) is recovered for $b\tau_c/\tau \ll 1$ upon linearization of the sinh.

Chapter 3

Hall Effect Study of the Superconducting Fluctuations in a Thin Film of NbN

3.1 Introduction

Among all the different superconductors it is especially of interest to investigate materials which exhibit a crossover between a Bose-Einstein condensate (BEC) and the Bardeen-Cooper-Schrieffer (BCS) regime [101–104], as different fluctuations are expected for the two cases. In the BCS regime the expected fluctuations are amplitude fluctuations, whereas in the BEC regime one expects phase fluctuations.

In the cuprates the overdoped side is usually considered to be ruled by BCS theory and the accompanying amplitude fluctuations [30], whereas on the underdoped side, or more precisely in the pseudogap phase, the case is less clear. There is evidence of phase fluctuations [27, 105–107], but at the same time amplitude fluctuations have been observed [33, 86, 108–111]. The same data set has even been taken as evidence for phase fluctuations by one group [112, 113] and for amplitude fluctuations by another [114]. Further support for phase fluctuations in the underdoped regime of high temperature superconductors comes from the low superconducting carrier density leading to a small phase stiffness [37, 115, 116].

A stronger response, i.e. faster growth upon approaching T_c , is usually expected for lower dimensions. This makes thin films ideal candidates for the study of superconducting fluctuations. The same behaviour is also expected for layered compounds, with corrections for interacting layers, which makes it easier to investigate cuprates compared to other bulk superconductors.

One way to get an improved understanding of the superconducting fluctuations in cuprates is to investigate systems that show a similar crossover between

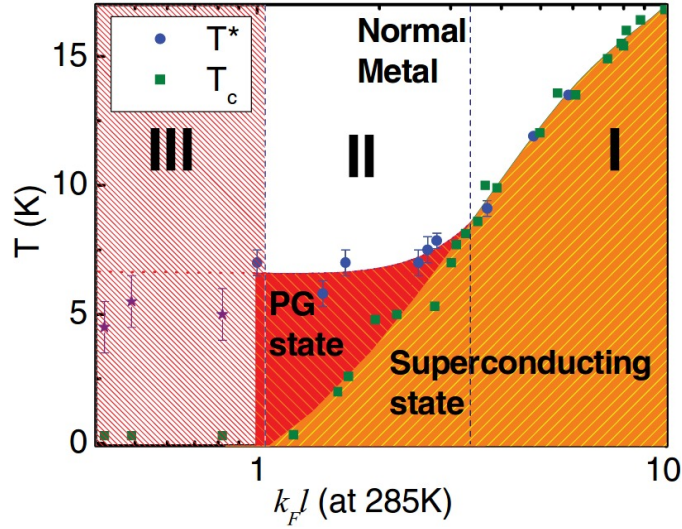


Fig. 3.1 The phase-diagram of NbN thin films as functions of T and $k_F l$. The pseudogap (PG) phase appears for high disorder at low temperatures between the superconducting and normal metallic phases. The sample of this chapter lies at $k_F l = 4.6$ and has a T_c of 15 K. Taken from Ref. [117].

BEC and BCS. One such system is NbN, where phase fluctuations and a connected pseudogap state for high disorder have recently been discovered [117, 118]. A phase diagram showing the location of the pseudogap is shown in figure 3.1. Another, very similar system, is TiN, for which a pseudogap has been identified as well [119, 120]. It is thus of great interest to carefully investigate such thin films in both the BCS and BEC region in order to obtain a better understanding of the fluctuation mechanism and the causes of superconductivity. Other nitrogen compounds that have recently been investigated by means of fluctuations are TaN [121, 122], and MoN [123], both showing behaviour consistent with Gaussian fluctuation theory [124].

NbN is a well characterized material, both in its superconducting and metallic state, which is in parts due to and in parts the reason for there being a wide array of applications, for example hot-electron bolometers [125, 126] and superconducting single photon detectors [127, 128]. Their high operating speed and low dark count rate make them ideal for applications in quantum optics. One important advantage of NbN over other superconducting films is the high T_c and the large superconducting gap. The fact that it is a type II superconductor furthermore makes it suitable for use in high magnetic fields. Different growth methods have been used to grow NbN films, such as reactive magnetron sputtering [129], high-temperature chemical vapor deposition [130], ion beam assisted sputtering [131],

or pulsed laser deposition [132]. It can even be grown as free standing films [133]. Many of its properties have been widely studied, including different transport properties [134–136]. On the other hand it has served as a model system to investigate the dynamics of superconductivity out of equilibrium [137–140].

For the purpose of this study we use a NbN film outside of the pseudogap phase. It is our goal to study the superconducting fluctuations in the region where they are predicted to be governed by Gaussian fluctuations [124]. We do this by investigating the paraconductivity and the contribution of the fluctuations to the Hall effect.

The sign of the superconducting fluctuations is determined by the derivative of the logarithm of the critical temperature with respect to the chemical potential $d \ln(T_c)/d\mu$ [124, 141]. For NbN, as for most other conventional superconductors, this derivative is positive [134] and thus the Hall coefficient of the superconducting (SC) fluctuations is expected to be positive, $R_{H,SC} > 0$. This is in contrast to the Hall coefficient expected for the electron quasiparticles (QP), which are the charge carriers in this material [134], where $R_{H,QP} < 0$ is thus expected. This opposite contribution to the Hall effect makes it easier to disentangle the two contributions.

A number of different films of varying thickness was initially characterized by resistivity measurements and later expanded to Hall measurements. For the detailed measurements we chose a film at the upper end of the thickness scale. This has multiple reasons. One important is the decay of the films over time, which is more pronounced the thinner the films get. Another is that the thicker films have a higher T_c , which is favourable in the context of fluctuations as they are dependent on $\epsilon = \ln(T/T_c)$, thus expanding the fluctuation region over a larger temperature range.

3.2 Methods

The NbN films were grown by Konstantin Ilin from the Karlsruhe Institute of Technology. The growth procedure was performed on sapphire substrate by using DC reactive magnetron sputtering of a target of pure Nb in an atmosphere composed of a mixture of Ar and N₂ gases. The dimensions of the film plane are 1 cm × 1 cm. The thickness of the sample was measured with a stylus profiler, and resulted in $d = 11.9(2)$ nm. The necessary contacts on the sample were made from gold and arranged in a Hall bar geometry, as shown in figure 3.2. Silver wires were then glued to the gold contacts with silver paint, which resulted in a good contact resistance after drying in air for ≈ 30 min. The measurements were carried out in a PPMS capable of reaching magnetic fields up to 9 T. For all measurements the magnetic field has been applied perpendicular to the film plane. Great care was

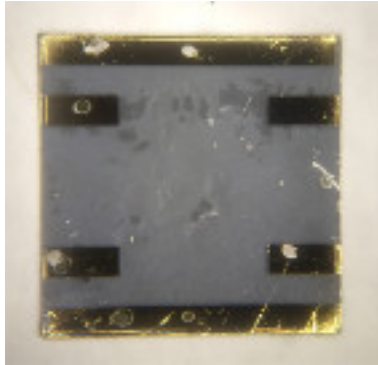


Fig. 3.2 A photo of a NbN film with the Hall bar geometry of gold contacts.

taken to minimize any offsets or backgrounds. For this purpose both temperature and field were stabilized at each measurement point. This was done for positive and negative magnetic fields (negative meaning pointing in the opposite direction) in order to obtain the antisymmetric part of the signal, which is the true Hall signal. Contributions originating from misaligned contacts, i.e. a background of ρ_{xx} , can be removed this way.

3.3 Experimental Results

The experiment consisted of resistivity measurements, combined of longitudinal and Hall resistivity. The longitudinal resistivity ρ_{xx} is shown in figure 3.3. It has been measured between 0 T and 9 T in steps of 1 T. We define the critical temperature as the temperature at which ρ_{xx} is steepest, i.e. $d\rho_{xx}/dT$ is at its maximum. This criterion is useful as the Aslamazov-Larkin theory predicts a diverging slope at T_c . In our film, for zero magnetic field, T_c is found to be 14.96(2) K. We can determine the transition so precisely thanks to the extremely sharp downturn of ρ_{xx} . Upon application of a magnetic field perpendicular to the film the transition shifts linearly towards lower temperatures.

The inset of figure 3.3 shows the critical magnetic field B_{c2} as function of temperature. The red line is a fit to a linear function. Its slope can be used to obtain the zero temperature critical field $B_{c2}(0)$, using the Werthamer-Helfand-Hohenberg (WHH) relation [142],

$$B_{c2}(0) = -0.69T_c \frac{dB_{c2}}{dT}, \quad (3.1)$$

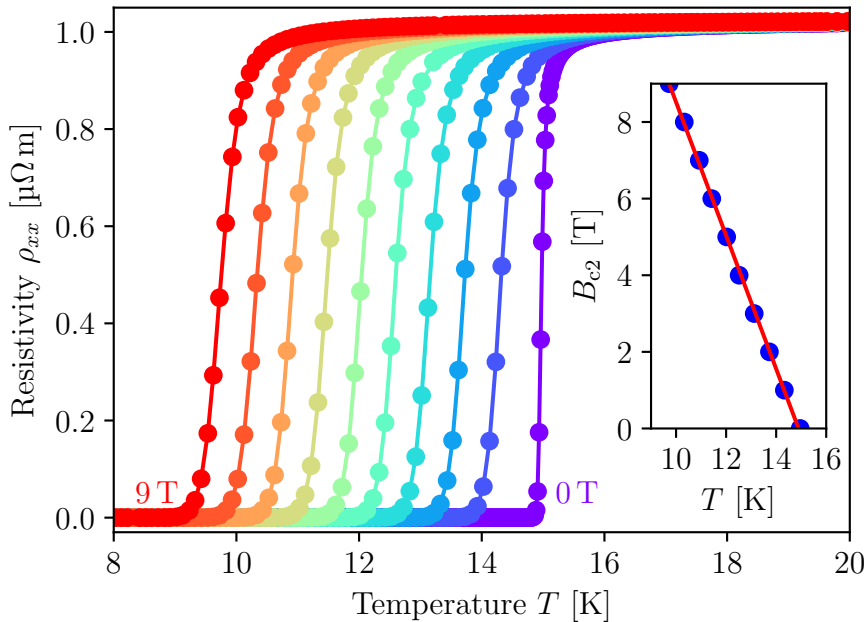


Fig. 3.3 Resistivity ρ_{xx} as function of temperature T measured for magnetic fields between 0 and 9 T in steps of 1 T. The magnetic field is perpendicular to the film plane. Solid lines are guides to the eye. The inset shows B_{c2} , defined as the steepest part of the resistivity, as function of temperature. The red line is a fit to a linear function, used to calculate $B_{c2}(0)$.

valid in the dirty regime of superconductors. We obtain $B_{c2}(0) = 18$ T, consistent with other reports [143, 144]. The WHH behaviour in NbN is valid independent of the film thickness [136].

The Hall resistivity as function of field is shown in figure 3.4. It focuses on the low-field part below 2 T, where the influence of the superconducting fluctuations can be seen. It displays three isotherms, two close to T_c and one far enough away to suppress the superconducting fluctuations completely. The inset shows one of the isotherms over the whole range of measurement, up to 9 T. It is clearly linear, as expected for the quasiparticle contribution to the Hall resistivity. The negative slope is due to electrons being the relevant charge carriers.

The slope is equal to the Hall coefficient $R_H = \rho_{xy}/B$ and can be used to calculate the carrier density $n = -1/(R_H e) = 4.2 \times 10^{23} \text{ cm}^{-3}$, a typical value for a metal [145]. This number can further be used to obtain the Fermi wavevector $k_F = (3\pi^2 n)^{1/3} = 2.3 \text{ \AA}^{-1}$. This can in turn be used to calculate the mean free path of the electrons $\ell = \hbar k_F / (n e^2 \rho_{xx}) = 2.0 \text{ \AA}$ and the Fermi energy $E_F = \hbar^2 k_F^2 / 2m = 20.5 \text{ eV}$, where $\rho_{xx} = 1 \mu\Omega \text{ m}$ is taken above the superconducting transition. This mean free path is extremely short, orders of magnitude smaller than the film

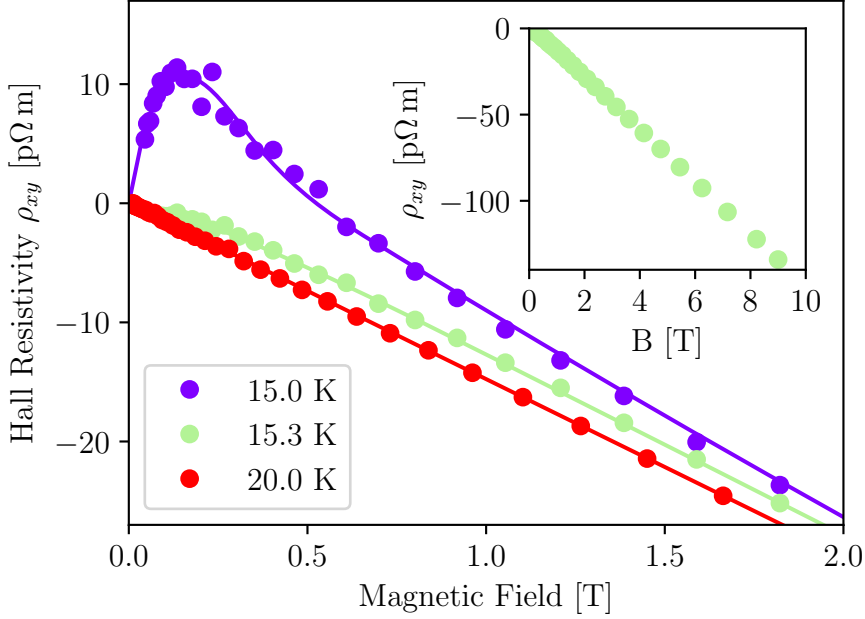


Fig. 3.4 Hall resistivity ρ_{xy} as function of magnetic field B in the low-field region for temperatures as indicated. For the $T = 15$ K ($\approx T_c$) isotherm a clear sign change can be observed. The inset shows the Hall resistivity for the whole measured range up to 9 T. The high-field behaviour is linear, as expected for the quasiparticle contribution. The negative slope indicates negative charge carriers, i.e. electrons. Solid lines are guides to the eye.

thickness $d = 11.9$ nm, and confirms that our NbN film is in the dirty limit of metals.

From the critical field B_{c2} we can calculate the zero temperature coherence length using

$$\xi_0 = \sqrt{\Phi_0 / (2\pi B_{c2}(0))}, \quad (3.2)$$

where $\Phi_0 = 2.07 \times 10^{-15}$ Wb is the flux quantum. This yields $\xi_0 = 43$ Å. This length scale is a bit below the film thickness, but since our measurements are conducted around T_c where the coherence length and the magnetic penetration depth diverge [100], we can conclude that we have two-dimensional superconductivity, while the quasiparticle electrons feel a three-dimensional environment due to the short mean free path.

For low fields and temperatures close to T_c the influence of superconducting fluctuations can be seen as a deviation from the linear background. For the isotherm of lowest temperature a sign change from negative to positive can be observed upon approaching $B = 0$ from above. This sign change can be observed

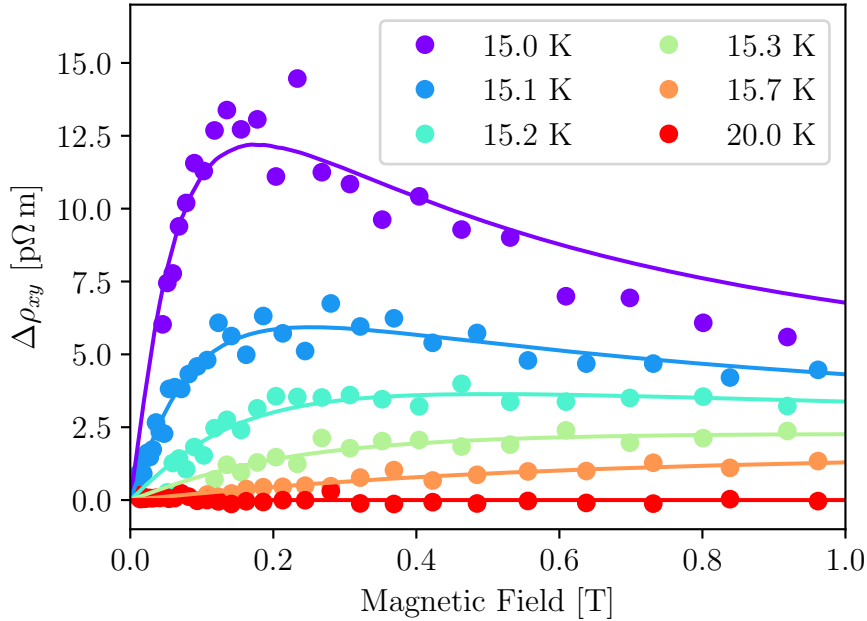


Fig. 3.5 The Hall resistivity $\Delta\rho_{xy}$ after removal of the linear quasiparticle background. The magnitude of the signal decays rapidly upon increasing the temperature. Solid lines are guides to the eye.

only in a narrow temperature window of approximately 0.3 K above T_c . For higher temperatures up to about 1 K above T_c a deviation in positive direction can be seen, but no sign change any more, as the magnitude of the effect drops below the magnitude of the quasiparticle background. The fact that there are two different signs involved makes it clear that there are two independent effects at work, as opposed to one effect getting weaker or stronger upon change of the magnetic field.

In figure 3.5 the linear quasiparticle background of the Hall signal is subtracted to obtain $\Delta\rho_{xy} = \rho_{xy} - \rho_{xy}^{\text{QP}}$. It shows the same data as figure 3.4 and includes further isotherms in between. The rapid decay of the signal is evident and within about 1 K it vanishes below the detection limit. As opposed to the quasiparticle contribution, the superconducting fluctuations cause a highly nonlinear behaviour. It is an extremely small effect with an amplitude of around 10 pΩ m, especially when compared to $\rho_{xx} = 1.0 \mu\Omega \text{ m}$. This means that the effect we are interested in is five orders of magnitude lower than the quantity causing the background in the measurement due to misaligned contacts. It needs to be noted, though, that the actual background in the voltage measurement is smaller, as the overall contact alignment is not that extreme.

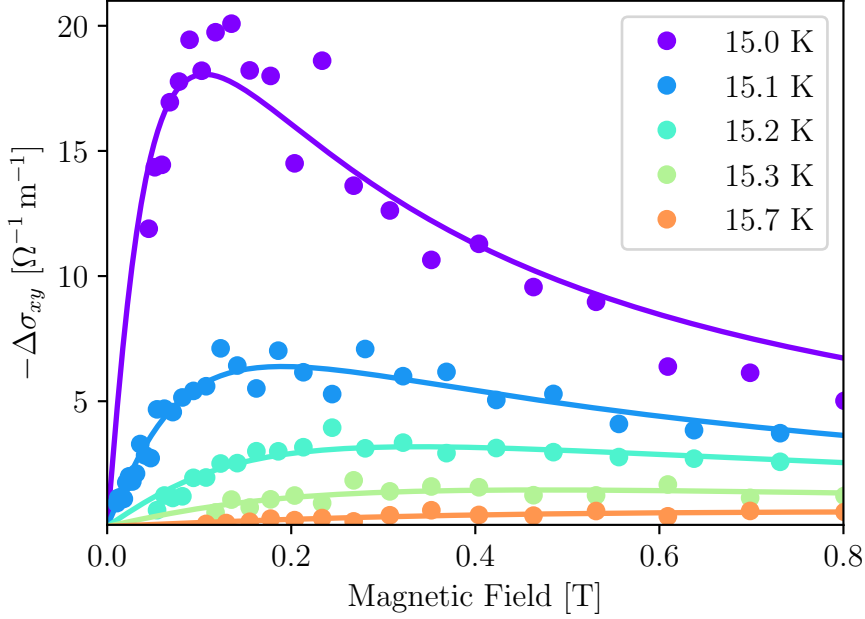


Fig. 3.6 The Hall conductivity $\Delta\sigma_{xy} = \sigma_{xy} - \sigma_{xy}^n$. Due to the proportionality of conductivity and resistivity for the Hall effect it looks similar to $\Delta\rho_{xy}$ shown in figure 3.5. Solid lines are fits to the theoretical model but should be viewed as guides to the eye.

It is important to note, however, that the quantity $\Delta\rho_{xy}$ does not have a physical meaning, it is not the true resistivity of the superconducting fluctuations, but merely a difference of two resistivities. The electron quasiparticles and the superconducting fluctuations are two parallel conduction channels for charge transport. In such a case the quantity that does add is the conductivity. That means for the measured conductivity that $\sigma_{xy} = \sigma_{xy}^n + \Delta\sigma_{xy}$, where σ_{xy}^n is the normal state conductivity and $\Delta\sigma_{xy}$ is the true contribution of the superconducting fluctuations. We thus subtract the normal state Hall conductivity, which in our case where there is virtually no magnetoresistance can be taken as the value at 9 T, from the measured Hall conductivity. This quantity, $\Delta\sigma_{xy}$, is displayed in figure 3.6. The figure shows strong similarities to figure 3.5 due to the proportionality of σ_{xy} and ρ_{xy} . Furthermore the data shows similarities to results obtained on the Nernst effect, specifically the contribution of superconducting fluctuations to the Nernst signal [33]. There the usual next step is to plot the Nernst coefficient ν . Inspired by this the same data as shown in figure 3.6 is plotted again in figure 3.7 as $\nu_H = \Delta\sigma_{xy}/B$, the Hall version of the Nernst coefficient. For low magnetic fields the values of ν_H are constant at values $\nu_{H,0}$ until a magnetic field B^* , at which the

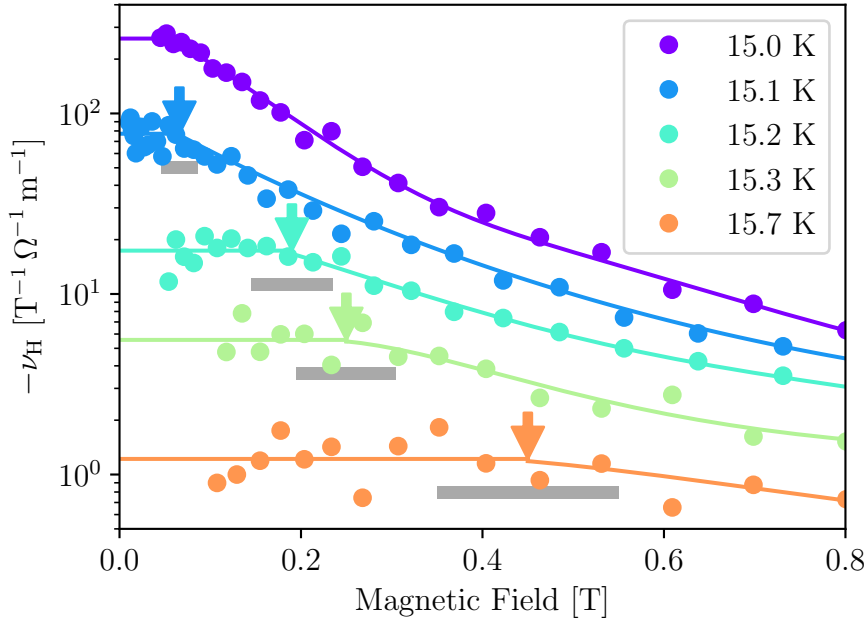


Fig. 3.7 The value $\nu_H = \Delta\sigma_{xy}/B$ on a logarithmic scale. For magnetic fields lower than a field B^* (indicated by arrows) the curves remain constant at zero-field values $\nu_{H,0}$. For higher fields they drop off rapidly. Solid lines are guides to the eye. The grey bars indicate the uncertainties of the corresponding B^* . For the isotherm of lowest temperature the constant plateau is not reached and the constant line corresponds to the lower limit.

isotherms start to decline towards lower values. This decrease is happening quite fast, as evidenced by the logarithmic scale.

The magnitude of $\nu_{H,0}$ as a function of the parameter $\epsilon = \ln(T/T_c)$ is shown in figure 3.8. Over less than 1 K the magnitude decreases by more than two orders of magnitude. We compare the Hall signal to the paraconductivity $\Delta\sigma_{xx} = \sigma_{xx} - \sigma_{xx}^n$, the difference of the measured conductivity as shown in figure 3.3 and the normal state conductivity, assumed to be given by the conductivity at 9 T. It is evident that the paraconductivity decreases much slower upon increasing T . This difference is quantified mathematically as a $\propto \epsilon^{-1}$ behaviour for the paraconductivity and a $\propto \epsilon^{-2}$ behaviour for the fluctuation Hall conductivity.

Finally the ghost critical field B^* , obtained as the field where ν_H deviates from $\nu_{H,0}$ is shown in figure 3.9. It increases linearly in ϵ for the measured temperature range. The error bars are relatively large and correspond to the 20 mK uncertainty for ϵ and to the grey bars in figure 3.7 for B^* .

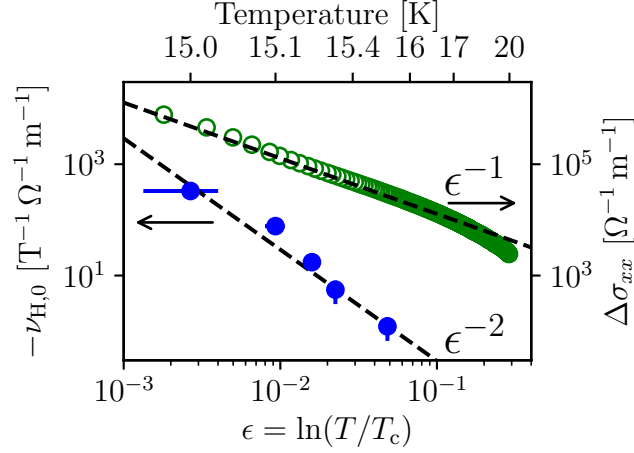


Fig. 3.8 The low-temperature value of ν_H , defined as $\nu_{H,0} = \Delta\sigma_{xy}/B$ when $B \rightarrow 0$, as function of ϵ (blue points, left axis). The values decay proportionally to ϵ^{-2} . In contrast the paraconductivity $\Delta\sigma_{xx}$ (green circles, right axis) decays only with ϵ^{-1} . The dashed lines are drawn according to the theoretical prediction, without any adjustable parameters. The error bars for $\nu_{H,0}$ in ϵ -direction correspond to an uncertainty in T_c of 20 mK. For $\Delta\sigma_{xx}$ the error bars are not shown, but along the ϵ -direction they would be of the same size as for $\nu_{H,0}$.

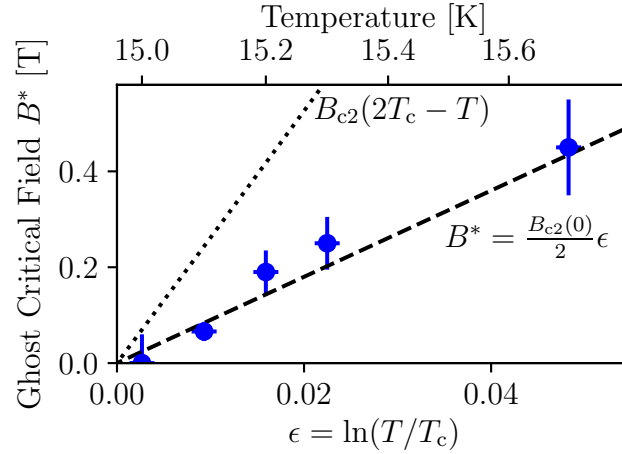


Fig. 3.9 The ghost critical field B^* as function of ϵ . Vertical error bars correspond to the grey bars in figure 3.7 while horizontal error bars correspond to an uncertainty in T_c of 20 mK. The dashed line corresponds to the predicted ghost critical field, while the dotted line corresponds to the mirror image of the critical field. The ghost critical field is clearly below the mirrored critical field.

3.4 Discussion

Recently a theoretical prediction has been made for the fluctuation Hall conductivity based on Gaussian fluctuation theory [124]. In a small range around the line of phase transition $T_c(B)$ and for small fields the equation can be written as

$$\Delta\sigma_{xy} = \frac{e^2 k_B T \kappa}{\pi \hbar d} \text{sgn}(B) \sum_{j=0}^{\infty} \frac{(j+1)(\zeta_{j+1} - \zeta_j)^3}{\zeta_j \zeta_{j+1} (\zeta_{j+1} + \zeta_j)^2}, \quad (3.3)$$

where

$$\zeta_j = \epsilon + \frac{\kappa \omega}{2} + \Psi \left(\frac{1}{2} + \frac{(j+1/2)4De|B| - i\omega}{4\pi k_B T} \right) - \Psi \left(\frac{1}{2} \right), \quad (3.4)$$

with the digamma function Ψ ,

$$\kappa = -\frac{d \ln(T_c)}{d\mu}, \quad (3.5)$$

and the diffusion constant D . The parameters κ and D are then normally used as fit parameters. This equation has already been successfully tested on TaN [121]. The data in figure 3.6 has been fitted with equation 3.3, which is shown as solid lines in the figure. They are, however, not a global fit and are thus to be seen as guides to the eye.

A simpler, clearer, and more straight forward way is to look at the low field limit of equation 3.3. It is given by

$$\frac{\Delta\sigma_{xy}}{B} = \frac{eD\kappa}{3} \frac{e^2}{16\hbar d} \frac{1}{\epsilon^2}, \quad (3.6)$$

the low field equation for $\Delta\sigma_{xy}$ in two dimensions for the Gaussian theory. The first term is a material-dependent prefactor unique to the Hall conductivity, the second factor is the Aslamazov-Larkin prefactor and is independent of the material, and the last factor describes the dependence on the temperature.

As opposed to equation 3.3, the factors D and κ are here combined into one single fit parameter. With some small calculations, however, this can be transformed into a known prefactor. For this purpose we substitute

$$D = \frac{v_F^2 \tau}{3} = \frac{2E_F \tau}{3m}. \quad (3.7)$$

In the case of $\kappa = -d \ln(T_c)/d\mu$ the substitution is a bit more complicated. We begin by applying the chain rule to obtain

$$\kappa = \frac{d \ln(T_c)}{d\lambda} \frac{d\lambda}{dN(0)} \frac{dN(0)}{dE_F} \frac{dE_F}{d\mu}, \quad (3.8)$$

where λ is the electron-phonon coupling constant and $N(0)$ is the density of states (states per volume and energy). By assuming $E_F = \mu$, the last term drops away. The second term can be evaluated as [134, 146]

$$\frac{d\lambda}{dN(0)} = \frac{\lambda}{N(0)}. \quad (3.9)$$

For the third term we make use of the standard equation [145]

$$N(0) = \frac{\sqrt{2m^3 E_F}}{\hbar^3 \pi^2} \quad (3.10)$$

from which the derivative can be calculated:

$$\frac{dN(0)}{dE_F} = \frac{1}{\hbar^3 \pi^2} \sqrt{\frac{m^3}{2E_F}}. \quad (3.11)$$

The second, third, and fourth term of equation 3.8 can thus be combined to

$$\frac{d\lambda}{dN(0)} \frac{dN(0)}{dE_F} \frac{dE_F}{d\mu} = \frac{\lambda}{2E_F}. \quad (3.12)$$

This means that κ can be expressed as

$$\kappa = -\frac{\lambda}{2E_F} \frac{d \ln(T_c)}{d\lambda}, \quad (3.13)$$

which means that $\kappa = \beta/E_F$ with a dimensionless parameter β .

The first term in equation 3.6 can thus be written as

$$\frac{eD\kappa}{3} = \frac{2e\beta\tau}{9m} = \frac{2\mu_H\beta}{9}, \quad (3.14)$$

where we have made use of the Hall mobility, which can be easily calculated from our Hall measurements, see equation 2.32: $\mu_H = 1.3 \times 10^{-5} \text{ T}^{-1}$. Equation 3.6 can then be written as

$$\frac{\Delta\sigma_{xy}}{B} = \frac{2\mu_H\beta}{9} \frac{e^2}{16\hbar d} \frac{1}{\epsilon^2}. \quad (3.15)$$

What is needed now is an equation to link T_c to λ in order to obtain a numerical value for β . In the weak coupling limit ($\lambda \ll 1$) this equation [8] is given by

$$k_B T_c = 1.13 \hbar \omega_D e^{-1/\lambda}, \quad (3.16)$$

which yields

$$\kappa = -\frac{1}{2\lambda E_F}, \quad (3.17)$$

or $\beta = -1/2\lambda$. The result already gives a good approximation of the data, but since our NbN films are not in the weak coupling limit [137], we look at a different formula to link T_c and λ : the McMillan formula [146]

$$T_c = \frac{\Theta}{1.45} \exp\left(\frac{-1.04(1 + \lambda)}{\lambda - \mu^*(1 + 0.62\lambda)}\right), \quad (3.18)$$

where Θ is the Debye temperature and μ^* is the Coulomb coupling constant accounting for the repulsive electron-electron interaction responsible for screening. The electron-phonon coupling constant λ for NbN and was found to be 1.1(1) according to a recent study [137], and μ^* is taken to be 0.13, a value typically used for NbN and other transition metal compounds [134, 146, 147]. This then leads to the value $\beta = -0.77$, or equivalently,

$$\kappa = \frac{-0.77}{E_F}. \quad (3.19)$$

All parameters of equation 3.15 are now known and can be compared with the data. The dashed line in figure 3.8 is drawn according to this equation. Thus, without any fitting parameters, an excellent agreement between the theory and the experiment is found.

For the paraconductivity the equivalent formula, the Aslamazov-Larkin formula, is given by equation 2.59. It is independent of material properties and depends only on the thickness of the film and the temperature. Without any additional calculations, all parameters of this equation are known. The validity of this formula is limited by the Ginzburg-Levanyuk number

$$Gi = \frac{e^2}{16\hbar d} \rho_{xx}^n. \quad (3.20)$$

There are slightly different ways of defining Gi , varying in small factors of order unity [28]. The criterion used here to define Gi is $\Delta\sigma_{xx} = \sigma_{xx}^n$, which is also used, for example, in Refs [148, 149]. The temperature range where equation 2.59 is valid

is $Gi < \epsilon \ll 1$. Using our parameters we obtain $Gi \approx 0.001$ and so we can see that equation 2.59 is in our case valid over almost three orders of magnitude.

Both quantities, $\nu_{H,0}$ and $\Delta\sigma_{xx}$, are well described by the theoretical prediction within the range of validity of the theory. The dip in $\Delta\sigma_{xx}$ upon approaching $\epsilon = 1$ is thus expected, as the theory is limited to lower temperatures, and typically observed in paraconductivity measurements [110, 150, 151].

It is clear from the excellent agreement of the paraconductivity with the prediction of the AL theory (see figure 3.8) that the conductivity is at least heavily dominated by AL fluctuations. Nonetheless a look at the other possibilities is appropriate. We first discuss the Halperin Nelson model (equation 2.69), which incorporates phase fluctuations.

In our case we have a very sharp transition where $T_c \approx T_{\text{BKT}}$ and thus τ_c is very small. Recently it was shown that the parameter b inside the tanh (which in that study is considered to be different from the prefactor b) depends linearly on τ_c . We are thus clearly in the Aslamazov-Larkin limit with $b\tau_c/\tau \ll 1$ and will discuss our results in the formalism of Gaussian fluctuations.

It now remains to answer the question of how relevant the MT contribution is compared to the AL contribution. The low mean free path would suggest that further scattering of electrons on fluctuations plays a minor role. A further indication of the relative insignificance is the absence of anything resembling a $\ln(\epsilon/\delta)$ behaviour. At the same time the relation of the Hall channel and the longitudinal channel for the MT theory reads [98, 152]

$$\frac{\Delta\sigma_{xy}^{\text{MT}}}{B} = -2\mu_{\text{H}}\Delta\sigma_{xx}^{\text{MT}}. \quad (3.21)$$

The relative insignificance of the MT contribution thus propagates to the Hall effect, where it is further decreased by a small mobility. In this channel as well no deviation from the ϵ^{-2} behaviour is found. The MT contribution is also less singular than the AL contribution [152]. A third influence on the superconducting fluctuations stems from the density of states (DOS) contribution. This contribution, however, is usually considered to be very small and is thus neglected [153].

A sign change in the Hall resistivity has been observed in many different materials. So far the explanation in these cases has involved vortices, or at least their influence could not be ruled out. In our case, however, we are clearly above T_c where vortices can not exist. This is another advantage of the very sharp superconducting transition. In the classical picture of the Hall effect, electrons get deflected by the Lorentz force. The sign change thus says that, once the electrons combine to form Cooper pairs, they are deflected into the opposite direction.

We now come to the last point of discussion, the ghost critical field B^* , which obtained its name due to it appearing as a ghost image of $B_c(T)$. This field scale originates as a crossover of two different length scales, of which one is dependent on the temperature and the other dependent on the magnetic field. The first one is the coherence length

$$\xi(T) = \frac{\xi_0}{\sqrt{\epsilon}} \quad (3.22)$$

and the second is the magnetic length scale

$$\ell_B = \sqrt{\frac{\hbar}{\alpha \epsilon B}}. \quad (3.23)$$

The parameter α is a numeric constant of order unity. Its precise definition varies slightly between different studies. In this way values of 1/2 [123], 1 [108, 154], 2 [155–158], and 4 [122] have typically been used, thus varying the magnetic length by a factor of $1/\sqrt{2}$, 1, $\sqrt{2}$, or 2, respectively.

There are thus two different regimes expected depending on which of the two length scales dominate. The crossover between the two regimes happens when $\xi(T) = \ell_B$. This implies for the ghost critical field, using equation 3.2 to relate $B_{c2}(0)$ and ξ_0 ,

$$B^* = \frac{\hbar}{\alpha \epsilon \xi_0^2} \epsilon = \frac{2B_{c2}(0)}{\alpha} \epsilon. \quad (3.24)$$

The ghost critical field thus depends linearly on the temperature, as long as the temperature is close to T_c . Furthermore it scales with the critical field, reflecting its ghost like behaviour of being a mirror image of the critical field.

It is not necessarily obvious of how to read the ghost critical field from the measured data. One possibility is to use the position of a peak. This is usually done in measurements of the Nernst effect, where the peak in the Nernst signal N is considered to indicate B^* [33, 154–158]. One problem of this definition is that this peak does not disappear upon approaching T_c and so a finite B^* is observed at T_c .

For this reason we decided to use an alternative approach and define the B^* to the field at which the value $\nu_H = \Delta\sigma_{xy}/B$ deviates from a constant low field behaviour.

We see (figure 3.9) that the ghost critical field scales indeed linearly in ϵ . We obtain $\alpha = 4$ when using our critical field $B_{c2}(0) = 18$ T, consistent with TaN thin films [122]. The observed ghost critical field is thus lower than the pure mirror image (dotted line in figure 3.9). The good agreement of the data with the prediction of the ghost critical field indicates that we do indeed observe a crossover

between two length scales in the region above T_c , of which one is a length scale directly related to superconductivity.

3.5 Conclusions

To summarize, we presented a study of the influence of superconducting fluctuations on the full conductivity tensor in a thin film of NbN. We could observe a sign change in the Hall resistivity caused by superconducting fluctuations in a small temperature window above T_c . For the low field limit of the Hall conductivity we find excellent agreement with Gaussian fluctuation theory. The same level of agreement to theory is also found in the paraconductivity. Different temperature dependences are observed for the two cases and both comparisons are done without having to fit any parameters. As a second result we could show the occurrence of a ghost critical field B^* , which depends linearly on the temperature and lies below the mirror image of the critical field.

The results of this chapter have been published in: D. Destraz et al., Phys. Rev. B **95**, 224501 (2017). The main contributions from the co-authors are the film growth by K. Ilin and assistance in writing the manuscript by J. Chang.

Chapter 4

Superconducting Fluctuations in Ultrathin NbN Films

“NbN does not exist.”

— Konstantin Ilin (KIT)

4.1 Introduction

Many properties in thin films are strongly dependent on the film thickness. This is also true for NbN. Quite dramatic differences are observed when going to thinner films around 3 nm. The phase diagram presented in figure 3.1 already gave an indication. Due to the stronger disorder effects upon decreasing the film thickness, a pseudogap phase is entered. The goal of this study is to investigate the superconducting fluctuations in the Hall resistivity when the film is in the pseudogap phase and to find connections to the cuprates. Despite the presumed connection of the pseudogap and phase fluctuations, the effects observed in cuprates usually go beyond the theories of phase fluctuations.

Figure 4.1 shows STM spectra for a NbN film in the pseudogap phase. Above T_c the spectra still show a dip around $V = 0$, which indicates the presence of a pseudogap. The pseudogap in NbN is very robust and remains intact across the superconductor insulator transition [159]. The pseudogap is thus present everywhere outside the superconducting phase in the B - T phase diagram. It has been predicted theoretically that for two- and three- dimensional superconductivity in a small range of ϵ the Aslamazov-Larkin behaviour, albeit with a different prefactor, can be found in strongly disordered systems with a large pseudogap [160]. The non-Gaussian part of the superconducting fluctuations depends strongly on the

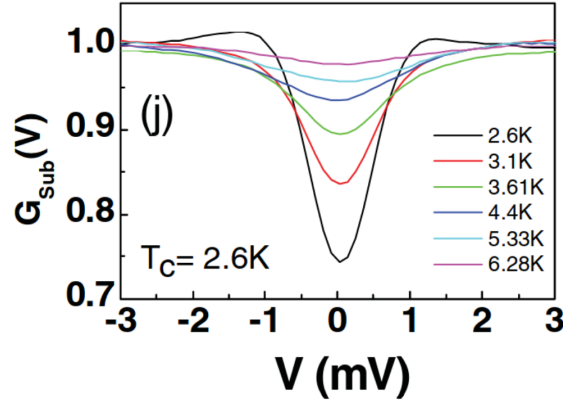


Fig. 4.1 STM spectra after background subtraction. Above T_c a pseudogap is observed. Taken from Ref. [117].

roughness and inhomogeneity of the investigated film [161]. This makes investigations inside the pseudogap regime in very thin films particularly challenging.

Experiments in ultrathin NbN films could show the presence of nanoscopic inhomogeneities leading to unusual properties. These inhomogeneities in the superconducting properties are not related to any structural inhomogeneities, which are much smaller, and exist even above the critical temperature inside the pseudogap phase. These very thin films of NbN have been found to host zero-dimensional superconducting fluctuations of the amplitude [162]. The data also supports a possible 0D-2D crossover upon approaching T_c . Such amplitude fluctuations are inconsistent with the appearance of a pseudogap. This paradox is explained with the confinement of the superconducting fluctuations instead of a more strict localization. In that study the threshold thickness to observe such behaviour is 2.2 nm. In the thinnest sample, a superconductor-insulator transition could be observed for high magnetic fields. In another study unconventional superconductivity with decreased or absent coherence peaks has been observed in NbN films thinner than 8 nm, lacking the strong pseudogap features and observing a reduced influence and even absence of vortices in the thinnest samples [163]. This suggests that phase fluctuations due to the thickness tuned superconductor-insulator transition play a significant role.

Another interesting phenomenon observed in very thin NbN is the BKT transition [164]. Besides superconducting fluctuations the resistivity above T_{BKT} can also be influenced by vortex fluctuations [100]. A crucial role is played by the vortex core energy, which in turn is influenced by the disorder in the film, leading to an increased energy cost for vortices for higher disorder. BKT transitions are also present in cuprates, including $\text{YBa}_2\text{Cu}_3\text{O}_7$, where it can be seen in single crystal films [165]. Good agreement with the Lawrence-Doniach theory of fluctu-

ations could be observed above T_c . In stripe ordered $\text{La}_{1.875}\text{Ba}_{0.125}\text{CuO}_4$ a purely two-dimensional BKT transition is observed [166]. The occurrence of the BKT transition in these materials is aided by the quasi-two-dimensional superconductivity in the layered cuprates.

The Hall effect inside a pseudogap phase has recently been investigated for cuprates in a theoretical study [167] in the strong pairing approach, but the more general results should apply also for NbN. Unfortunately, without a detailed band structure calculation the results are not suitable to describe the experimental observations quantitatively. Furthermore the sign change near T_c in the Hall resistivity is excluded from their considerations. The Hall conductivity of the fluctuations is found to reflect the underlying fermionic quasiparticles in its sign, meaning that no sign change is expected. At the pseudogap temperature T^* the Hall coefficient is expected to rise due to a reduction in the unpaired charge carriers, which is reflected in the term fermionic transport. This increase is then stopped abruptly close to T_c where the Hall resistivity drops sharply in the regime of bosonic transport, where the fluctuations influence the conductivity.

After much research the pseudogap in the cuprates is still not fully understood. Only recently, a significant jump in the carrier density could be observed from Hall effect measurements [168,169], together with a strongly negative thermal Hall conductivity [170]. Interestingly, the Hall coefficient scales with the pseudogap energy scale [171]. In this study we investigate very thin NbN films in the pseudogap regime. The aim is to gain more insight into the fluctuations and their connection to the pseudogap through Hall effect measurements. Combined influences from the BKT transition, the pseudogap, and Gaussian fluctuations of predominantly AL character are expected. The MT contribution in the Hall effect is less singular than the AL contribution and is not expected to play a role [152].

4.2 Methods

Multiple NbN films of thicknesses below 3 nm have been investigated. Due to the fast decay of the films we only show the results of two fresh films of thickness 2.3 nm, and 2.7 nm. Their growth process is the same as described in the last chapter. The 2.7 nm film is a part of the same batch as the film described in the last chapter. The 2.3 nm film is from a second batch. The growth parameters of the two batches are not exactly the same, leading to some differences in the superconducting properties between the films. The electrical connections and the measurement procedure follows the description of last chapter.

4.3 Results and Discussion

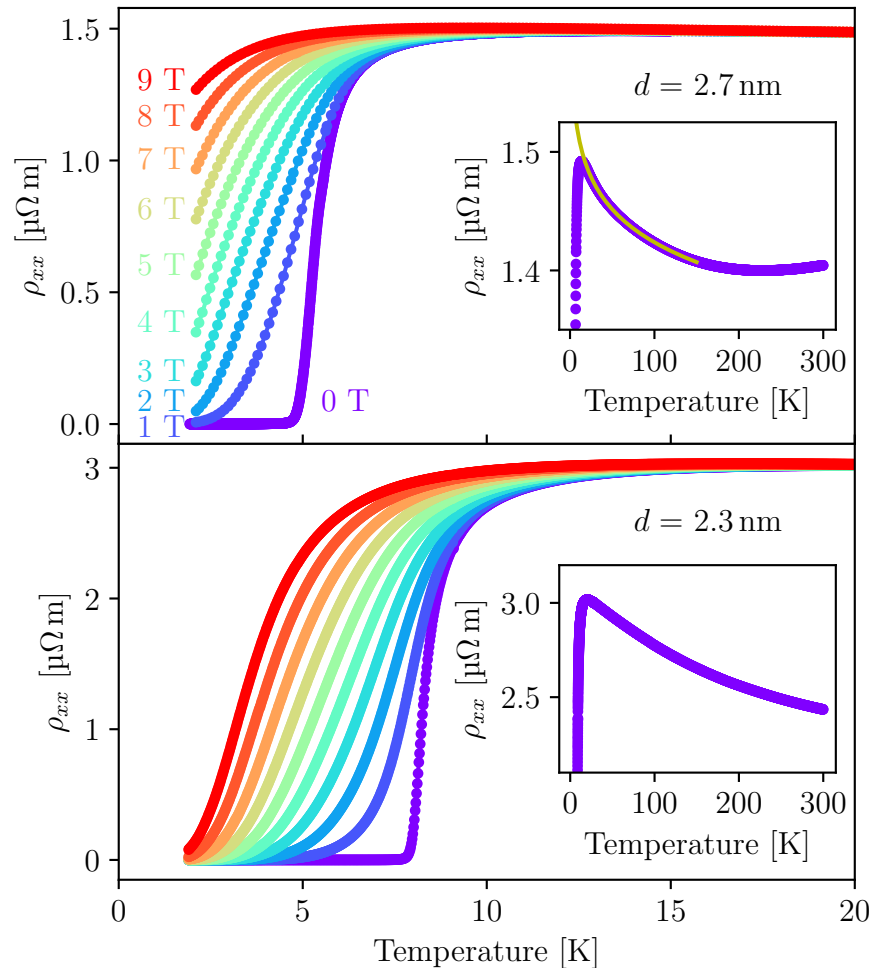


Fig. 4.2 Resistivity as function of temperature for magnetic fields as indicated for the two very thin NbN films. The insets display the temperature dependence above the transition, showing insulating behaviour in a large temperature range. The yellow lines are fits to equation 4.1.

The first step is to gain the relevant knowledge about the resistivity and whether we observe a BKT transition. Resistivity measurements on both films are shown in figure 4.2. The superconducting transitions take place around 5 K and 8 K for the two films. Above the transition insulating behaviour is found as shown in the insets. Nonetheless, the resistivity between room temperature and T_c varies only slightly, around 7% and 20% for the two films. In the insulating

region it can be described by

$$\rho(T) = a_3 \ln^3 \left(\frac{1}{T} \right) + a_1 \ln \left(\frac{1}{T} \right) + a_0, \quad (4.1)$$

an equation which is regularly used to fit insulating behaviour in thin superconducting films [162]. This fit is shown as yellow lines in the insets. For the 2.7 nm film this insulating behaviour extends up to around 150 K, where the resistivity starts to flatten off followed by an increase again upon increasing temperature. In the second film the insulating behaviour extends up to room temperature. The behaviour upon applying a magnetic field around the transition is shown in the main panel. Above the transition the resistivity is independent of magnetic field, no significant magnetoresistance is observed. The superconducting transition is much broader than in the thicker films of the last two chapters, extending over a range of about 1 K. This range increases even more for higher magnetic fields. In the absence of a magnetic field two different resistivity regimes are observed. This behaviour is shown in figure 4.3 on a logscale to visualize the very low resistivity regime. For the first film the onset of the superconducting transition is visible at around 6 K with the steepest part of the transition at 5.2 K. The resistivity curve then decreases until a clear bump is observed at 4.5 K. Around 2 K, the lowest temperature of the measurement, the resolution of the measurement hardware becomes a limiting factor. For the second film the onset of superconductivity occurs around 8.4 K, a much higher temperature than the first film despite this film being the thinner of the two. The kink occurs around 7.3 K and below 5 K the instrument resolution prevents the clear experimental confirmation of a further resistivity decrease. The resistivity curve of the film investigated in the last chapter is shown in yellow as a comparison.

The resistivity of the ultrathin films shown in figure 4.3 can be fitted below the kink with the formula

$$\rho_{xx} \propto \exp \left(-b/\sqrt{t} \right) \quad (4.2)$$

with the dimensionless temperature

$$t = \frac{T - T_{\text{BKT}}}{T_{\text{BKT}}}. \quad (4.3)$$

This equation describes the resistivity behaviour above a BKT transition. From the fit we obtain the temperature $T_{\text{BKT}} = 1.50(2)$ for the first film and $T_{\text{BKT}} = 1.5(4)$ for the second. The fits are shown as red lines in figure 4.3 and agree well with the measured data over most of the range between the temperature of the resistivity kink and the temperature where the signal becomes too small to measure. In a plot with a logarithmic ordinate this formula will always result

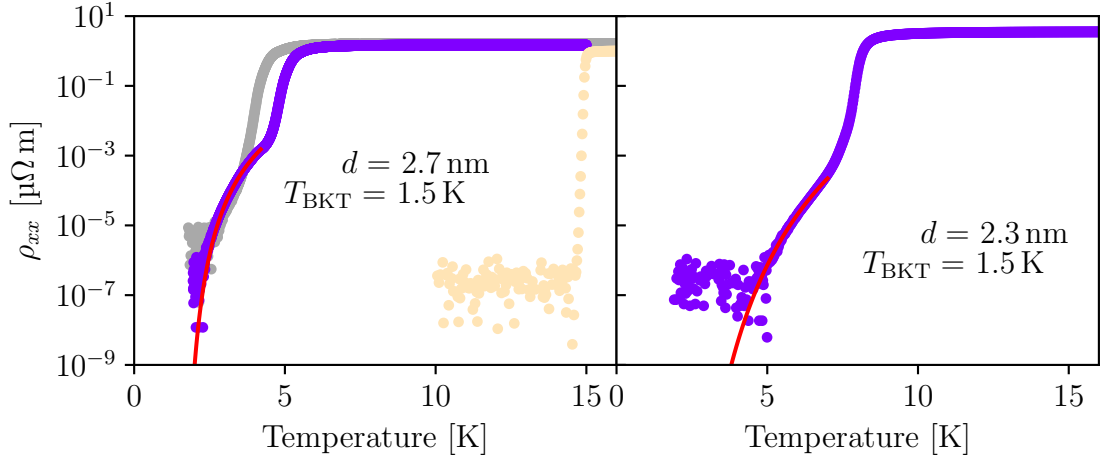


Fig. 4.3 Resistivity as function of temperature on a logscale plot. The measurements (violet points) display the BKT regime below 4.5 K and 7.3 K, respectively. As an illustrative example the data measured on the aged version of the first film is shown in grey. It exhibits a very different resistivity behaviour with a different T_c . The data of the film presented in the last chapter is also shown as comparison in yellow. The solid red lines are fits to equation 4.2.

in a negative (clockwise) curvature. The data around the kink is thus clearly inconsistent with a BKT behaviour. We can thus conclude from this analysis that we observe a BKT behaviour and that the kink in the resistivity curves marks the end of the BKT regime. The BKT transition in NbN films is a well-known phenomenon. We investigate it here again as the resistivity is the starting point for the investigations of the superconducting fluctuations in the Hall effect. To illustrate the problems caused by film decay the first panel of the figure also shows the resistivity of the same film at a later time in grey. At this point the film decay has shifted the resistivity curve to lower temperatures. The BKT regime can also not clearly be distinguished any more.

Next we take a look at the paraconductivity. It is calculated by subtracting the extrapolated normal state conductivity according to equation 4.1 from the measured conductivity. The resulting $\Delta\sigma_{xx}$ is shown in figure 4.4 for both films over a large range in ϵ . Over one and a half orders of magnitude of ϵ the paraconductivity follows a straight line in the log-log plots, corresponding to a power-law.

First the 2.7 nm film is discussed. The critical temperature used is 4.8 K which is chosen because it extends the power law region over the largest range of ϵ and corresponds well with the resistivity measurements, as seen in figure 4.3(a). Figure 4.4 shows two lines obtained from the AL theory for different dimensions.

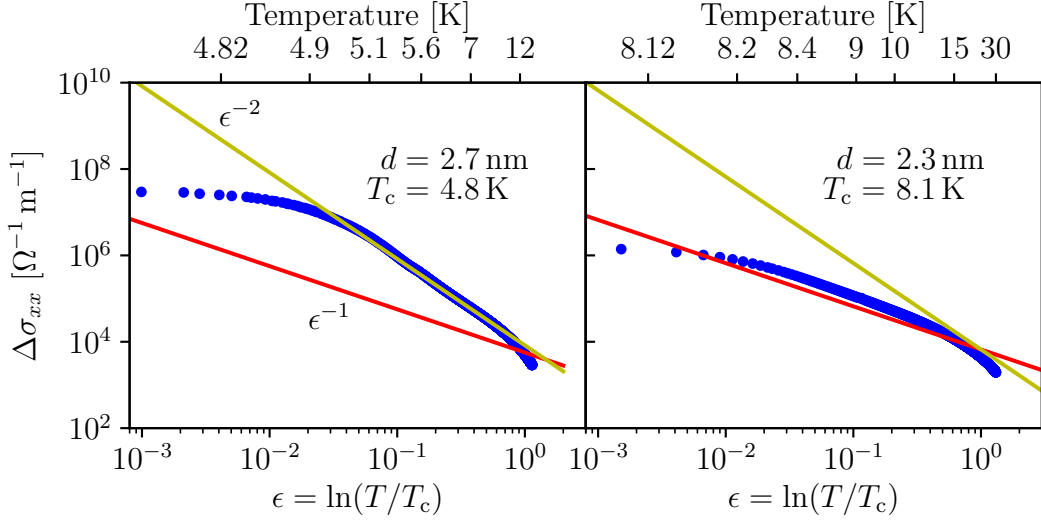


Fig. 4.4 Paraconductivity vs reduced temperature ϵ on a log-log scale, with the regular temperature shown in the upper abscissa. Yellow lines correspond to the 0D Aslamazov-Larkin prediction (equation 4.4). Red lines correspond to the 2D AL prediction (equation 2.59).

The curves correspond to the zero-dimensional (yellow line) and two-dimensional (red line) AL theory. The zero-dimensional theory works well in this case. It can be described by [162]

$$\Delta\sigma_{xx} = \frac{\bar{\gamma}e^2}{16\hbar d} \frac{1}{\epsilon^2}. \quad (4.4)$$

The dimensionless factor $\bar{\gamma}$ is the fitting parameter used and evaluates to 1.5. It is linked to the coherence length as

$$\bar{\gamma} = 4\pi \left(\frac{\xi_0}{\ell_{\text{sg}}} \right)^2. \quad (4.5)$$

The length ℓ_{sg} determines the size of a supergrain over which the superconducting fluctuations are confined. For our value of $\bar{\gamma}$ it then evaluates to $\ell_{\text{sg}} \approx 3\xi_0$. For 0D fluctuations a length ℓ_{sg} on the order of, or larger than, the coherence length is expected for consistency. Our result for ℓ_{sg} fulfils this requirement. If this were not the case, the different superconducting regions could couple together and the zero-dimensionality would be lost. Since $\bar{\gamma}$ is a multiplicative term it only shifts the yellow curve up or down without changing the form of the function, giving strong support that the agreement between the fit and the data is not just coincidental. The observation of zero-dimensional fluctuations does not mean that the film itself is granular but instead that superconducting fluctuations are confined to certain

regions. Changing the value of T_c could not recover any power law behaviour consistent with two-dimensional fluctuations or any other exponent.

Next the paraconductivity of the second film is discussed. The zero-dimensional fluctuations can not be observed in this film. Instead the two-dimensional AL behaviour is found over 1.5 orders of magnitude in ϵ . This indicates that the superconducting properties are more homogeneous across the sample. Since the superconducting inhomogeneities should not be connected to the inhomogeneity of the sample it is not an easy task to tell which growth properties lead to such a difference in behaviour.

No influence of phase fluctuations can be observed above T_c , despite our films being in the pseudogap phase [172]. A further contribution expected in the case of a pseudogap are DOS corrections, which could also not be observed [20]. The observation of zero-dimensional amplitude fluctuations in the first film, although inconsistent with the expected phase fluctuations, are thus consistent with earlier reports on NbN [162]. A possible explanation for the absence of the 0D fluctuations in the second film is linked to the same effects that lead to a higher T_c .

Due to the decay of the 2.7 nm film, the further measurements are only available for the 2.3 nm film. The Hall resistivity as a function of temperature is shown in figure 4.5 for different magnetic fields for the 2.3 nm film. For high temperatures the Hall resistivity is temperature independent but depends strongly on the magnetic field, which is the expected quasiparticle behaviour. For temperatures lower than ≈ 20 K a small increase in resistivity upon cooling can be observed, which gets more pronounced around 10 K for the lowest fields and at lower temperatures for higher fields. A zoom on the low-temperature region is shown in the lower panel of the figure. Here it can clearly be seen that after the first positive peak a negative peak is present at even lower temperatures. This second peak is smaller than the positive peak but still clearly visible.

To get a better understanding of the temperature dependence of the different peaks and zero-crossings, figure 4.6 shows a diagram of these quantities. All peaks and zero crossings shift towards lower temperatures upon applying a magnetic field and no clear difference in the way how they shift can be determined. Only at low magnetic fields the behaviour is a bit different.

Sign changes in the Hall effect can originate from different processes. In chapter 3 we showed how this sign change is driven by superconducting fluctuations. The vortex motion is the most obvious alternative contribution. Different signs of this contribution have been observed in different materials [98, 173, 174]. A third process that can drive sign changes is the topological Hall conductivity [175]. This process is an unlikely origin, as the band structure of NbN is not topological. Pure Nb films also display a sign reversal in the Hall from a positive sign in the normal

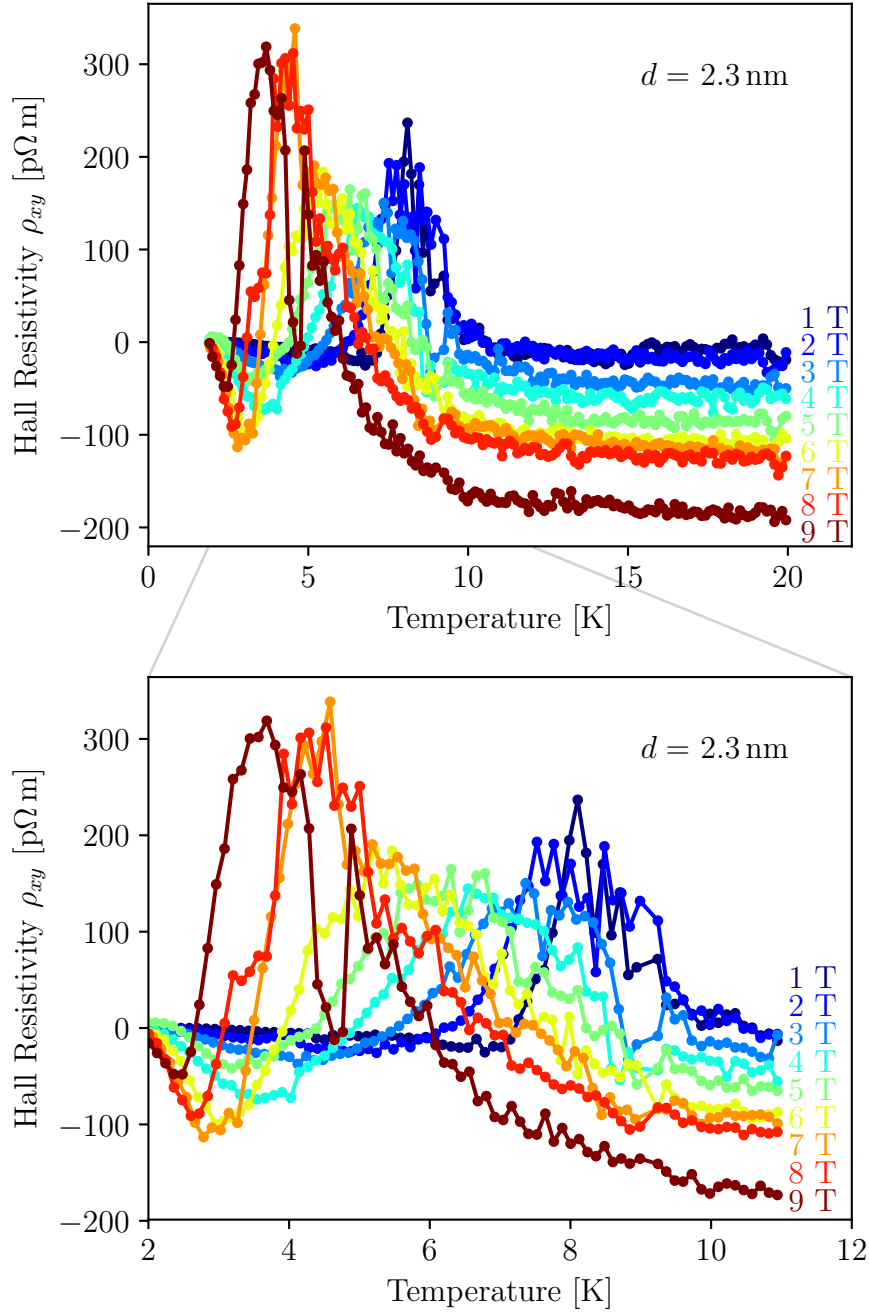


Fig. 4.5 Hall resistivity as a function of temperature for different magnetic fields as indicated. Multiple peaks and sign changes appear. The bottom panel zooms on the range of the sign changes. A jump in all curves at 9.1 K has been removed.

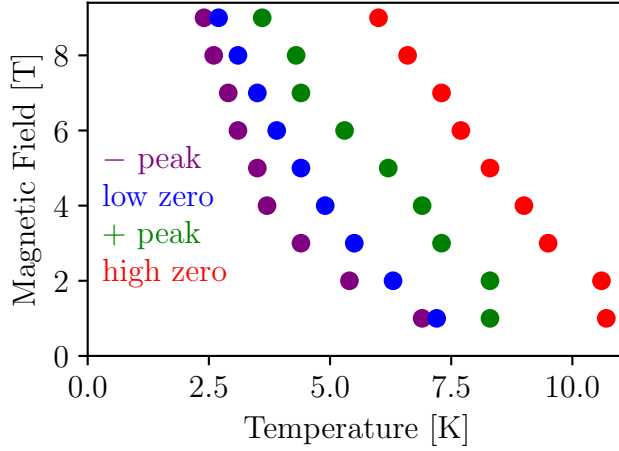


Fig. 4.6 Diagram showing the position of the negative and positive peaks and the two zero-crossings.

state to a negative sign below T_c , which is attributed to vortex motion [176]. The same positive and negative peaks that we see have been observed for $\text{YBa}_2\text{Cu}_3\text{O}_{7-\delta}$ with the difference of a positive Hall signal at higher temperatures due to the charge carriers being holes [177]. This also results in the lack of the higher zero crossing. On the other hand a double sign change has also been reported for Nernst effects measurements in the pseudogap phase of cuprates [19]. A difficulty in relating NbN to the cuprates is the difference in charge carriers. While NbN is an electron like material, the hole doped cuprates show the opposite behaviour. As the character of the charge carriers might be important for the fluctuations, this difference must be taken into account [167].

With reasonable confidence the positive peak in our measurement can be attributed to superconducting fluctuations, predominantly of Gaussian nature. Whether their dimensionality replicates what is found in ρ_{xx} and hence depends on the superconducting inhomogeneities can not be determined from the data presented. The negative peaks below T_c are most likely due to vortex motion.

4.4 Conclusions

To conclude we have shown how the BKT transition impacts the resistivity and reproduced in one sample the zero-dimensional AL fluctuations as observed by another group. In the Hall effect we found deviations from the linear quasiparticle behaviour. We furthermore find more sign changes and clear differences to what is expected in the Gaussian theory of fluctuations. The experiments are challenging

due to the decay of the samples and the strong dependence of their properties on growth conditions. Nonetheless we can say that the Hall effect in NbN shows strong similarities to the Hall effect in the underdoped cuprates and further measurements on very thin NbN film, although very challenging, will probably be worth the effort. I end this chapter with the same quote that started it, as it summarizes all the problems we encountered in a very concise way: “NbN does not exist.”

Chapter 5

High-Field Electronic Transport in NbN Films

5.1 Introduction

The high field regime (quantum regime) of superconductors (see figure 5.1), that is close to $B_{c2}(0)$, features interesting quantum phenomena. In this chapter a combined study of the search for superconducting fluctuations and resistivity scaling around the quantum critical point is undertaken.

5.1.1 Quantum Critical Scaling

Upon destruction of the superconducting state many materials enter a metallic state. In some materials, however, for low temperatures an insulating state is entered instead. Of special interest in the quantum region is the superconductor-insulator transition, a prime example of a quantum phase transition [178]. It is typ-

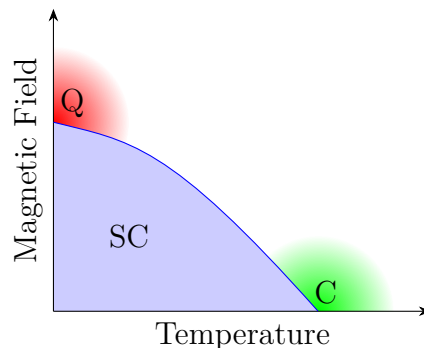


Fig. 5.1 Phase diagram illustrating the classical (C) and quantum (Q) regions of the fluctuations outside of the superconducting (SC) phase.

ically found in thin films but can be observed in one-dimensional nanowires [179]. In temperature scans it manifests itself as a curve which for low temperatures is independent of temperature. Such a curve occurs only for one specific magnetic field B_c . For magnetic fields higher than B_c the curves display insulating behaviour, turning up towards higher resistivities for decreasing temperatures. For curves lower than B_c , metallic behaviour is observed, with the curves turning down towards lower resistivities upon cooling. This second region below B_c is the region in which superconductivity is observed. The value of $\rho_{xx,c}$ is usually close to the normal state resistivity, but significantly lower values have also been observed, especially in the disordered limit [180,181]. It is also in this limit, where the universal value for the sheet resistance $R_{\square,u} = h/4e^2 = 6450 \Omega/\square$ has been observed, while in the less disordered systems, the critical resistance is determined by the normal state resistance and can thus deviate significantly from $R_{\square,u}$ [182]. Variation in purity has also been shown to turn first order transitions into second order transitions upon increasing disorder in semiconductor based superconductors [183].

The study of the magnetic field tuned superconductor-insulator quantum phase transition can reveal much about the underlying processes of superconductivity. A recent study found a sequential transition from superconductor to Bose insulator to Fermi insulator in α -WSi, marked by two subsequent critical points [184]. Superconducting fluctuations could be observed between the two transitions, disappearing at a tricritical point. This shows how the bosonic Cooper pairs can exist on the insulating side of the SIT.

For a two-dimensional superconductor the resistivity is expected to follow a curve described by

$$\rho_{xx}(B, T) = \rho_{xx,c} F \left(\frac{|B - B_c|}{T^{1/z\nu}} \right), \quad (5.1)$$

where F is the single variable scaling function describing the shape of the curve [185]. It is thus not a function of the field and temperature separately, but of a combined parameter, leading to the collapse of different isotherms for proper scaling with $z\nu$. The quantity $z\nu$ is a product of two critical exponents, one being the dynamical exponent z , the other being the correlation length exponent ν . To determine the two exponents separately, this equation alone is thus inadequate. A similar equation is used to describe the dependence of the resistivity on the electrical field:

$$\rho_{xx} = \rho_{xx,c} \tilde{F} \left(\frac{|B - B_c|}{E^{1/(z+1)\nu}} \right), \quad (5.2)$$

with a different scaling function \tilde{F} . This equation alone has the same problem of not being able to disentangle the two exponents z and ν . With a combined analysis of measurements of field sweeps at different temperatures with field sweeps

at different electrical fields it is then possible to extract z and ν separately. It is important to note, that these two scaling functions are only valid in a small region around the critical point and significant deviations of the data from the equations are expected at larger distances.

The origin of the two critical exponents z and ν are the scaling behaviours of two quantities related to superconductivity: first the correlation length ξ , and second the correlation time τ . Both of these quantities diverge at the superconducting transition and it is this divergence that is described by the two critical exponents:

$$\xi \propto |x - x_c|^{-\nu} \quad (5.3)$$

and

$$\tau \propto \xi^z \propto |x - x_c|^{-z\nu} \quad (5.4)$$

for some control parameter x , which can be, for example, the magnetic field, the thickness of the film, or the disorder [186]. The parameters ξ and τ thus depends on the proximity of the control parameter to its critical value x_c .

This quantum critical point influences the Hall effect in a very similar fashion to the resistivity and an equivalent crossover point can be observed in ρ_{xx} and ρ_{xy} [181, 187]. The Nernst effect is a further probe where such a crossover can be observed and used to perform a scaling analysis of the transverse Peltier coefficient α_{xy} [188].

It is of interest to investigate these scaling properties under very high magnetic fields, as such measurements are usually performed on materials with much smaller critical fields. Furthermore the interplay with superconducting fluctuations in the Hall channel can be investigated.

5.1.2 Superconducting Fluctuations

In the spirit of the last two chapters we are also interested in how the fluctuations influence the Hall effect in the quantum region. The fluctuations expected in the quantum region are obtained from the same theory of Gaussian fluctuation as in chapter 3 [124]. There are two relevant limiting cases applicable in the quantum region. The first one is

$$\Delta\sigma_{xy} = \frac{2e^2 \text{sgn}(B)}{\pi \hbar d} \left(\frac{\kappa}{2} k_B T - \frac{21 k_B T}{8 E_F} \right) \frac{1}{\ln \left(\frac{B}{B_{c2}} \right)}, \quad (5.5)$$

valid around $B \approx B_{c2}$ for measurements in T direction. The second case is

$$\Delta\sigma_{xy} = \frac{e^2 \text{sgn}(B)}{2\pi^2 \hbar d} \left(\omega_c \tau - \frac{\kappa \Omega_c}{3} \right) \ln \left(\frac{1}{\ln \left(\frac{B}{B_{c2}} \right)} \right), \quad (5.6)$$

valid for very low temperatures for measurements of increasing B . Both of these equations start with a material-independent prefactor depending only on the thickness d , followed by a factor which depends on either the temperature or the magnetic field. Both of these factors can be positive, negative, or even zero, as they each contain one factor that is a difference of two terms. In the first equation the sign is determined by the Fermi energy E_F and the parameter $\kappa = -d \ln(T_c)/d\mu$. In the second equation, the two cyclotron frequencies $\omega_c = |eB/m|$ and $\Omega_c = |4eBD|$ are used to compute the middle factor, which both depend linearly on the magnetic field. The parameter ω_c describes the quasiparticles (electrons and holes), while Ω_c describes the diffusive regime. The last factor in both equations then describes the magnetic field dependence as either an inverse logarithm or the logarithm of an inverse logarithm. The magnetic field takes the place of the temperature in the factor $\epsilon = \ln(T/T_c)$, as it appears in the classical fluctuation region. These two equations thus predict a divergence of the superconducting fluctuations upon approach of B_{c2} from above. The validity of this theory of Gaussian fluctuations has so far only been tested in the classical region. It is thus of great interest to investigate this regime experimentally.

5.2 Methods

The measurements were performed at the high magnetic field laboratory in Grenoble. A resistive magnet capable of reaching 35 T was used. Two films were measured simultaneously, one of them was the same film on which chapter 3 is based on ($d = 11.9$ nm), the second one is a film of slightly different thickness ($d = 11.5$ nm). In order to fit onto the sample holder, both films had to be made slightly smaller in both dimensions of the plane. This was done by filing away the film with the substrate with a diamond file. Care was taken to ensure symmetry of the remaining contacts. The sample was glued onto the holder with Stycast two component epoxy, as other attempted methods resulted in the sample detaching, most likely caused by the rapid cooling upon inserting the variable temperature insert into the He bath. An AC current source and lock-in amplifiers were used to measure both the longitudinal and Hall voltages. The current leads of the samples were attached in series with a $1 \text{ M}\Omega$ resistor in order to enforce a stable and constant current through the sample independent of its momentary resistance. Cooling was

achieved by a dilution refrigerator and the current through the samples were chosen small enough to avoid Joule heating. All field sweeps were performed at very low dB/dt slopes to reduce heating effects from induced currents. As a result only a single isotherm could be recorded per night. The magnetic field was oriented perpendicular to the film planes in all measurements.

5.3 Results and Discussion

5.3.1 Quantum Critical Scaling

The longitudinal resistivity ρ_{xx} is shown in figures 5.2(a) and 5.3(a) for a range of magnetic field close to the critical field $B_{c2}(0)$ for the three different temperatures 50 mK, 120 mK, and 400 mK. As expected, the slope shifts towards lower magnetic fields upon increasing the temperature. The normal state resistivity of about $0.97 \mu\Omega \text{ m}$ of the thicker film is consistent with the results found in the low-field measurements and confirms the absence of any sizeable magnetoresistance. The superconducting transition is noticeably wider than in the low-field measurements, stretching over $\approx 2 \text{ T}$. The inset shows the same data zoomed to the point where all isotherms cross the same point. This point gives the critical field $B_c = 20.94(3) \text{ T}$ and the critical resistivity $\rho_{xx,c} = 0.9630(3) \mu\Omega \text{ m}$ for the thicker of the two films, while for the thinner film the values are $B_c = 21.58(5) \text{ T}$ and $\rho_{xx,c} = 0.6729(8) \mu\Omega \text{ m}$. These values can be converted into sheet resistances by dividing with the thickness: $R_{\square} = \rho_{xx}/d$. The corresponding values of $80.92(3) \Omega/\square$ and $58.51(7) \Omega/\square$, respectively, deviate significantly from the universal value $R_{\square,u}$, which is not uncommon. All uncertainties given here are the uncertainties of reading off the crossing point from the data and do not incorporate any systematic uncertainties. The critical fields obtained in this way are slightly higher than the critical field extrapolated from the WHH relation (equation 3.1).

In order to obtain $z\nu$, the parameter

$$t = T^{-1/z\nu} \quad (5.7)$$

is first obtained for each curve as follows: An arbitrary value of t is chosen for one isotherm. The arbitrariness of this factor originates from the function F , which can absorb any constant factors. The other isotherms are then multiplied with any factor t such that the curves visually coincide when plotted according to equation 5.1. The value of t obtained this way is then plotted against the temperature T , as is shown in the insets of figures 5.2(b) and 5.3(b) as a log-log plot. This is subsequently fitted with a power law according to equation 5.7. In the log-log plot it appears as a straight line and its slope corresponds to $-1/z\nu$.

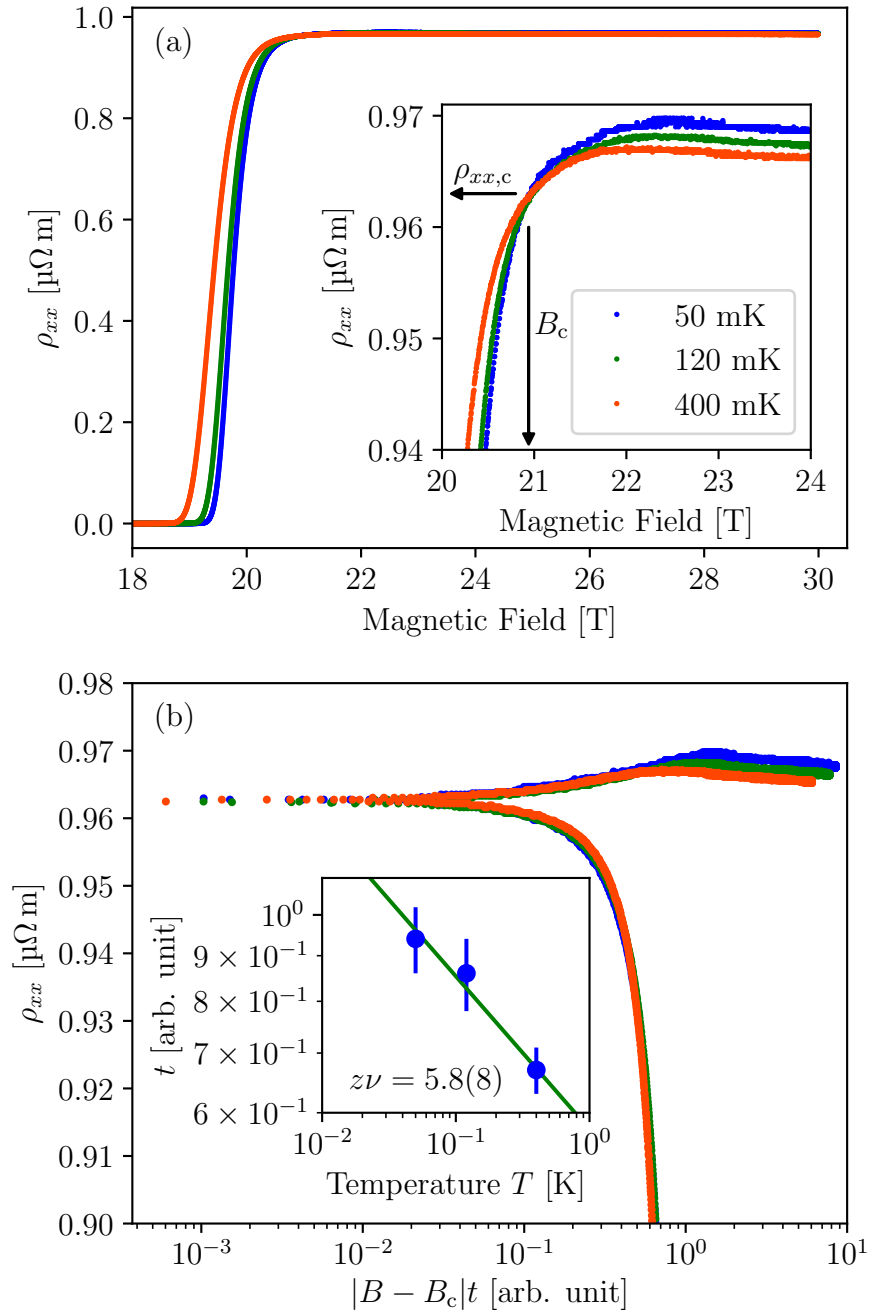


Fig. 5.2 (a) Resistivity isotherms of the thicker film ($d = 11.9\text{ nm}$). The curves shift towards lower magnetic fields as the temperature increases. The inset zoom to the critical point, where all isotherms meet at $B_c, \rho_{xx,c}$. (b) The scaled resistivity. All isotherms collapse into a single curve. Inset: Log-log plot of the parameter t against Temperature T . The straight line corresponds to a power law, from which the critical exponent $z\nu = 5.8(8)$ is obtained.

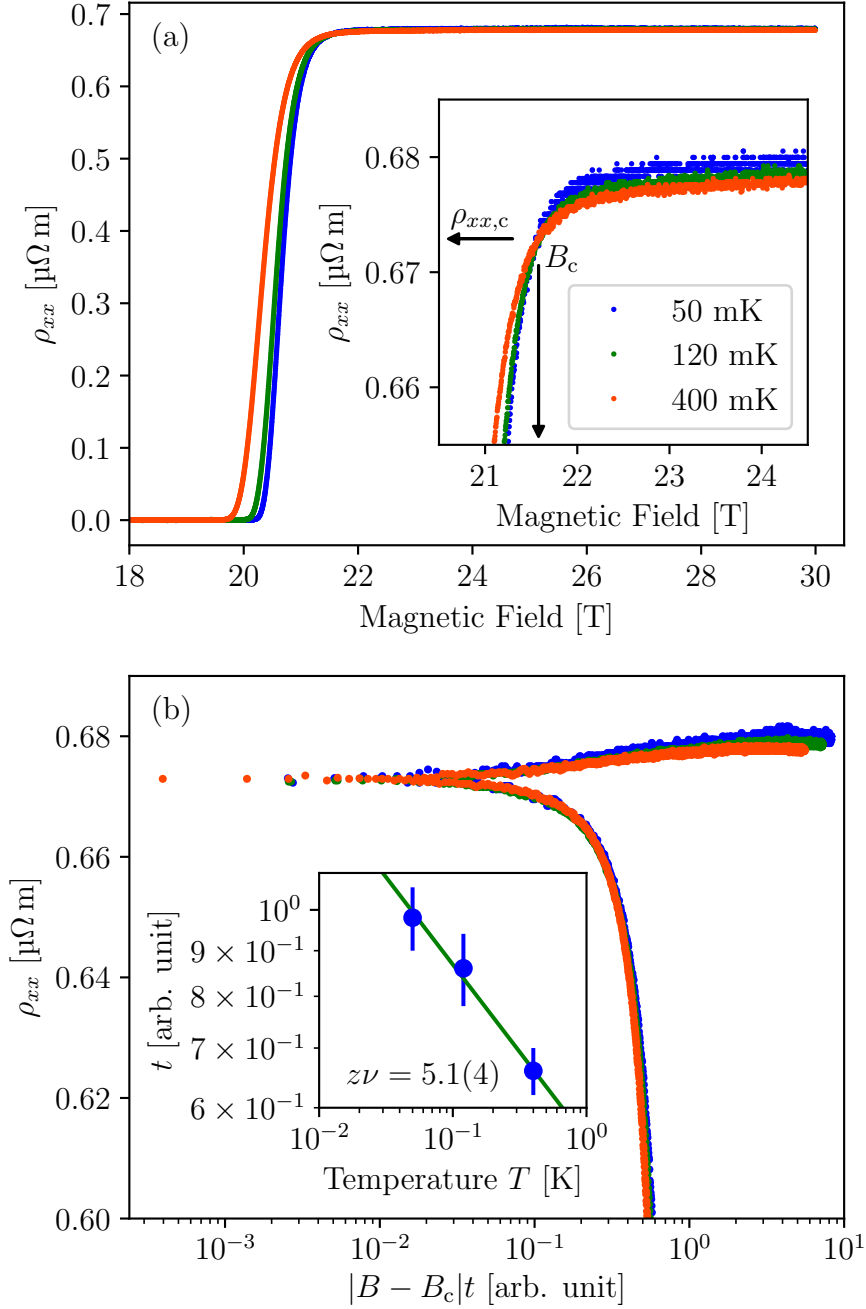


Fig. 5.3 (a) Resistivity isotherms of the thinner film ($d = 11.5$ nm). The curves shift towards lower magnetic fields as the temperature increases. The inset zoom to the critical point, where all isotherms meet at $B_c, \rho_{xx,c}$. (b) The scaled resistivity. All isotherms collapse into a single curve. Inset: Log-log plot of the parameter t against Temperature T . The straight line corresponds to a power law, from which the critical exponent $z\nu = 5.1(4)$ is obtained.

From these data $z\nu = 5.8(8)$ and $5.1(4)$ can be extracted for the two films. The value of $z\nu$ can often be used to gain insight into the underlying processes leading to the QCP. The Boson scenario, for example, is indicated by $z\nu = 4/3$, while the pair-breaking fermionic scenario is indicated by $z\nu = 2/3$ [184]. This $z\nu = 2/3$ has also been observed in ultrathin NbN films with lower critical temperatures and lower critical fields [162]. In comparison to other reports of $z\nu$ the value found here is unusually large and it must thus be explained differently.

Higher values of $z\nu$ can for example be observed in Quantum Griffiths singularities, which have been observed in a variety of materials. These include, for example, thin films of Ga [189], LaAlO₃/SrTiO₃ interfaces [190, 191], ion-gated ZrNCl and MoS₂ [192], and quasi-one-dimensional Ta₂PdS₅ nanowires [193]. Although critical behaviour usually depends only on the universality class of the transition and is independent of the microscopic details, this singularity is caused by disorder effects. It is characterized by the divergence of the dynamical critical exponent z , which manifests itself in the $\rho_{xx}(B)$ curves as a shift of the crossover field B_c towards lower fields for higher temperatures. The value B_c is thus not a constant of the temperature anymore. The divergence occurs in form of a power law which can be expressed as

$$z\nu \propto (B_c^* - B_c)^\alpha \quad (5.8)$$

with an exponent $\alpha < 0$ and thus depends on the distance of the observed crossover field $B_c(T)$ to the true zero field crossover field B_c^* . At B_c^* the quantity $z\nu$ then reaches ∞ . This also leads to a deviation from the WHH behaviour [189, 194]. While such a shift can, however, not be observed in our measurements, it can not be fully excluded due to the limited temperature range for which data are available.

5.3.2 Alternative View on the Transition

A second way to investigate the superconducting transition is by looking at the steepest part of the resistivity curve, as was done in the previous chapters. The critical field as defined by the steepest part will be denoted by B_{c2} like in the previous chapters. Due to the location of the crossover from insulator to superconductor, this transition must be located at lower magnetic fields than the QCP. The location of B_{c2} is less influenced by the quantum critical point the further away it is from it in field and temperature. Therefore the measurement at 400 mK is least affected by the QCP. The value of B_{c2} as function of temperature are displayed in figure 5.4. A noticeable slope is still present in the low temperature region, comparable in size to the high-temperature region. The inset zooms closer

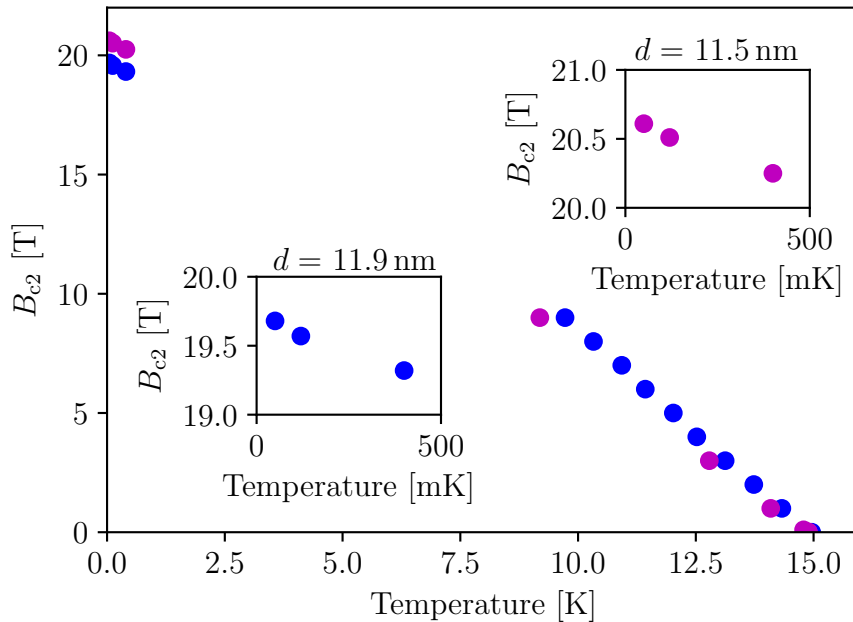


Fig. 5.4 Upper critical magnetic field B_{c2} as defined by the steepest part of the transition for both films. For the $d = 11.9$ nm film the data measured below 9 T is the same as shown in figure 3.3. The insets zoom to the low-temperature region.

on this low-temperature region. This behaviour is clearly not anticipated by the WHH theory. For the high-field measurements, the values of B_{c2} are slightly higher than the values for the thinner film at the same temperature. For the low-field measurements this is reversed. The reason for this is not clear, but different degradation of the films over time is the most likely reason. A small shift could also originate from slightly different temperatures of the two samples.

5.3.3 Hall Effect

The Hall resistivity ρ_{xy} for both films is shown in figure 5.5. Above the critical magnetic field the Hall resistivity is linear in field with no offset from zero as evidenced by the fits (shown as straight lines). At the critical field the Hall resistivity drops to 0. This drop happens within a magnetic field range of about 1.9 T. Within this range, the resistivity depends linearly on the magnetic field with a slope much steeper than in the high-field region. Deviations from this behaviour are only observed in sharp spikes. These spikes can, however, potentially be explained by tiny offsets in magnetic field between the positive and negative field direction. This is supported by their presence in only some of the measurements. A clear fluctuation

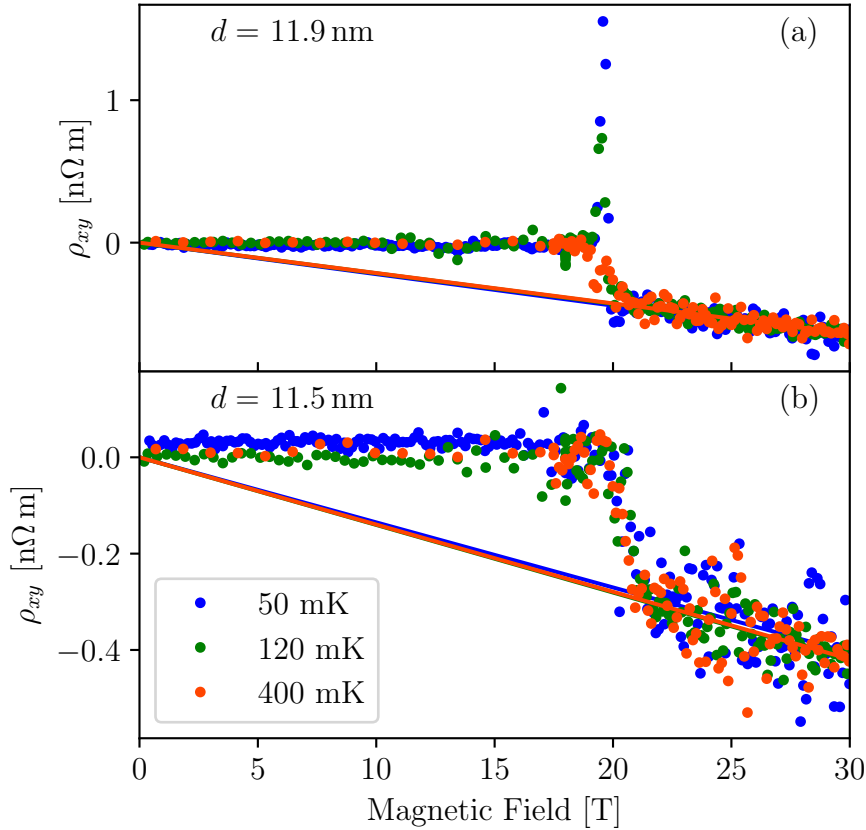


Fig. 5.5 The Hall resistivity for the thicker ($d = 11.9\text{ nm}$) film (a) and the thinner ($d = 11.5\text{ nm}$) film (b). The straight lines are fits to high-field normal state hall resistivity and are temperature independent.

contribution can thus not clearly be confirmed from the data at hand. The main reason seems to be the strong noise on the data, which in the region of interest is about 50% of the value itself. Even this level of noise is only achieved after averaging over many measured data points. Each point shown in figures 5.5 is the average over 45 measured points. In order to get a lower noise level, much higher statistics would thus be necessary. Such a measurement is hardly a viable option in a high-field magnet. From equation 5.6 an estimation of the expected fluctuation contribution can be obtained. Since the parameters entering the equation are measured far away from the quantum region, the result might deviate from the true experimental value. The first two factors in equation 5.6 yield a conductivity of $\Delta\sigma_{xy} \approx 0.15\text{ }\Omega^{-1}\text{ m}^{-1}$. The third factor depends on the distance of B to B_{c2} , but it can be assumed to be $1 < \ln(1/\ln(B/B_{c2})) < 10$, which corresponds to field values between 2 mT to 2 T above B_{c2} . Comparing this to the Hall conductivity

of the normal state close to the transition $\sigma_{xy}^n = 300 \Omega^{-1} \text{m}^{-1}$ clearly shows that the expected signal is below the noise level.

Considering the presence of the resistivity crossover at the critical point of the SIT, a similar scenario is expected for the transverse resistivity channel. Such a crossover as in ρ_{xx} could, however, not be observed in ρ_{xy} . Instead, the Hall resistivity is, within our measurement resolution, independent of temperature in the whole range of magnetic field. The Hall effect in the quantum region is thus at most influenced by contributions too small to observe in our measurement.

A further possible indication of the Hall effect in NbN can come from the Hall-insulator phase, as observed, for example, in highly disordered InO_x films [195]. In this phase, standard insulating behaviour in the longitudinal resistivity is found, i.e. a divergence of $\rho_{xx} \rightarrow \infty$ upon $T \rightarrow 0$. In the Hall resistivity, however, a finite value is observed which is found to be smaller than its classical value B/ne . The Hall conductivity, on the other hand, will again be $= 0$. A crossover point is observed for ρ_{xy} at higher fields than where the crossover is observed in ρ_{xx} . The critical field for ρ_{xy} is about a factor of 3 larger than the one for ρ_{xx} . Even though we do not observe the hallmarks of a Hall-insulating phase, this could indicate a hypothetical deviation of the observed linear Hall resistivity above the 30 T that our measurements could access. This connection is even more interesting when noticing that in InO_x the critical exponents evaluate to $z\nu = 2.4$, which is only different by a factor ≈ 2 to our results, and draws a connection to the quantum-Hall-to-insulator transition.

Another question arising from the comparison of the Hall isotherms and the resistivity isotherms is whether the curves go to 0 at the same fields. Phases with a finite ρ_{xx} and a vanishing ρ_{xy} have been observed in weakly disordered films of TaN_x and InO_x , hinting at a particle-hole symmetry extending into the metallic phase [196]. No variation in the field $B_{\rho_{xy}=0}$ can be seen in figure 5.5 for either film, while a clear shift is seen for $B_{\rho_{xx}=0}$ in figures 5.2 and 5.3. This raises the question whether we have such an anomalous metallic phase. A concluding answer to this can, however, not be given as the noise level in the Hall measurements are too large. Figure 5.6 shows this comparison, by normalizing ρ_{xx} to its high-field value and ρ_{xy} to $R_{\text{H}}B$ based on the high-field fit of the Hall resistivity.

5.4 Conclusions

In summary we showed the existence of critical behaviour with a crossover point in resistivity measurements of NbN thin films under high magnetic fields and the product of two critical exponents could be determined. This extends the validity of quantum critical scaling to higher fields than what is usually studied. In order

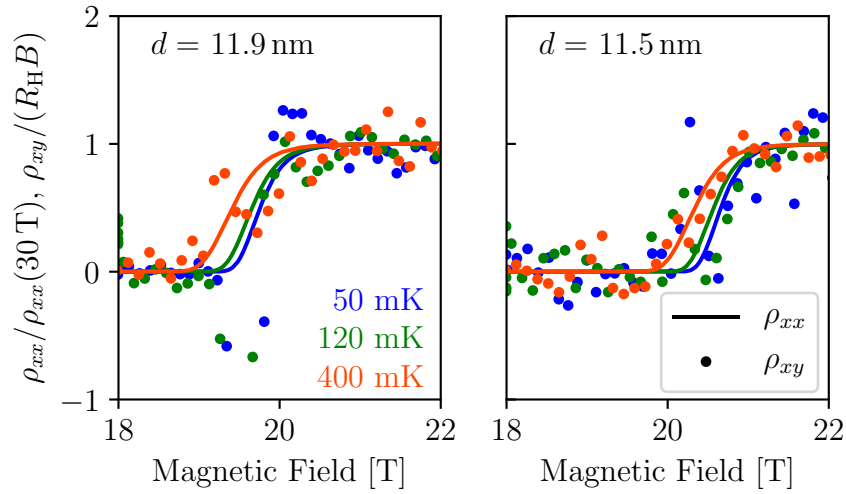


Fig. 5.6 Comparison of the superconducting transition of ρ_{xx} and ρ_{xy} for both films. The longitudinal resistivity is scaled with its value at 30 T and the Hall resistivity with $R_H B$, corresponding to the straight line fits shown in figure 5.5.

to get a clearer understanding of the value of $z\nu$, a study involving films of varying thicknesses would be necessary. No clear signal originating from superconducting fluctuations could be observed in the Hall resistivity. This is in parts due to large noise on the data and the possibility of having a very small fluctuation signal. Obtaining better measurements with less noise or more statistics is not a viable path to take.

Chapter 6

Observation of a Quantum Critical Point in $\text{Ca}_{1.8}\text{Sr}_{0.2}\text{RuO}_4$

6.1 Introduction

The ruthenate $\text{Ca}_{1.8}\text{Sr}_{0.2}\text{RuO}_4$ investigated in this chapter is a member of the $(\text{Ca}, \text{Sr})_2\text{RuO}_4$ substitution system, which in turn is a member of the Ruddlesden-Popper series ($\text{A}_{n+1}\text{B}_n\text{X}_{3n+1}$, see figure 6.1) [197, 198] of ruthenates. This series is of great scientific interest, especially for the Sr case. The different strontium-ruthenate members of the Ruddlesden-Popper series with different amounts of perovskite layers can be written as $\text{Sr}_{n+1}\text{Ru}_n\text{O}_{3n+1}$ for the n -layer compound. The unit cells of the most important structures are shown in figure 6.1. The case $n = 1$ corresponds to the single layer compound Sr_2RuO_4 . The case $n = 2$ corresponds to the bilayer compound $\text{Sr}_3\text{Ru}_2\text{O}_7$. In the limiting case of $n = \infty$ the pure perovskite compound SrRuO_3 is obtained. Since the $n = 0$ member SrO does not contain Ru anymore, it is usually not considered. Inside the perovskite layers the Sr atoms are located inside the gaps between the RuO_6 octahedra.

The substituted single layer compound $\text{Ca}_{2-x}\text{Sr}_x\text{RuO}_4$ has a very rich phase diagram, as shown in figure 6.2 as a function of substitution parameter x . Collectively many researchers have done a lot of work to establish this phase diagram [200–202]. The $x = 2$ end member Sr_2RuO_4 is a quasi-two-dimensional superconductor with a $T_c \approx 1$ K [203]. It is an oxide based superconductor isostructural to the $(\text{La}, \text{Ba})_2\text{CuO}_4$ superconductor, but does not contain any copper. It is thus a non-cuprate superconductor isostructural to a cuprate superconductor which makes it an interesting system, even though the electronic properties are different. Originally the superconducting pairing in Sr_2RuO_4 has been suggested to be of the p -wave kind [204] and experimental evidence in support has been found [205–207], but the discussion went on as no consensus could be reached [208–211]. Even

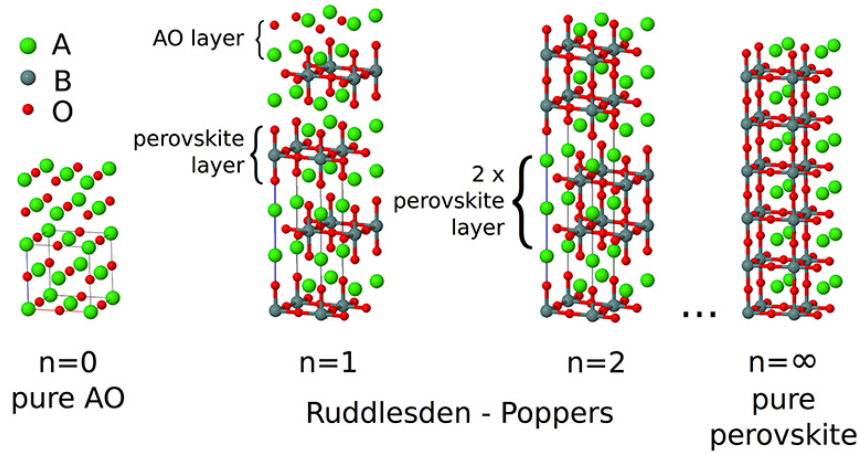


Fig. 6.1 The Ruddlesden-Popper series $A_{n+1}B_nO_{3n+1}$. Each unit cell contains n perovskite layers (ABO_3) between the AO spacer layers. In the $n = \infty$ compound no spacer layers are left and in the $n = 0$ compound no perovskite layers are left. Taken from Ref. [199].

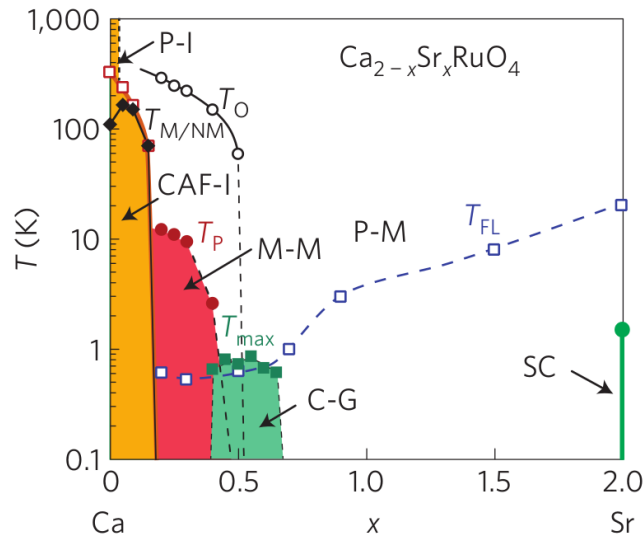


Fig. 6.2 Phase diagram of $\text{Ca}_{2-x}\text{Sr}_x\text{RuO}_4$. At small x the system is a paramagnetic insulator (P-I) and a commensurate antiferromagnetic insulator (CAF-I), followed by a magnetic metallic (M-M) state and a cluster glass (C-G) state. For $x = 2$ a superconductor is found. Outside of these states the system is a paramagnetic metal. Fermi liquid behaviour is observed below T_{FL} . A structural phase transition is denoted by T_O . In the present study the $x = 0.2$ compound was investigated. Taken from Ref. [200].

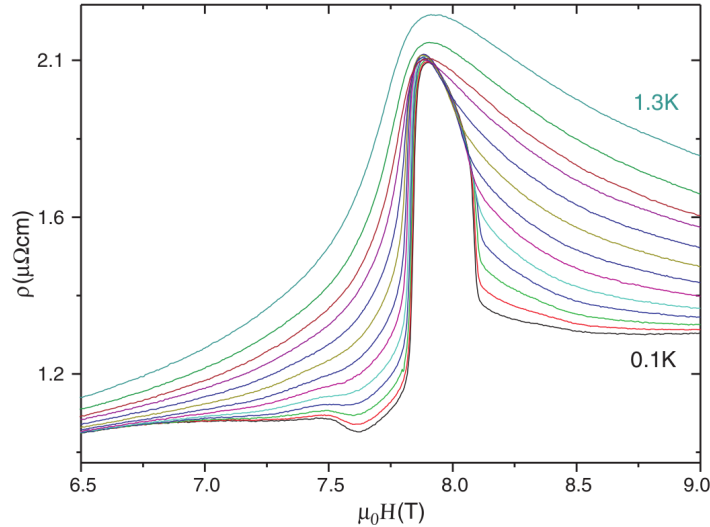


Fig. 6.3 The resistivity around the quantum critical points in $\text{Sr}_3\text{Ru}_2\text{O}_7$. For temperatures low enough ($T < 1$ K) and for a small temperature dependent range in magnetic field the resistivity is temperature independent and varies rapidly with a changing magnetic field. Taken from Ref. [216].

f -wave superconductivity has been suggested [212]. More recently a consensus developed that it is not p -wave superconductivity after new NMR measurements showed that older reports are incorrect [213]. An other way forward that has been suggested is to use strain to further investigate the superconductivity in Sr_2RuO_4 and the proposed spin density wave phase [214]. The $x = 0$ end member Ca_2RuO_4 on the other hand is a Mott insulator. This state originates from multi-band physics, Coulomb interaction, and Hund's coupling [215]. At $x = 0.2$ a metal/non-metal transition takes place and at $x = 0.5$ a strong increase in the susceptibility is found, driving the system close to ferromagnetism [201].

A lot of research has been undertaken on the bilayer compound $\text{Sr}_3\text{Ru}_2\text{O}_7$. The conduction is quasi-two-dimensional and is located inside the perovskite bilayers [217]. The magnetic properties are paramagnetic [217] but very close to ferromagnetism and can be turned ferromagnetic under weak uniaxial pressure [218]. The proximity to ferromagnetism leads to the development of enhanced magnetism termed metamagnetism. The symmetry is lowered from tetragonal to orthorhombic due to a 7° rotation of the oxygen octahedra. Furthermore the fourfold rotational in-plane symmetry of the crystal lattice is broken very weakly, on the order of 10^{-7} [219] relative to the lattice parameter. But most importantly interesting physical properties appear below 1 K and under a magnetic field in crystals of extremely high purity [216, 220]. Resistivity measurements in this region are shown in figure 6.3. At 7.8 T the resistivity suddenly increases almost by a factor of two

in a very sharp transition. On the other side of the peak the resistivity decreases slower initially but is followed by an other steep decrease in resistivity at 8.1 T. Afterwards the resistivity is close to constant but at a higher level than before the transitions. This behaviour can be seen at low temperature in a small window of magnetic field which is temperature dependent. The higher the temperature, the smaller the window in which this behaviour is observed. Between the two steep flanks, the resistivity is temperature independent. At around 1 K the strong effects disappear and only a broader peak is left with much wider flanks than what is seen for lower temperatures. Closely related to the main peak is a small dip of the resistivity starting at 7.5 T, which is only present at the very lowest temperatures and in the purest of samples. The steep low-temperature resistivity increase are accompanied by peaks in the AC susceptibility and linear magnetostriction and are not a purely resistive feature. This small phase between 7.8 T and 8.1 T is considered to be an electronic nematic phase [221], a phase with broken rotational symmetry and the electronic equivalent to a nematic liquid crystal as used in computer displays. This phase is limited on both sides by metamagnetic transitions. The transition on the lower field side is connected to large increases in entropy [222]. The electronic nematic phase shifts towards lower magnetic fields when the applied magnetic field is tilted away slightly from the crystallographic c -axis [219]. Both below and above the nematic phase quantum oscillations have been observed [223]. The frequency shift corresponds to a small change in the Fermi surface area and is accompanied by a small shift in magnetic moment. The transport anisotropy in $\text{Sr}_3\text{Ru}_2\text{O}_7$ is strongly dependent on uniaxial pressure [224]. Upon compression the resistivity inside the phase is increased. This increase is already significant for only small strains. In addition the upper field range of the phase increases. On the other hand, an elongated sample will lose the resistivity increase completely at a strain of only 0.05%.

The nematic phase transitions end at a quantum critical point at $T = 0$. Clear indications of quantum criticality have been observed [225, 226]. Because the two QCPs are so close together, they can often not clearly be distinguished in measurements further away and appear as just one QCP. When fitting the resistivity to a function of the form $\rho = \rho_0 + AT^\alpha$, the influence of at least one quantum critical point can be seen in all three parameters ρ_0 , A , and α , as shown in figure 6.4. For low fields the exponent α is consistent with the Fermi liquid value of 2. Upon approach of the quantum critical point, its value decreases gradually and reaches 1 at the quantum critical point. For higher fields the value increases again, reaching 1.5 at the highest field investigated of 14 T. At high temperatures the exponent has a value of 1 for the whole range of magnetic field, but since the

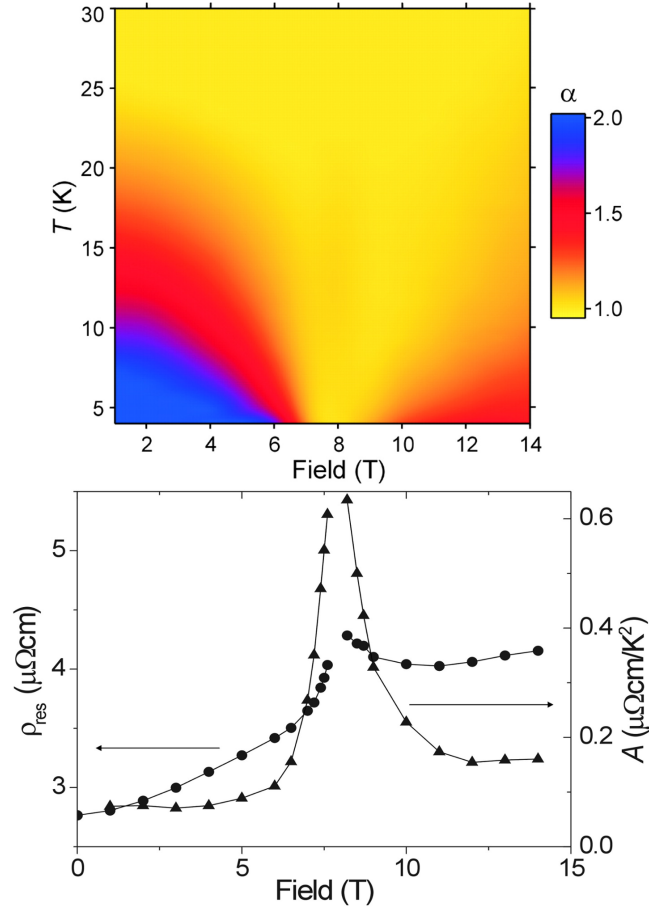


Fig. 6.4 (Top) Exponent α of $\text{Sr}_3\text{Ru}_2\text{O}_7$ in $\rho = \rho_0 + AT^\alpha$ displaying the fan-like structure of a QCP. At the QCP the exponent is at its minimum. Far away from the QCP, the Fermi liquid behaviour of $\alpha = 2$ is recovered. (Bottom) Parameters ρ_0 and A , both showing a peak at the QCP. Both panels taken from Ref. [225].

Fermi liquid picture is only applicable for low temperatures, this deviation is not unexpected.

Spin density wave order has been observed inside the nematic phase with neutron scattering. At the same time these measurements show that there are two separate phases [227]. These two phases are distinguished by different wave vectors of the spin density wave and an anisotropy in the resistivity behaviour upon tilting of the magnetic field. The corresponding phase diagram is shown in figure 6.5. The two phases lie in between two regions of high and low magnetic moment. For perfect alignment of the magnetic field along the c -axis the observations correspond to two SDW directions, along the crystallographic a - and b -axes, forming two domains in the sample. For small misalignments of the field, only the CDW

support the importance of this van Hove singularity [232–234]. More recently, the van Hove singularity has been linked more directly to the itinerant metamagnetism at low temperatures [235].

Lastly, to reiterate: The clear observation of the nematic phase in $\text{Sr}_3\text{Ru}_2\text{O}_7$ is strongly dependent on the purity of the samples. Only in the purest samples the resistivity follows the sharp lines. In less clean samples, it merely shows a broadened peak [223].

The electronic nematic state with its broken rotational electronic symmetry is of great importance to understand the behaviour in $\text{Sr}_3\text{Ru}_2\text{O}_7$. Other studies, such as in $\text{FeSe}_{1-x}\text{S}_x$ of nematic quantum critical points show how at such a point itinerant fermions couple to fluctuations of the order parameter. [236]. Interestingly, in this material a spin-density-wave is found in FeSe under pressure [237], but a connection of the QCP to this SDW-phase is not probable [236].

In this study we present strong evidence for the existence of a quantum critical point in $\text{Ca}_{1.8}\text{Sr}_{0.2}\text{RuO}_4$ and lay out its similarities to the quantum critical point found in $\text{Sr}_3\text{Ru}_2\text{O}_7$. We furthermore compare our results to quantum criticality observed in Sr_2RuO_4 and other materials.

6.2 Methods

The single crystals of $\text{Ca}_{1.8}\text{Sr}_{0.2}\text{RuO}_4$ were obtained through a collaboration with Antonio Vecchione, Rosalba Fittipaldi, and Veronica Granata from the University of Salerno. The resistivity measurements were conducted in a commercial PPMS manufactured by the company Quantum Design. Measurements have been taken on multiple samples. Some measurements were conducted in a ^3He system for the PPMS. Measurements in a dilution refrigerator were performed at PSI in the TASP instrument during a beam shutdown. For this measurement, the resistance was measured with a Lakeshore resistance bridge. The samples were connected in a four-point measurement geometry. Silver wires were glued to the sample with different glues: DuPont 6838 silver paste and EPO-TEK H20E two component epoxy. No noticeable differences were found in measurements between the two methods but the contacts made with the silver paste were more mechanically stable. All measurements reported are with the magnetic field aligned along the c -axis while the current is flowing in the ab -plane.

6.3 Results and Discussion

Resistivity measurements on $\text{Ca}_{1.8}\text{Sr}_{0.2}\text{RuO}_4$ are shown in figure 6.6, in panel (a) as a function of magnetic field and in panel (b) as a function of temperature.

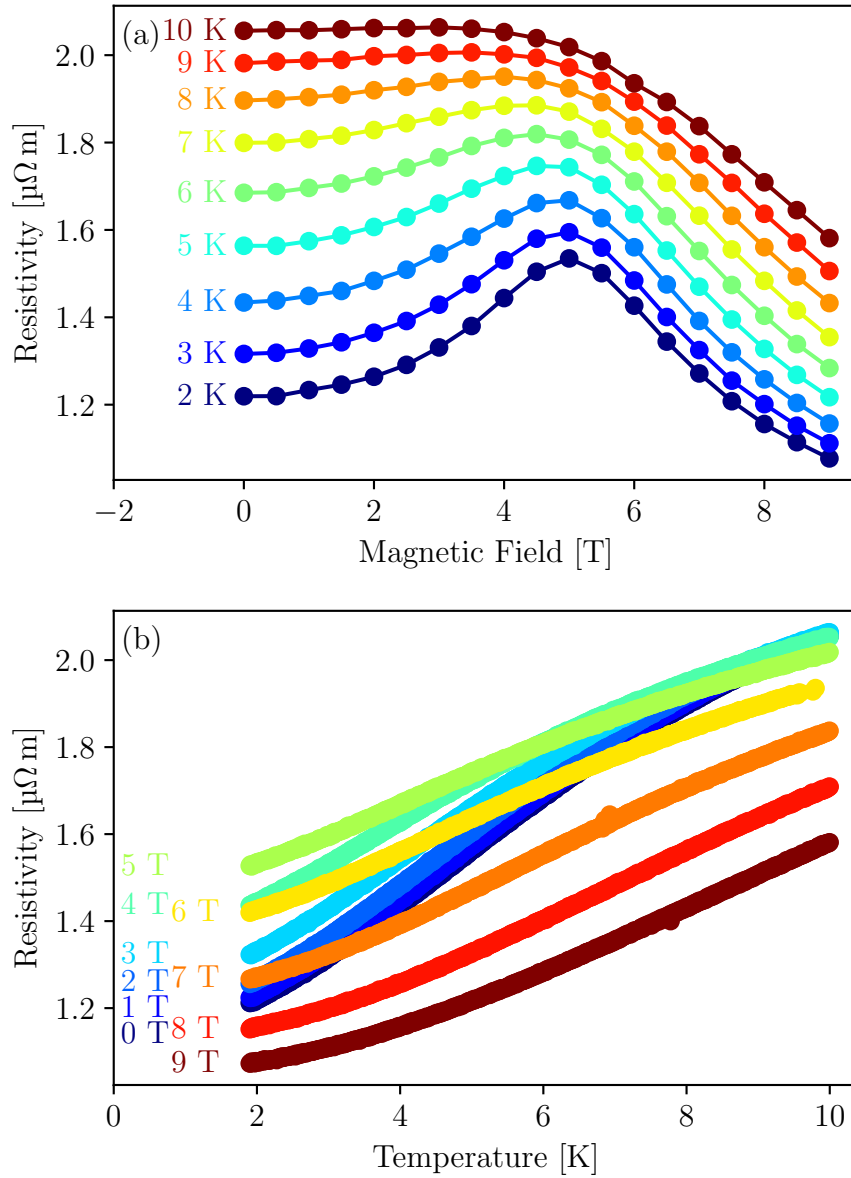


Fig. 6.6 (a) Resistivity as a function of magnetic field measured between 2 K and 10 K in steps of 1 K. At low temperatures a strong peak is present at B_c , which gradually disappears for increasing temperature. At 10 K all traces of a peak have vanished. (b) Temperature scans for different fields as indicated.

The resistivity behaves metallic in the entire range of magnetic fields, for each field value the resistivity is a strictly monotonic function of the temperature. The resistivity of $1.2\ \mu\Omega\text{m}$ for zero temperature and field is considerably larger than what is observed in $\text{Sr}_3\text{Ru}_2\text{O}_7$, consistent with the charge transport taking place in the perovskite layers and the addition of Ca which brings the system closer to the insulating state. The residual resistivity ratio is $\rho(300\text{ K})/\rho_0 \approx 7$. Upon cooling below 10 K a peak starts to appear in field-scans at 5 T, getting sharper the lower the temperature becomes. The resistivity curves of $\text{Ca}_{1.8}\text{Sr}_{0.2}\text{RuO}_4$ show a behaviour reminiscent of those on $\text{Sr}_3\text{Ru}_2\text{O}_7$ (see figure 6.3) above 1 K.

The temperature independent resistivity feature in $\text{Sr}_3\text{Ru}_2\text{O}_7$ only starts to appear at around 1 K. This poses the question if at lower temperatures the resistivity would also show the same feature in $\text{Ca}_{1.8}\text{Sr}_{0.2}\text{RuO}_4$. For this purpose measurements with a dilution refrigerator were performed down to 100 mK. Within the noise (which is very large) the result is consistent with the data recorded at 2 K meaning that no further narrowing of the peak occurred in the accessible temperature range. A strong narrowing of the resistivity peak like in $\text{Sr}_3\text{Ru}_2\text{O}_7$ can thus not be confirmed, but neither clearly ruled out based on the measurements in the dilution refrigerator and a potential narrowing at even lower temperatures is possible.

In order to better visualize the resistivity behaviour upon changes of field and temperature, a colorplot of the resistivity as a function of both magnetic field and temperature is shown in figure 6.7(a). The quantum critical point at 5 T is clearly visible in the color map through the fan-shaped resistivity behaviour in the region around it. The resistivity curves at fixed field follow locally the shape given by the equation

$$\rho(T) = \rho_0 + AT^\alpha \quad (6.1)$$

which can be used to fit the data in different temperature windows. All three parameters are free parameters of the fit. In case some of the parameters are fixed, different results will be obtained. The exponent α is shown in figure 6.7(b) as a color plot. The quantum critical point is visible again at 5 T and its influence in the (B, T) plane is comparable to that of the resistivity itself. The temperature window over which the fitting is performed had to be taken large enough to get the fitting procedure to converge and the noise level of the resulting exponent is noticeably larger than the noise level in the resistivity. The result, however, is believable and represents well the properties of a QCP. Figure 6.7 can be considered to be the most important result of this chapter.

Earlier results published on $\text{Ca}_{1.8}\text{Sr}_{0.2}\text{RuO}_4$ do not observe such a quantum critical behaviour [238]. Resistivity peaks could be observed in ρ_{xx} and ρ_{xy} , but

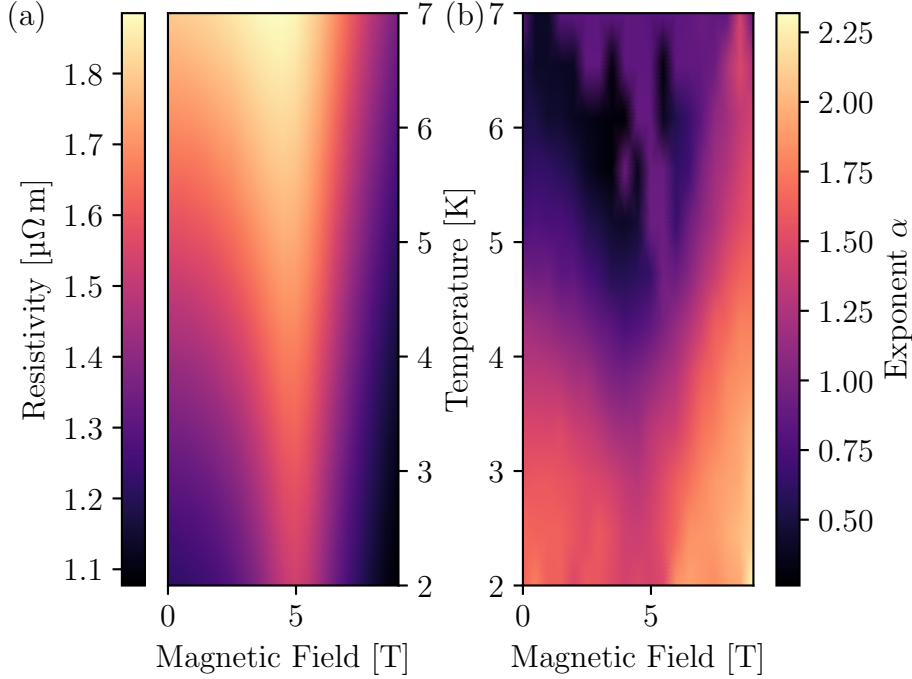


Fig. 6.7 (a) Resistivity as function of magnetic field and temperature. (b) The exponent α of $\text{Ca}_{1.8}\text{Sr}_{0.2}\text{RuO}_4$ in $\rho = \rho_0 + AT^\alpha$. At the QCP the exponent is at its minimum. Far away from the QCP, the Fermi liquid behaviour of $\alpha = 2$ is recovered. The fan-like structure of a QCP is visible in both panels.

neither the prefactor A nor the exponent α display anything resembling the behaviour expected for a quantum critical point.

Exponents of $4/3$ are expected to occur near antiferromagnetic and magnetic instabilities and have been observed before for $\text{Ca}_{1.8}\text{Sr}_{0.2}\text{RuO}_4$ in zero magnetic field at low temperature [201] and in Sr_2RuO_4 under pressure [239]. For even lower temperatures in zero field the observation of scaling consistent with T^2 is claimed again in $\text{Ca}_{1.8}\text{Sr}_{0.2}\text{RuO}_4$ [240]. In figure 6.8 the temperature scaling of our resistivity curves at low temperatures is shown for three select magnetic fields: below, at, and above the QCP. Panel (a) has a temperature scaling of T^2 for the abscissa, corresponding to the Fermi liquid model. At high magnetic fields, the resistivity is a straight line for T^2 scaling, thus indicating Fermi liquid behaviour. The same is observed for zero field at low temperatures. Panel (b) is based on a $T^{1.3}$ scaling, leading to a straight line for 5 T, showing the suppression of Fermi liquid behaviour due to the quantum critical point.

Lastly the behaviour of the factors A and ρ_0 at 2 K are shown in figure 6.9. The fit is done to the equation $\rho = AT^2 + \rho_0$ for $T < 2.4$ K. It is necessary to keep the exponent constant as the units of A depend on the temperature exponent. Both

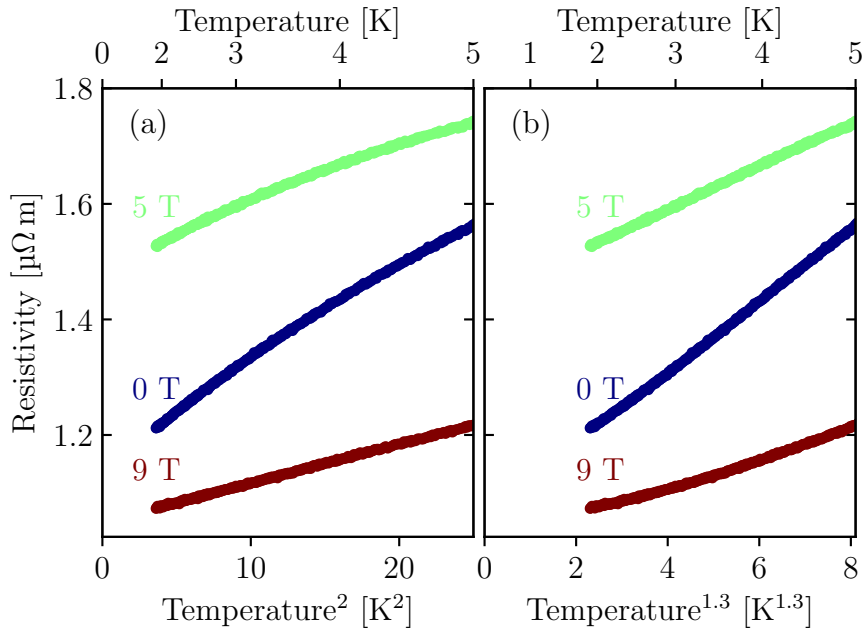


Fig. 6.8 Temperature scaling of the resistivity for magnetic fields as indicated. (a) Scaled as T^2 . A straight line is obtained for 9 T. (b) Scaled as $T^{1.3}$. A straight line is obtained for 5 T. For 0 T the exponent of 2 is only recovered for the lower temperatures. This indicates the change from a Fermi liquid to a non-Fermi liquid to again a Fermi liquid.

quantities display a peak at or around the QCP. In the case of A it is much less symmetric than ρ_0 or the resistivity as seen in figure 6.7. Nonetheless these peaks give further support to the presence of a QCP.

In order to get a better understanding of why earlier measurements did not observe quantum critical behaviour, it is illustrative to look at measurements from different crystals. Large variations between crystals would indicate strong dependence of the quantum critical behaviour on the microscopic details and could explain the absence of quantum criticality in older measurements. The measurements of two more of our crystals are shown in figure 6.10. These data were recorded down to 0.5 K in a ^3He system. The sample shown in the left panel is noticeably more asymmetric, but the overall resistivity behaviour is still consistent with a quantum critical point. The much higher resistivity of the data on the left indicate a sample of lower quality and possibly explains the skewed colorplot. The data on the right agree very well with the sample of figure 6.7. The parameters A and ρ_0 are shown in figure 6.11, as obtained from fits to the equation $\rho = AT^2 + \rho_0$. For both crystals there are clear features present at or around the critical field. The strong divergence as seen in $\text{Sr}_3\text{Ru}_2\text{O}_7$ could again not be observed. The behaviour

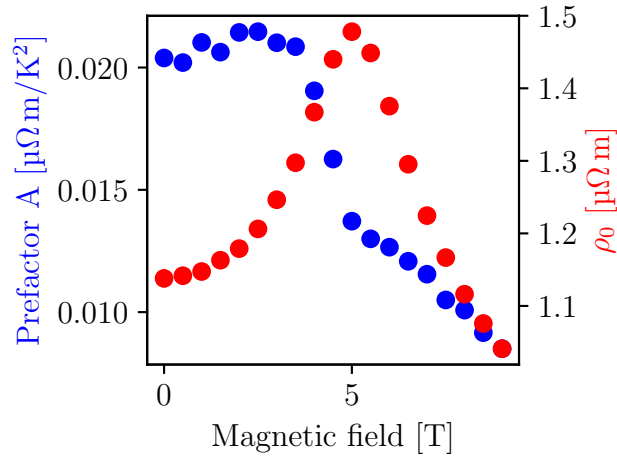


Fig. 6.9 Parameters A and ρ_0 of $\rho = AT^2 + \rho_0$ as obtained from the measurement shown in figure 6.7. The fitting window was $T < 2.4$ K. Both quantities show features at or around the QCP.

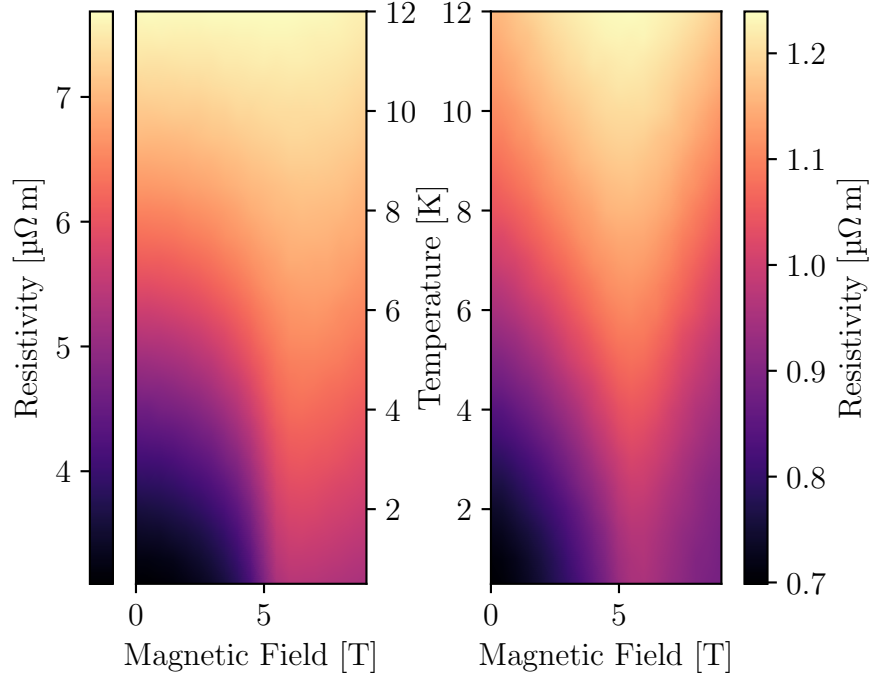


Fig. 6.10 Comparison of two other crystals, both measured with ^3He down to 500 mK, highlighting the variations in resistivity behaviour between different crystals.

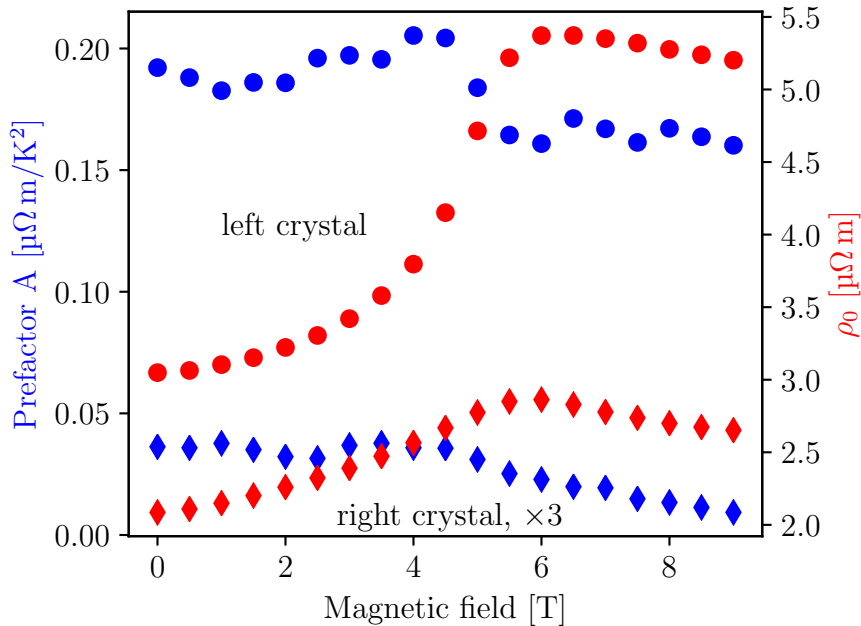


Fig. 6.11 Parameters A and ρ_0 in $\rho = AT^2 + \rho_0$ as obtained from the two measurements shown in figure 6.10 by fitting the data below 1.2 K. The labels of ‘left’ and ‘right’ refer to the measurements of figure 6.10. The data of the ‘right’ crystal has been multiplied by 3 for clarity.

overall is in reasonable qualitative agreement with what is shown in figure 6.9. The asymmetry of ρ_0 is reversed but the prefactor A is skewed in the same direction. In order to plot the exponent α of these two crystals the data are not of sufficient quality for reliable fitting but the limited conclusions that can be drawn agree with the results of the first crystal. We thus do observe the same qualitative behaviour in multiple crystals, removing the possibility of having a special or unique crystal out of pure luck. The different crystals presented here are from the same crystal growers, so variations in crystal growth processes between different groups could be an explanation. The resistivity alone, however, does not indicate an improved purity. Neither does the residual resistivity ratio.

Since many measurements on $\text{Ca}_{1.8}\text{Sr}_{0.2}\text{RuO}_4$ and related materials have already been published, it is important to compare our findings with these older reports. The same qualitative behaviour as we see in the resistivity is also found in heat capacity measurements, which show a pronounced increase centered around 5.3 T [241]. This is shown in figure 6.12. Such a field dependence is visible below 3 K for all fields up to B_c . For higher fields variations in heat capacity with field can be observed at least up to 11 K. The coefficient A as shown before contains

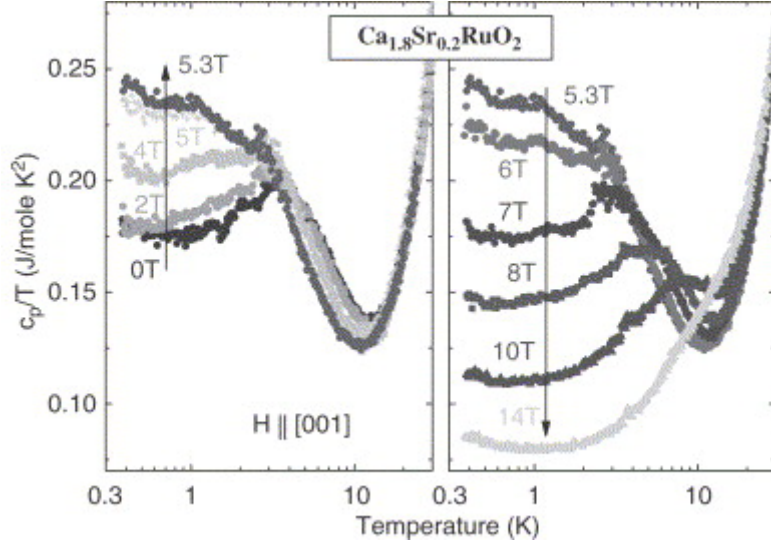


Fig. 6.12 The heat capacity c_p/T of $\text{Ca}_{1.8}\text{Sr}_{0.2}\text{RuO}_4$. The maximum is reached at the quantum critical point, reflecting the behaviour of $R(T)$ curves. Taken from Ref. [241].

information about the quasiparticle mass m^* and is linked to the electronic specific heat through the Kadowaki-Woods ratio [242]. An increase in A then indicates an increasing electronic specific heat and an increasing effective mass. The specific heat data shown in figure 6.12 confirm this scenario. The same study also reports a steep increase in magnetostriction very close to the critical field. These results are linked to magnetic fluctuations at a metamagnetic transition, hence yielding a further similarity to the behaviour of $\text{Sr}_3\text{Ru}_2\text{O}_7$.

The field-dependent magnetization of $\text{Ca}_{1.8}\text{Sr}_{0.2}\text{RuO}_4$ shows a steep increase starting at 5 T lasting until around 9 T [240]. Similarly, resistivity measurements with $B \parallel I \parallel c$ show a similar peak as we observe with $I \perp c$, albeit with a much flatter decrease in resistivity for fields above the peak. Both features are ascribed to a metamagnetic transition due to a destabilized antiferromagnetic order. Resistivity measurements with our configuration of magnetic field and current are not reported in this publication.

More insight might be gained from strained thin films of Sr_2RuO_4 . No external pressure is needed if such films are grown on lattice-mismatched substrates, which enables ARPES studies to investigate the Fermi surface. Such a study found a topological Lifshitz transition in the Fermi surface upon application of strain, as a van Hove singularity is pushed below the FS [243]. A Lifshitz transition is the change of how the FS connects or its disappearance [244]. This transition in Sr_2RuO_4 is accompanied by signatures of a quantum critical point visible in the resistivity behaviour. At the Lifshitz transition a temperature dependence of

$\rho \propto T^{1.4 \pm 0.1}$ is observed, consistent with our values obtained for $\text{Ca}_{1.8}\text{Sr}_{0.2}\text{RuO}_4$. Furthermore, in Sr_2RuO_4 a deviation from the Fermi liquid behaviour in the real part of the self energy function $\Sigma'(\omega)$ accompanies the Lifshitz transition as well.

Similar behaviour has been observed in another study on bulk samples of Sr_2RuO_4 under uniaxial pressure [239], where the temperature dependence of $\rho \propto T^{1.5}$ is obtained at the Lifshitz transition and $\rho \propto T^2$ away from it. The coefficient A as a function of strain also shows indications of a divergence at the critical strain.

The strong similarities between $\text{Ca}_{1.8}\text{Sr}_{0.2}\text{RuO}_4$ and $\text{Sr}_3\text{Ru}_2\text{O}_7$ now raise the question of whether there is a spin density wave present at extremely low temperatures. Since even in the ^3He measurements no clear phase transition is occurring at finite temperature it is possible that this QCP originates from an ordered phase at $T = 0$ only or that the sample is not clean enough to enter a SDW state. The problem lies in the inherent disorder in a doped system [245]. With increased disorder $\text{Ca}_{1.8}\text{Sr}_{0.2}\text{RuO}_4$ has even been driven to insulating behaviour [246]. Since the ruthenates are generally very sensitive to disorder, this adds further complications. Furthermore, if the disorder is not homogeneously distributed over the sample, the QCP could appear for varying magnetic fields for different regions of the sample, smearing out a sharper quantum critical behaviour. Strong electron correlation make it generally harder to understand this system.

Another big problem in this study is the twinning of $\text{Ca}_{1.8}\text{Sr}_{0.2}\text{RuO}_4$ crystals originating from the tilting and rotations of the RuO octahedra [202]. The orthorhombic lattice can be rotated by 90° between different regions of the crystal. This means that all effects seen in the measurements are smeared out averages over the two lattice directions. The importance of the different twins is also illustrated by magnetization measurements along different axes showing strongly different behaviour [201]. In order to circumvent this problem, a detwinning process must be undertaken.

Overall the picture that emerges from all these considerations is that there is a QCP due to a metamagnetic transition around 5 T in $\text{Ca}_{1.8}\text{Sr}_{0.2}\text{RuO}_4$. Maybe in cleaner samples, multiple metamagnetic transitions in a small magnetic field range around 5 T would emerge, possibly even in conjunction with a SDW phase. Whether it is even possible to make such clean samples is a question that can not be answered here. Nonetheless, the metamagnetic transition is not the only possible explanation. A further possible origin of the QCP is the metal/nonmetal transition upon crossing the $x = 0.2$ doping that could occur upon increasing the magnetic field. The observation of metallic resistivity in all samples to either side of the QCP does, however, not support such considerations. A further possibility is that the real QCP is at another doping and we look at a cut through a multidimensional

quantum critical region slightly away from the QCP. Finally the possible influences of a van Hove singularity can also not be neglected.

With ARPES measurements it has been shown that the non-Fermi liquid behaviour originates predominantly from the d_{xy} bands while the d_{xz} and d_{yz} orbitals still display Fermi liquid behaviour. The breakdown of Fermi liquid quasiparticles is thus orbitally selective [247]. A combination of Fermi liquid and non-Fermi liquid quasiparticles will make the experimental treatment a lot harder as the different contributions will have to be disentangled.

6.4 Conclusions

In this chapter we have shown the observation of strong evidence of a quantum critical point in $\text{Ca}_{1.8}\text{Sr}_{0.2}\text{RuO}_4$. Many of our results are in agreement with older published data [240]. Especially on resistivity measurements we observe a distinct difference to older publications, which find no evidence of a QCP [238, 241]. Our data shows strong resemblance to a quantum critical point of an electronic nematic phase in $\text{Sr}_3\text{Ru}_2\text{O}_7$. The exponent α , the residual resistivity ρ_0 and the prefactor A of the temperature dependence of the resistivity all show clear signs of quantum critical behaviour. The same effects are observed on three different samples with small quantitative differences most likely resulting from varying quality of crystals. The origin of the QCP is most likely one or more closely spaced metamagnetic transition. This raises the question of whether there is another phase hiding in $\text{Ca}_{1.8}\text{Sr}_{0.2}\text{RuO}_4$ at lower temperatures than what has been accessible to us, especially a SDW phase. Measurements at lower temperatures and detwinned crystals would both be necessary to obtain a more detailed insight. A publication based on the results of this chapter is in preparations by Yang Xu, Daniel Destraz, et al.

Chapter 7

Magnetism and Topological Effects in PrAlGe

7.1 Introduction

Topological Weyl semimetals are influenced strongly by the Berry curvature originating from their Weyl nodes. Typical properties include negative magnetoresistance and anomalous Hall and Nernst effects. Many Weyl semimetals with very large anomalous Hall effects have been reported. Examples include the antiferromagnetic Mn_3Sn bulk [248,249] and thin films [250,251], the kagome ferromagnet $\text{Co}_3\text{Sn}_2\text{S}_2$ [252], and the nodal line ferromagnet Fe_3GeTe_2 [253]. In the same fashion extremely large Nernst effects have been observed in the Heusler compound Co_2MnGa [254,255]. This material is in proximity of a Lifshitz transition between type I and type II magnetic Weyl fermions. The chiral anomaly in form of negative magnetoresistance could also be observed. Similarly large Nernst effects have been reported in Mn_3Sn [256] and $\text{Co}_3\text{Sn}_2\text{S}_2$ [257]. In NbP, another inversion-symmetry-breaking Weyl semimetal the Dirac dispersions lead to a Nernst effect that is orders of magnitude larger than its Seebeck effect [258]. Another topological effect observable in the Hall channel besides the anomalous Hall effect is the planar Hall effect, which is linked to the chiral anomaly. It has been observed, for example, in the half Heusler Weyl semimetal GdPtBi [259]. Many properties of topological materials are of interest for applications and can be expected to have a great impact on everyday life in the future [260]. The large Nernst responses, for example, could be of great use for transverse thermoelectric elements.

Recently the $R\text{AlGe}$ ($R = \text{La}, \text{Ce}, \text{Pr}$) family has been investigated in a theoretical study and presented as a model system for the interactions of magnetism in non-centrosymmetric crystals [263,264], see figure 7.1(a). The three compounds have different types of Weyl nodes at the Fermi level and are either magnetic or

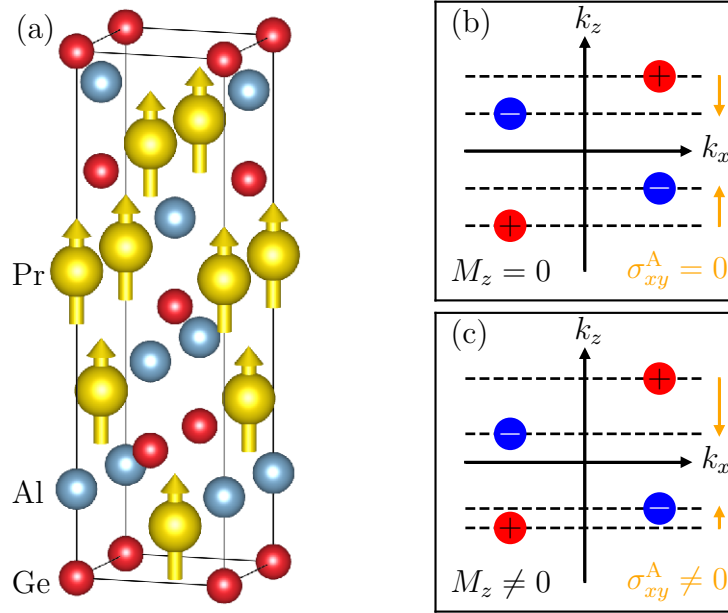


Fig. 7.1 (a) The unit cell of PrAlGe, containing four formula units. It is of the tetragonal lattice system and has the space group $I4_1md$ [261]. The arrows indicate the magnetic moments on the Pr atoms, aligned along the c -axis, which constitutes the easy axis for this system. The crystal structure importantly lacks inversion symmetry, giving rise to topological effects. The figure was made using the VESTA software [262]. (b,c) Effect of the Weyl node position on the anomalous Hall conductivity σ_{xy}^A . For no magnetization (b) the Weyl nodes are separated equally and the Hall conductivity cancels. The presence of a magnetization (c) shifts the Weyl cones according to their chirality (+ or -). The different separations lead to a nonvanishing Hall conductivity.

non-magnetic depending on the rare earth ion. Table 7.1 lists these properties for the three compounds. The only combination not present is a non-magnetic material with type I Weyl nodes at the Fermi level. In inversion symmetric compounds a Weyl semimetal can be generated from breaking the time-reversal symmetry through magnetism. The Dirac cone then turns into a pair of Weyl cones. In the case of materials with a broken inversion symmetry, at least two pairs of Weyl cones are already present. The magnetism is then shifting the Weyl nodes with the direction depending on their chirality. This process is visualized in figure 7.1(b,c). The separation of the Weyl nodes induces an anomalous Hall conductivity but since at $B = 0$ the two pairs of Weyl nodes induce an equally strong anomalous Hall effect in opposite directions the two components cancel and no anomalous Hall effect can be observed in measurements. A magnetization in the material will shift the Weyl nodes such that the separation of the two pairs becomes different,

Compound	Type of Weyl node at FL	Magnetism
LaAlGe	type II	non-magnetic
CeAlGe	type II	magnetic
PrAlGe	type I	magnetic

Tab. 7.1 Type of Weyl node at the Fermi level (FL) and magnetic properties of the three $R\text{AlGe}$ compounds.

leading to a finite Berry curvature when integrated over the Brillouin zone over all bands below the Fermi energy. This then means that the two opposite components of the Hall conductivity do not cancel completely any more and an anomalous Hall effect is observed experimentally. The same reasoning applies to the anomalous Nernst effect.

Early studies of PrAlGe and related alumogermanides date back to the end of last century [261, 265, 266]. Solid PrAlGe crystallizes in a tetragonal lattice with the $I4_1md$ space group [261]. A unit cell of PrAlGe is shown in figure 7.1(a). One unit cell contains four formula units. The arrows in the figure indicate the magnetic moment of the Pr atoms, which align along the easy-axis of the system which coincides with the crystallographic c -axis. Each plane perpendicular to the c -axis contains only one kind of atom. Along the c -axis the atoms are aligned alternately. This leads to a screw structure alignment along c for each of the three kinds of atoms. The most important property of this crystal for the present study is the lack of an inversion center, which breaks spatial inversion symmetry. This broken spatial inversion symmetry leads to topological effects.

Recently the sister compound CeAlGe, proposed to be a type II Weyl semimetal, has been investigated [267]. The authors find anisotropic magnetic properties. The ground state has been confirmed to be antiferromagnetic below 5 K. No anomalous transport properties have been observed.

In this study we investigate the compound PrAlGe through electric and thermoelectric transport, bulk magnetization, and SANS. We show how the ferromagnetic ground state hides the anomalous transport properties through domain formation and how they can be recovered by polarizing the sample. Comparisons to first principle calculations prove the origin of the anomalous transport based on the topology. A schematic phase diagram is shown in figure 7.2 for illustrative purposes to make the result section more clear. For high temperatures PrAlGe is a paramagnet. At T_c a ferromagnetic phase based on a domain structure is entered. At a magnetic field B_s the magnetism in the sample saturates and the domain structure disappears, leaving a fully field polarized sample. Inside the Ferromagnetic phase, a glass transition is found starting at a temperature T_g .

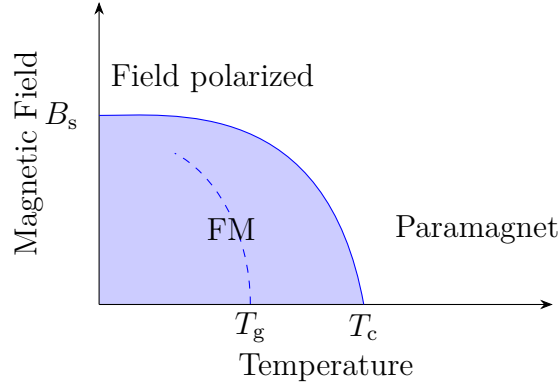


Fig. 7.2 Schematic phase diagram of PrAlGe. An inhomogeneous ferromagnetic (FM) state appears below the critical temperature T_c and the saturation field B_s . Outside of this state, paramagnetic behaviour is found. Above B_s the material is field polarized for low temperatures. A glass transition is found at T_g (dashed line).

7.2 Methods

Single crystals of PrAlGe in high quality were grown by Pascal Pupal at PSI using the flux growth method and the floating zone method. Their growth process and a comparison of the properties of crystals of the two types is described in Ref [268]. The flux grown samples contain a slight excess of Al and are typically smaller than the floating zone crystals. For the study presented in this chapter crystals of both types have been used. The variations between crystals of the two types and between different crystals of the same type are not of importance for any of the conclusions of this chapter.

The electrical transport (ρ_{xx} and ρ_{xy}) was measured in a Quantum Design Physical Property Measurement System (PPMS). The DC magnetic moment was measured in a Magnetic Property Measurement System (MPMS) of the same company. The AC magnetic moment measurements were performed with the commercial AC Measurement System (ACMS) for the PPMS. For the thermoelectric measurements a home-build insert for the PPMS was used. The PPMS was reading out the sample thermometers, while Keithley nanovoltmeter were used to measure the longitudinal and transverse voltages after amplifying the signal by a factor of 1000. For the Hall measurements a Hall bar geometry was used for the contacts and good electrical contact was achieved with DuPont 6838 silver paste cured at 500 °C for 10 min and subsequent application of short high voltage pulses, finally reaching values of a few Ohm. The temperature gradient in the Nernst measurements was kept at around 3% of the average sample temperature. All temperatures were measured with Cernox thermometers.

The powder neutron diffraction was performed at PSI with the DMC instrument. The neutron wavelength was 2.457 Å. The powder sample from which the diffraction profiles were collected were of mass 2 g. The base sample temperature in the Orange cryostat was 1.6 K.

The SANS measurements were performed at PSI at the SANS-I instrument with a base temperature of 1.9 K. The 25 mg single crystal was mounted with the *c*-axis parallel to the incoming beam with the magnetic field aligned in the same direction. The neutron wavelength was set to $\lambda_n = 8 \text{ \AA}$ with $\Delta\lambda_n/\lambda_n = 10\%$. For each temperature or magnetic field value the data were collected for 5 to 20 min.

All measurements reported here were conducted with the magnetic field aligned along the *c*-axis. For all transport measurements, the electric or heat current were applied within the *ab*-plane.

7.3 Results on Transport and Magnetism

The first results we present are on electrical transport (resistivity including magnetoresistance, and Hall effect) and thermoelectric (Seebeck and Nernst) measurements as well as magnetization data. All these measurements focus mainly on the macroscopic behaviour. Later sections present theoretical calculations and results on neutron scattering, which link the observed macroscopic behaviour to the microscopic details.

7.3.1 Resistivity, Hall, DC Magnetization, Seebeck, and Nernst

Figure 7.3 shows the three quantities ρ_{xx} , ρ_{xy} , and m as a function of temperature. The same general features are present in all three quantities.

First we have a closer look at the resistivity ρ_{xx} , as shown in panel (a) in the main panel for the low-temperature part and in the inset over the entire temperature range. The residual resistivity is in the typical semimetallic range with its value of $\rho_0 = 102 \mu\Omega \text{ cm}$. The residual resistivity ratio of the material is rather small with $\rho(T = 300 \text{ K})/\rho_0 \approx 2$. The temperature dependence above $T_c = 15 \text{ K}$ is very well described by the Bloch-Grüneisen formula, including additionally a phenomenological T^3 correction term [269], resulting in

$$\rho(T) = \rho_0 + C \left(\frac{T}{\Theta_R} \right)^5 \int_0^{\frac{\Theta_R}{T}} \frac{x^5 dx}{(e^x - 1)(1 - e^{-x})} - \alpha T^3, \quad (7.1)$$

where Θ_R is the Debye temperature. A fit of the data to this equation from 16 K to room temperature is shown as a red line in the inset of panel (a). The excellent

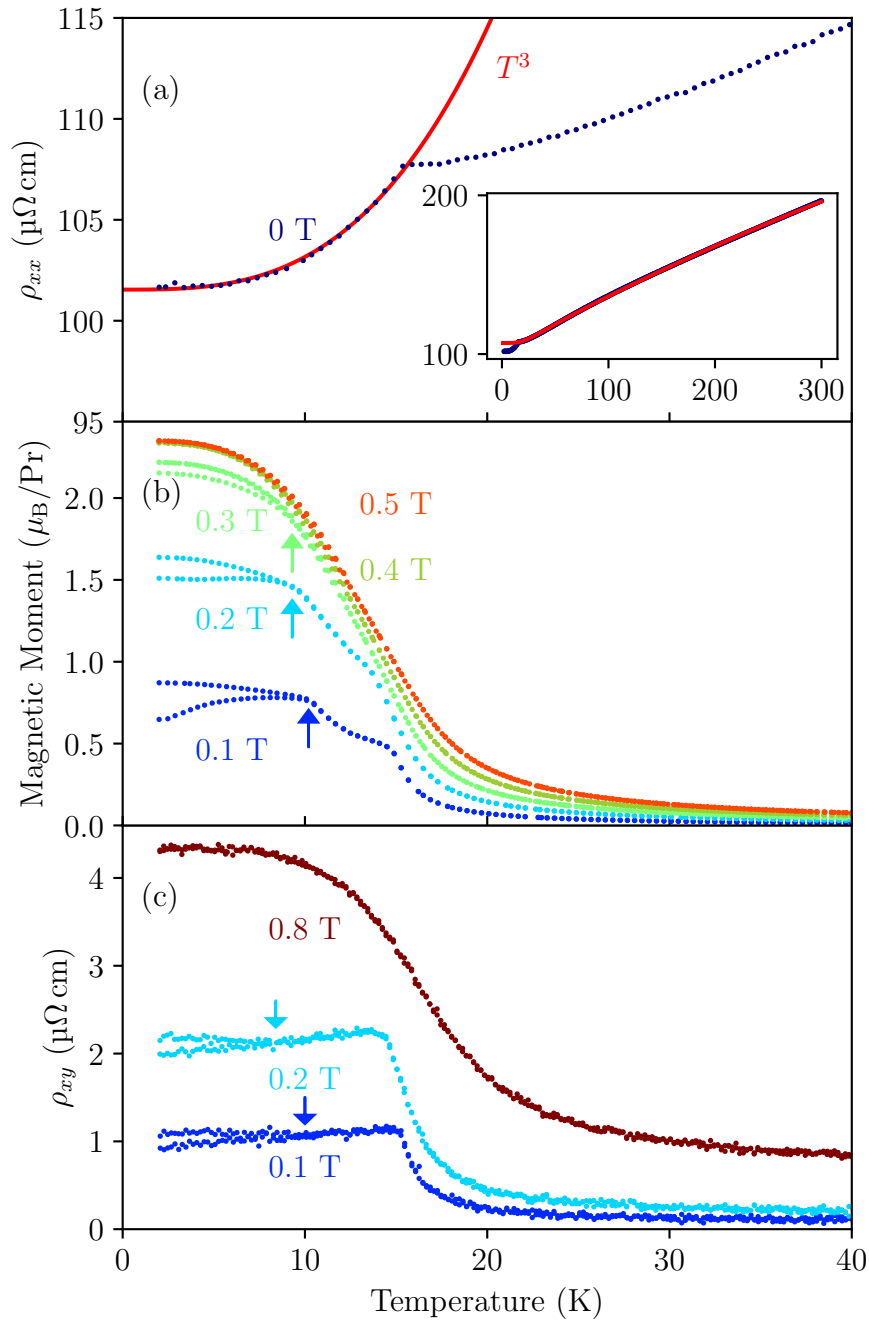


Fig. 7.3 Temperature dependence of (a) the longitudinal resistivity ρ_{xx} , (b) the magnetic moment m , and (c) the Hall resistivity ρ_{xy} (c). The inset in (a) shows the full temperature range of ρ_{xx} . For panel (b) and (c) the zero-field cooled (ZFC) curve branches off from the field-cooled (FC) curve at T_g , marked by arrows. The ZFC branch is in both cases the lower one.

fit to the Bloch-Grüneisen formula indicates that electron-phonon scattering is the dominant scattering process at higher temperatures. According to this formula the resistivity at low temperatures is almost constant. The onset of this flattening can be seen in the resistivity closely above T_c . At T_c a sharp cusp can be observed with an immediate decrease of the resistivity. Below T_c the resistivity is adequately described by a T^3 power law, as indicated by the red line in the main panel.

The magnetic moment as function of temperature is shown in panel (b). For fields below the saturation field B_s a sharp upturn in magnetic moment is observed upon approaching T_c . Below T_c the growth of the magnetic moment is weakened and in some samples enters a plateau, where the magnetic moment is constant over a temperature range of a few Kelvin. Upon reaching T_g , a bifurcation occurs in the magnetic moment curve for zero field cooling and field cooling. The zero field cooled branch has a lower magnetic moment than the field cooled branch. This bifurcation is indicated by arrows in figure 7.3. Above B_s the curves do not show any clear features any more and the magnetic moment saturates at low temperatures, reaching a magnetic-field-independent value of $2.3\mu_B/\text{Pr}$. In other samples this value varies moderately but even up to $3\mu_B/\text{Pr}$ could be observed in flux grown samples. The saturation field was found to vary between 2 T and 4 T, and the critical temperature between 15 K and 16 K. Generally, larger variations could be observed in the flux grown samples as opposed to the floating zone grown samples.

Third, the Hall resistivity ρ_{xy} is shown in panel (c). The curves follow a shape almost identical to that observed for the magnetic moment. Again a sharp increase in ρ_{xy} is observed upon approaching T_c , followed by a plateau phase and a bifurcation below T_g , again indicated by arrows in the figure. This strong similarity between the magnetic moment and the Hall resistivity is already an indication for the anomalous Hall effect. To get a more quantitative insight, the Hall resistivity is plotted against the magnetic moment in figure 7.4. It shows data measured on the same crystal for the case of zero-field cooling. With the exception of the very lowest temperatures we observe a linear behaviour, indicating $\rho_{xy} \propto m$, which shows clearly the anomalous origin of this Hall resistivity.

Next we look at the behaviour of the magnetism and the Hall effect inside the glass phase ($T < T_g$). Figure 7.5 displays the time-dependent magnetization and Hall resistivity below and above T_g . After field-cooling to the indicated temperature in a magnetic field above the saturation field the magnetic field was set to zero and the magnetic moment and Hall resistivity were measured as a function of time. The magnetization was measured over approximately one day, while the Hall resistivity was measured only for around 8 h due to the larger noise which reduces the sensitivity to the small signals after longer times. At $2\text{ K} < T_g$ a decay of the

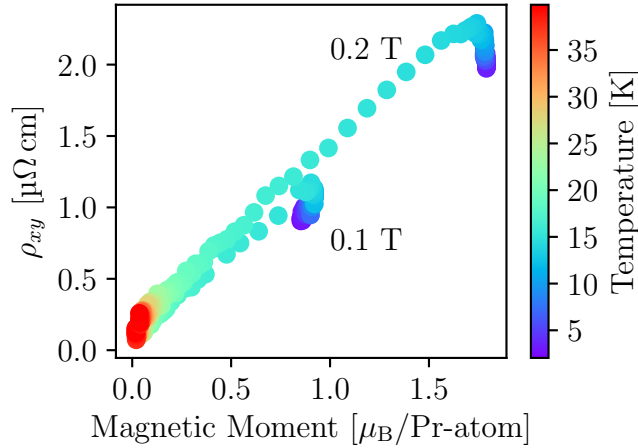


Fig. 7.4 The Hall conductivity plotted against the magnetic moment for two different magnetic fields as indicated, showing the linear dependence of the two quantities. The color bar indicates the temperature.

magnetic moment and the Hall resistivity can be observed, see panel (a). This decay is well described by a stretched exponential with a background remaining after infinite time. The time dependent magnetic moment is thus given by

$$m(t) = \hat{m}e^{-(t/\tau)^\beta} + m_\infty \quad (7.2)$$

and equivalently for the Hall resistivity by

$$\rho_{xy}(t) = \hat{\rho}_{xy}e^{-(t/\tau)^\beta} + \rho_{xy,\infty}. \quad (7.3)$$

Such a decay is typical for spin glasses. The values of $\beta = 0.2$ and $\tau = 0.7$ h are within the range of values reported for other spin glasses [269–271]. The values m_∞ and $\rho_{xy,\infty}$ are both $\neq 0$. Upon changing the fitting window to less than what is shown in figure 7.5, the values of m_∞ and $\rho_{xy,\infty}$ increase. It is thus justified to assume that the values would further decrease for measurements over a longer time-scale than one day. Whether zero can be reached after infinite time or whether some magnetization truly remains, can not be answered. At $12\text{K} > T_g$, the situation looks very different. As seen in figure 7.5(b), almost no time-dependence is observed. The magnetization is growing, but the amplitude is extremely small. The effect can potentially be attributed to the domain walls. For the Hall resistivity, no temperature dependence at all can be seen, but the noise here is noticeably larger than on the magnetic moment. Taken together, these

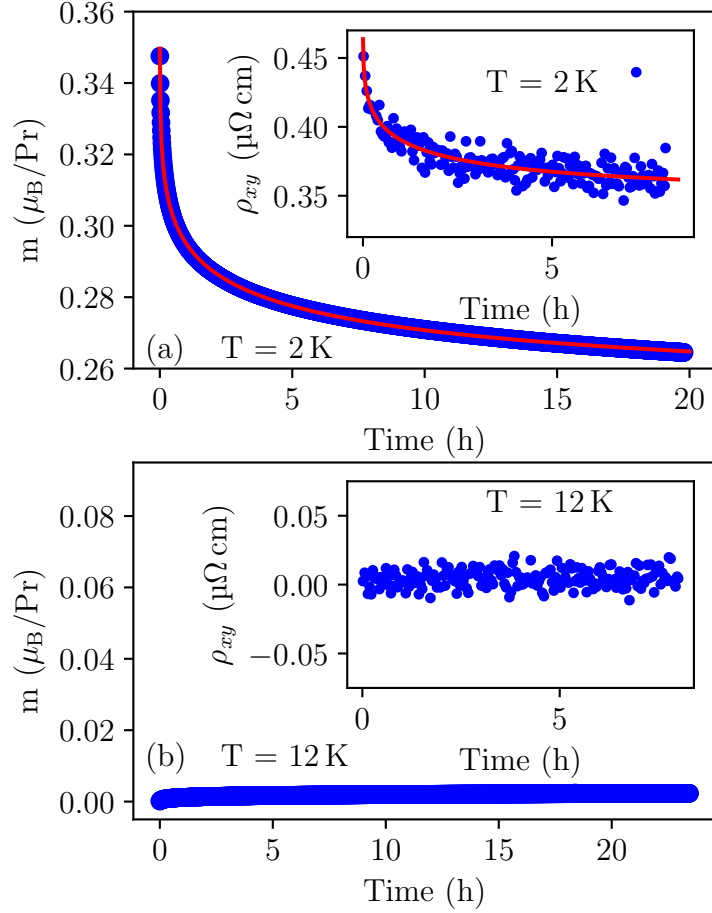


Fig. 7.5 Time dependent measurements of the magnetization (main panel) and Hall resistivity (inset) after field cooling above saturation for 2 K (a) and 12 K (b). Red lines are fits to a stretched exponential (equations 7.2 and 7.3).

data show how the glass transition at T_g changes the time-dependent magnetic behaviour of PrAlGe.

The Hall resistivity as a function of magnetic field is shown in figure 7.6 over the entire field range for selected temperatures between 2 K and 100 K. For high temperatures a purely linear dependence on the magnetic field is observed. The complete lack of deviation from linearity suggests that the Hall effect is strongly dominated by only a single band of hole-like character, as deduced from the positive slope. This justifies the application of the one-band formula of the Hall coefficient (equation 2.30), yielding $p = 7.8 \times 10^{20} \text{ cm}^{-3}$, a value typical for semimetals [145]. The Hall mobility evaluates to $\mu_H = 8 \times 10^{-3} \text{ T}^{-1}$. At lower temperatures a deviation from the linear behaviour is observed in shape of a curved section at low fields which turns again into linear behaviour at higher fields. For $T < T_c$ and

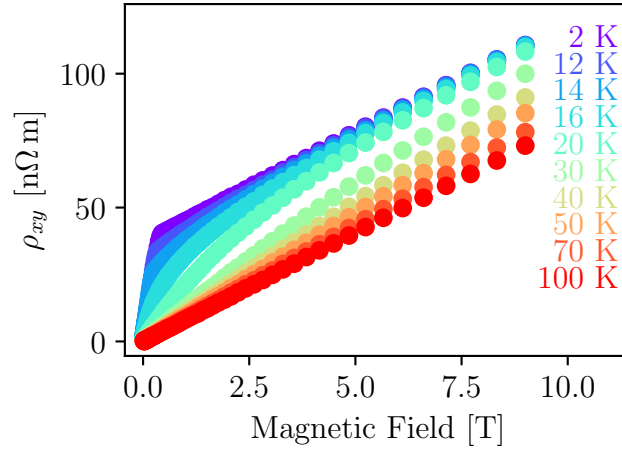


Fig. 7.6 Hall resistivity as function of magnetic field for temperatures as indicated.

very low magnetic fields, a linear increase with a much higher slope than at high temperatures is seen until a sharp kink where the curves flatten off again. At 2 K this effect is at its strongest, where after the sharp kink the curve is linear again with the same slope as the high-temperature measurement, but at higher absolute values. Below T_g the curves are nearly temperature independent. Between T_g and T_c the kink shifts to lower fields until it disappears at T_c . A zoom on this low-field region is shown in figure 7.7(a). The interpretation of the initial steep increase is that this part is due to the anomalous Hall effect. Once saturation is reached, the anomalous part does not increase any longer and only the effects of the quasiparticles are still observed, creating a slope consistent with the one observed at high temperatures.

As a second, independent, method to verify anomalous behaviour in PrAlGe the Nernst effect was measured¹. The low-field behaviour is shown in figure 7.7(b). The same behaviour of a linear high-temperature behaviour and a steeper increase at lower temperatures up to a kink as seen in the Hall resistivity is present here again. At 21 K the Hall coefficient is calculated as $\nu = N/B = 20 \text{ nV}/(\text{K T})$. Together with the mobility this can be converted into the relation $\nu/T = (4.6 \times 10^{-4} \text{ V/K})\mu/T_F$ and thus is very close to the universality curve of the quasiparticle Nernst effect given by equation 2.45.

Figure 7.7(c) shows the extrapolations to zero field of both the Hall conductivity and the Nernst signal. These extrapolations correspond to the pure anomalous contribution. The extrapolations are done by fitting a straight line to the part

¹The thermoelectric measurements have been performed by L. Das from the University of Zurich.

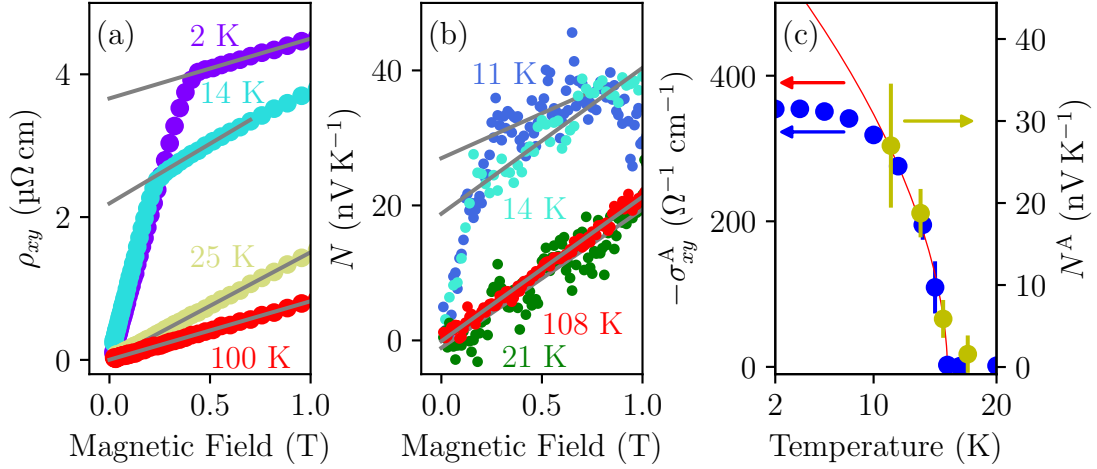


Fig. 7.7 (a) Hall resistivity, (b) Nernst signal, and (c) the extrapolated anomalous Hall conductivity and Nernst signal. Grey lines are linear fits to the data used to extrapolate the anomalous effects to zero magnetic field. The red line in (c) is a fit to a power law of the anomalous Hall conductivity between 11 K and 16.5 K.

above the kink (grey lines in panels (a) and (b)). Error bars are obtained by varying the fitting window to account for slight curvature. Both components agree very nicely and can be fitted with a power law around the increase, as shown by the red line in panel (c).

As the longitudinal counterpart to the Nernst effect the Seebeck effect has been measured, as is shown in figure 7.8. The Seebeck effect is nearly independent of magnetic field and almost linear over a large temperature range. At 14 K a sign change is found from positive at higher temperatures to negative at lower temperatures. The positive Seebeck signal is consistent with the domination of positive charge carriers as observed in the Hall effect.

7.3.2 Magnetoresistance

The magnetoresistance isotherms are shown in figure 7.9. A color plot of the same data is displayed in figure 7.10(a) and the derivative in magnetic field direction is shown in 7.10(b). Some of the effects discussed in the following can be seen more clearly in the color plot. A weakly negative magnetoresistance is observed at 2 K. The isotherm displays a strong curvature and consequently at around 6 T the magnetoresistance crosses 0 and becomes positive for higher fields. Upon increasing the temperature the negative magnetoresistance becomes much more pronounced and the minimum shifts towards higher magnetic fields. At T_c the effect is developed maximally and upon further increases of the temperature the

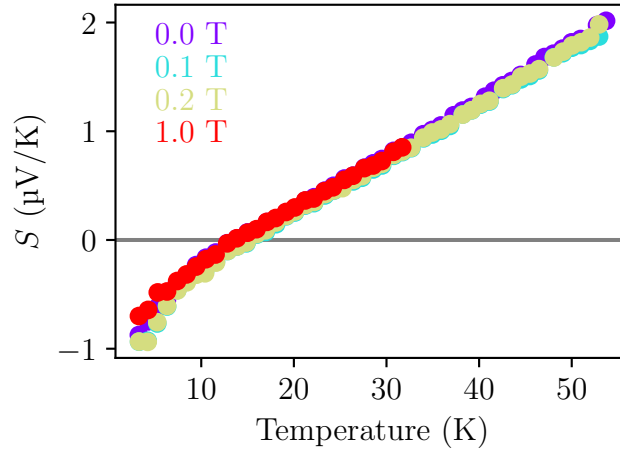


Fig. 7.8 Seebeck effect as function of temperature for magnetic fields as indicated. A sign change is found at 14 K.

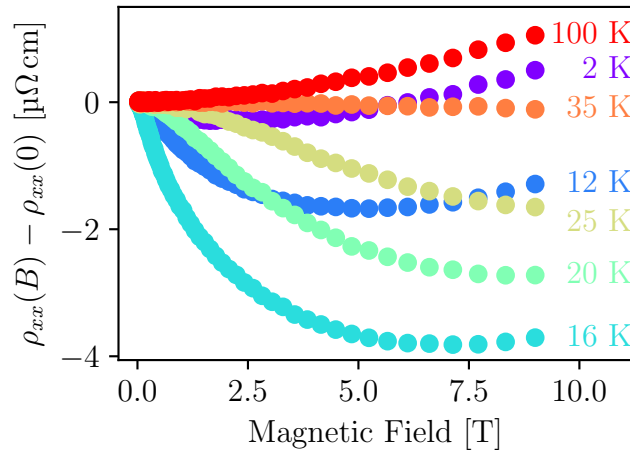


Fig. 7.9 The magnetoresistance of PrAlGe. A clear negative magnetoresistance is observed for temperatures below 40 K for small enough magnetic fields. The strongest effect is reached at T_c .

magnetoresistance weakens. Around 40 K the resistance becomes independent of the magnetic field over the measured range. For temperatures higher than 40 K only a positive magnetoresistance can be observed, which is well described by a power law with exponent 1.7(1). From figure 7.10(b) it can be extrapolated that at around 18 T the slope will be positive for all temperatures and thus a positive magnetoresistance is expected for all temperatures for high enough fields.

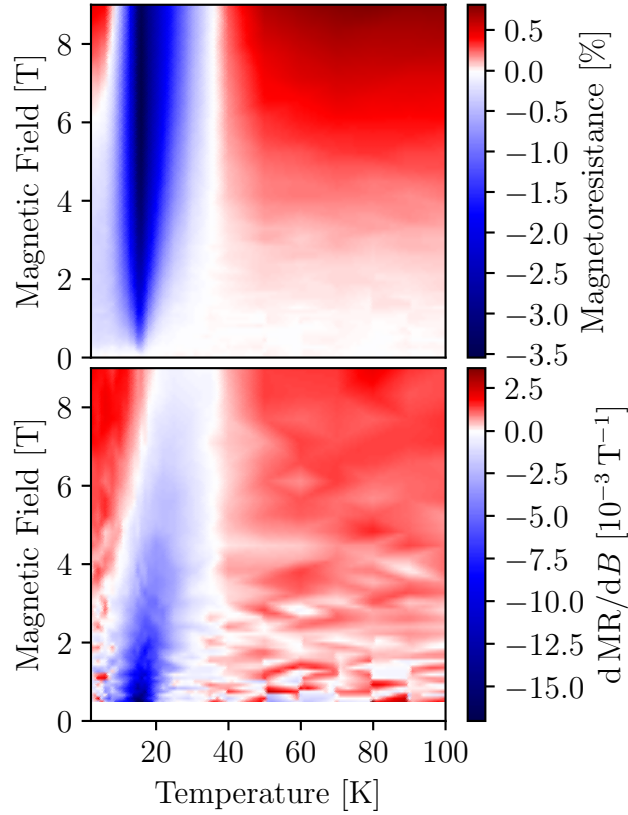


Fig. 7.10 (a) The magnetoresistance of PrAlGe as function of both magnetic field and temperature. The critical temperature at 16 K is visible as the origin of the negative magnetoresistance. (b) The slope of the magnetoresistance. Note that the color scales are not equidistant in the positive and negative regions.

One remarkable difference to the Hall resistivity is the strong temperature dependence of the magnetoresistance below T_g . In this range the Hall isotherms are temperature independent. Between T_g and T_c the high-field part of the Hall isotherms is still only weakly temperature dependent. The rapid changes of the magnetoresistance below T_c are reflected above T_c and no strong deviation in the rate of change can be observed. Only once the negative magnetoresistance disappears above 40 K is a weaker temperature dependence obtained.

7.3.3 AC Magnetization

To further investigate the transition, AC magnetization measurements were performed. The in-phase magnetic moment m' as a function of temperature is shown

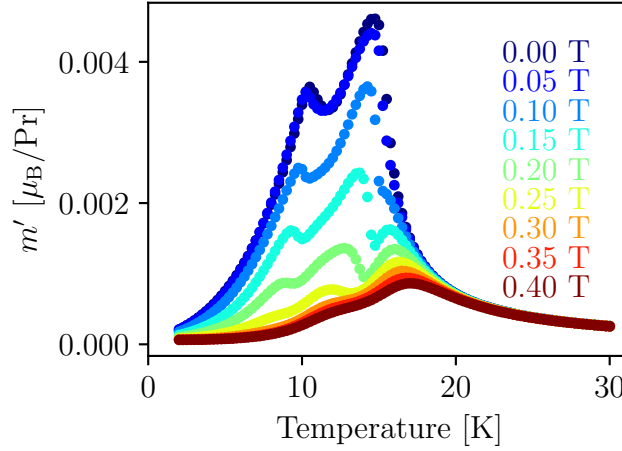


Fig. 7.11 The AC magnetic moment of PrAlGe as a function of temperature measured at a frequency of 100 Hz for different DC background fields as indicated.

in figure 7.11 for a frequency of 100 Hz and magnetic DC fields between 0 and 0.4 T. At 0 DC field two peaks are seen corresponding to T_c and T_g . Upon increasing the DC field, the peak at T_c splits into two peaks. The lower of the two drifts towards lower temperatures upon increasing field while the upper peak shifts towards higher temperatures. The peak at T_g also shifts towards lower temperatures upon increasing the field. The amplitude of all peaks reduces for increasing fields, with the upper half of the T_c peak being the least sensitive to the magnetic field. Upon reaching the saturation field, it is the only peak remaining, albeit as a very broad one.

The frequency dependence of the AC magnetization is shown in figure 7.12 as a function of temperature for the four frequencies 10^1 Hz, 10^2 Hz, 10^3 Hz, and 10^4 Hz. Each of the four panels of figure 7.12 is based on a different DC background magnetic field. The most relevant observation is the frequency dependence of the T_g peak, which displays the behaviour expected for a spin glass with a decrease in amplitude for increasing frequencies. Interestingly, the peak at T_c is almost not frequency dependent at $B = 0$. Upon application of a DC field and the accompanying splitting of the peak into two peaks, the lower one is again frequency dependent while the upper is not.

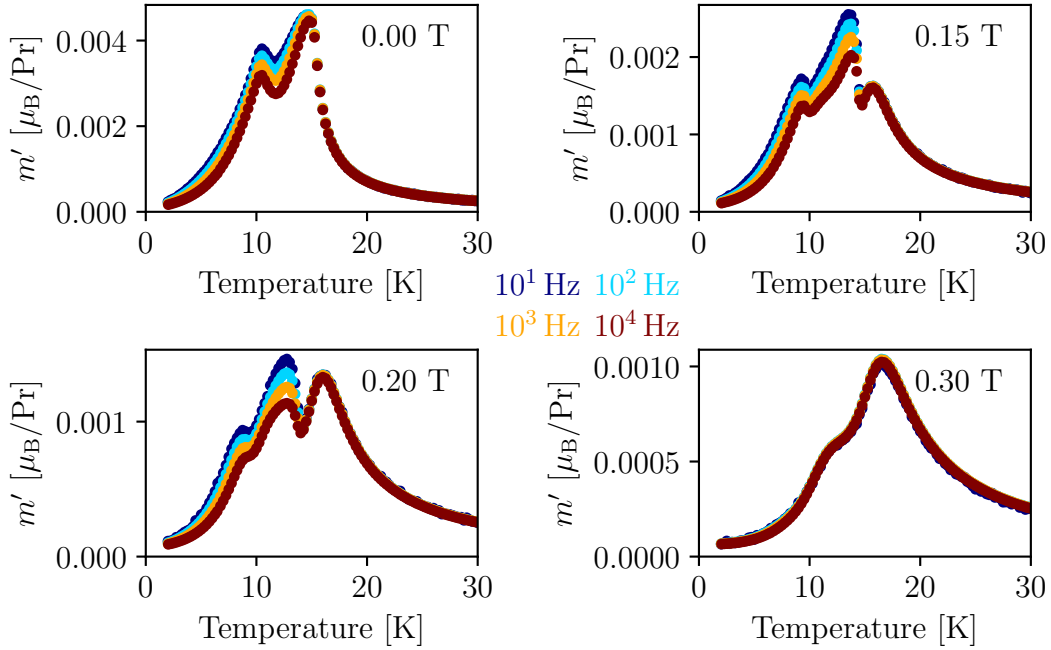


Fig. 7.12 The frequency dependence of the AC magnetic moment of PrAlGe for four different DC background fields.

7.4 Theoretical Results

In this section the theoretical calculations and their results are presented². These predictions are then compared to the experimental observations. The first principal calculations were performed using the Vienna Ab initio Simulation Package (VASP) [272]. The exchange-correlation functional was used within the GGA-PBE approximation. The starting point for the discussion is the band structure, shown in figure 7.13 along the high symmetry lines. The Fermi level is crossed by multiple bands, both electron- and hole-like, with a predominance of hole-like bands. PrAlGe is thus predicted to be a semimetal. Even though many bands cross the Fermi level, no Weyl nodes are located along high symmetry lines [264]. This calculation incorporates spin-orbit-coupling. Without the inclusion of spin orbit coupling, the bands are spin split and can be labelled by their spin. SOC makes the spin not a good quantum number any more and mixing of the spins occurs. Noticeable differences in the density of states for up and down spin exist above the Fermi level, while it presents itself as mostly identical for the two spins below the Fermi level [264]. The magnetic moment that is obtained is $2\mu_B/\text{Pr}$, slightly lower

²The theoretical calculations have been performed by Stepan Tsirkin from the University of Zurich.

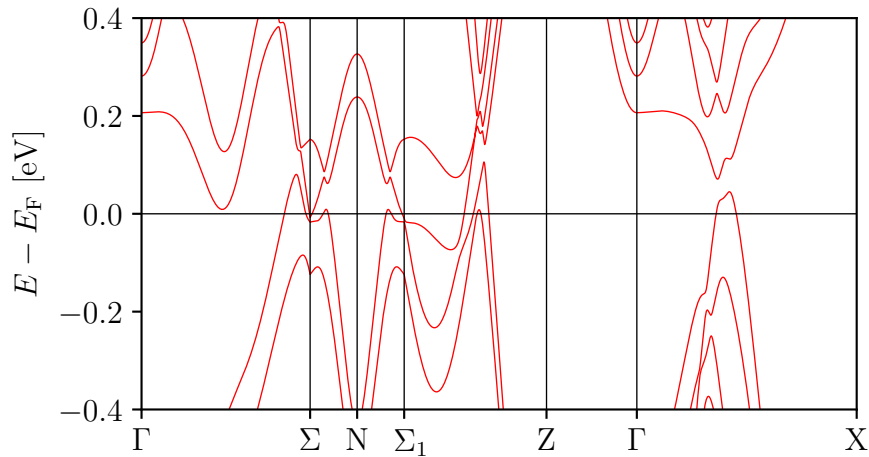


Fig. 7.13 The band structure of PrAlGe close to the Fermi level along the high symmetry lines, with multiple bands crossing the Fermi level. The Weyl nodes are not on the high symmetry directions and can not be seen here [264].

than what is observed experimentally. The location of the Weyl nodes is shown in figure 7.14.

To show more clearly how the Berry curvature affects the anomalous Hall conductivity, a plot of the Berry curvature integrated along k_z is shown in figure 7.15(a) and integrated along k_x and k_y in figure 7.15(b). The Berry curvature dipoles in (b) are indicated by the steep slopes around $k_z \approx 0$ and $k_z \approx 0.5$. They are formed by pairs of Weyl nodes of opposite chirality, which in k -space are separated in z direction. The values of the steps are close to integer values and would be exactly integer values if all Weyl nodes were located precisely at the Fermi level.

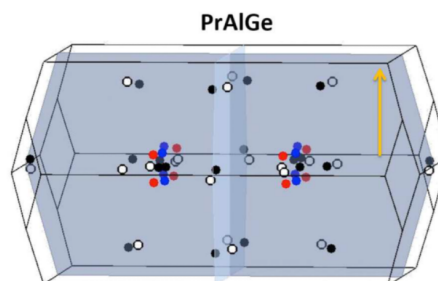


Fig. 7.14 Position of the Weyl nodes in the Brillouin zone. The different colours indicate different chiralities and origins. The orange arrow indicates the magnetization direction. Taken from Ref. [264].

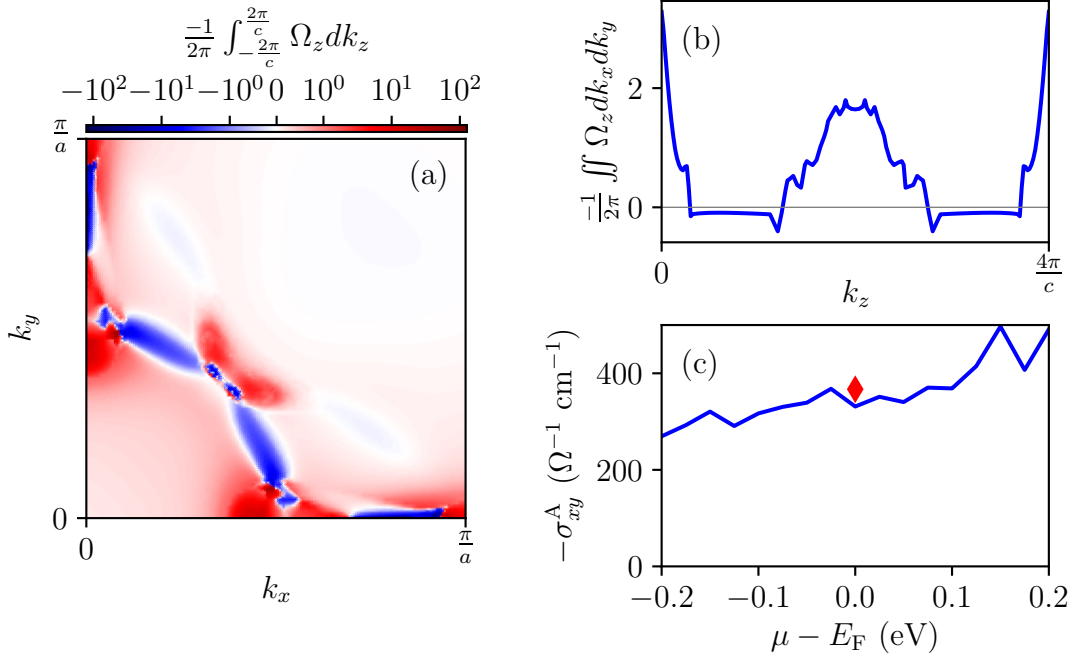


Fig. 7.15 The Berry curvature and the anomalous Hall conductivity following from it. (a) The negative Berry curvature integrated along k_z as a function of k_x and k_y . Only a quarter of the region is shown due to fourfold rotational symmetry. (b) The negative Berry curvature integrated in the $k_x k_y$ -plane. (c) Theoretical calculation for σ_{xy}^A (blue line) for a varying chemical potential compared to the experimental value (red diamond), finding excellent agreement.

In panel (a) the Weyl nodes are indicated by the quick variation from red to blue and vice-versa.

The anomalous Hall conductivity is calculated from the Berry curvature Ω_{kn} by integrating over the whole Brillouin zone:

$$\sigma_{ab}^A = -\frac{e^2}{\hbar} \sum_n \int \theta(\mu - E_{kn}) \epsilon_{abc} \Omega_{kn}^c \left(\frac{dk}{2\pi} \right)^3, \quad (7.4a)$$

$$\Omega_{kn} = \nabla_k \times A_{kn} = -\text{Im} \langle \partial_k u_{kn} | \times | \partial_k u_{kn} \rangle. \quad (7.4b)$$

Here $A_{kn} = i \langle u_{kn} | \partial_k u_{kn} \rangle$ is the Berry connection, θ is the Heaviside step function, E_{kn} is the band energy, and ϵ_{abc} is the antisymmetric tensor. The Anomalous Hall conductivity σ_{xy}^A is then given by Ω^z , provided the magnetic field is along the z direction. The resulting σ_{xy}^A is shown in figure 7.15(c) as a function of chemical potential ± 0.2 eV around the calculated Fermi energy. This variation in chemical potential is incorporated to check for the robustness of the result under small

doping and other inaccuracies of the calculation, which would move the chemical potential slightly. As can be seen, the variation of the chemical potential has little effect on σ_{xy}^A . The value obtained for $\mu = E_F$ is $\sigma_{xy}^A = -330 \Omega^{-1} \text{cm}^{-1}$. This is in excellent quantitative agreement with the experimentally observed value (red diamond).

To make a similar calculation on the Nernst effect is a much more difficult endeavour. While the anomalous Hall effect is given by the Berry curvature of all the occupied bands, the anomalous Nernst effect is given only by the Berry curvature at the Fermi level. The exact position of the Fermi level is thus of great importance. The temperature, furthermore, plays an equally big role due to the Fermi-Dirac distribution. Only at high temperatures the Fermi-Dirac distribution is wide enough to reduce the uncertainties to an acceptable level. Quantitative analyses are thus only done at high temperatures [255]. For these reasons, a calculation for the anomalous Nernst effect is not made.

7.5 Neutron Scattering

None of the measurements or calculations presented so far can give a microscopic explanation for the suppression of the anomalous transport below T_c . For this reason in this section neutron scattering results obtained at PSI are presented³, which can give a first indication of the microscopic details.

The powder neutron diffraction (PND) results are shown in figure 7.16. Upon cooling from 20 K to 1.6 K the scattering intensity increases, as shown in panel (a). This increase is commensurate with the point symmetry of the lattice. Panel (b) shows the fit to the model of ferromagnetism with excellent agreement. The difference between fit and data are shown as a grey line. The green ticks indicate the position of nuclear (top row) and magnetic (bottom row) peaks. Some scattering is only allowed by the magnetism but not by the lattice. Such positions are marked with a * and no scattering can be observed at these position. The magnetic moment obtained from these measurements is $2.29(3)\mu_B/\text{Pr}$.

The small angle neutron scattering (SANS) measurements are shown in figure 7.17. Panels (a) and (b) show the whole two-dimensional SANS pattern measured at base temperature. At zero magnetic field a circularly symmetric pattern emerges which decreases for increasing $|q|$. Upon saturating the sample with an external magnetic field, the SANS signal is strongly reduced. SANS is a technique which probes variations in the magnetization density over length scales between 5 nm to 500 nm. The presence of a SANS signal thus indicates not magnetization

³The neutron scattering experiments were performed and their data analyzed by Jonathan White from PSI.

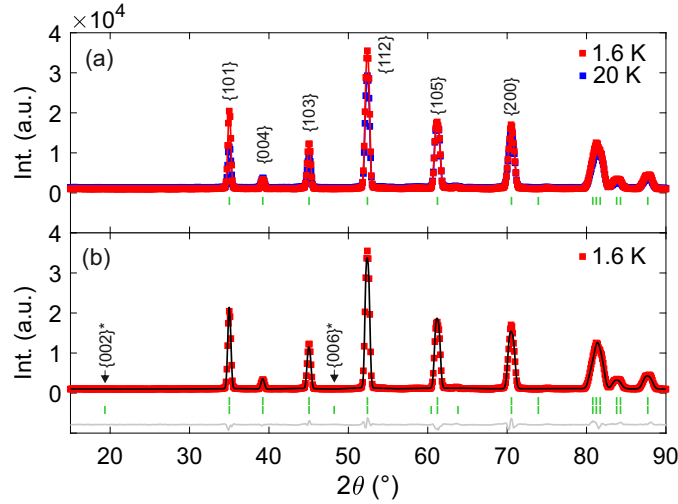


Fig. 7.16 Neutron scattering data of PrAlGe. (a) PND profiles recorded above ($T = 20$ K) and below ($T = 1.6$ K) the critical temperature. The peak amplitude is higher below T_c than above. The green marks indicate expected peak positions as determined by the space group $I4_1md$. (b) Comparison of the refined model (black line) with the data. The grey line represents the difference between model and data. The upper and lower rows of green marks show peak positions of nuclear peaks and magnetic peaks according to the Γ^1 magnetic structure model, respectively. Peaks labelled with * indicate scattering only allowed according to magnetic symmetry.

itself but its variations. The disappearance of the SANS pattern above saturation is thus an indication of the disappearance of magnetic variations. Below saturation there is a component of the magnetization which is not aligned along the c -axis. A potential interpretation is the formation of extended domain walls. Due to the rotational symmetry, an azimuthally averaged data set is an easier way to visualize the data. This is done in panel (c) for the $B = 0$ case. It is seen very clearly how above T_c the scattering intensity is very low and temperature independent. This intensity thus constitutes the background. Below T_c the intensity increases fast and reaches its maximum around T_g , after which there is no variation for the lowest values of $|q|$ but the temperature dependence remains for higher $|q|$. Panel (d) shows the total scattering without the background for each temperature. The blue line is a fit to a power law. Finally, panel (e) shows the decrease in SANS intensity at base temperature upon increase of the magnetic field with the vanishing of the intensity at the saturation field.

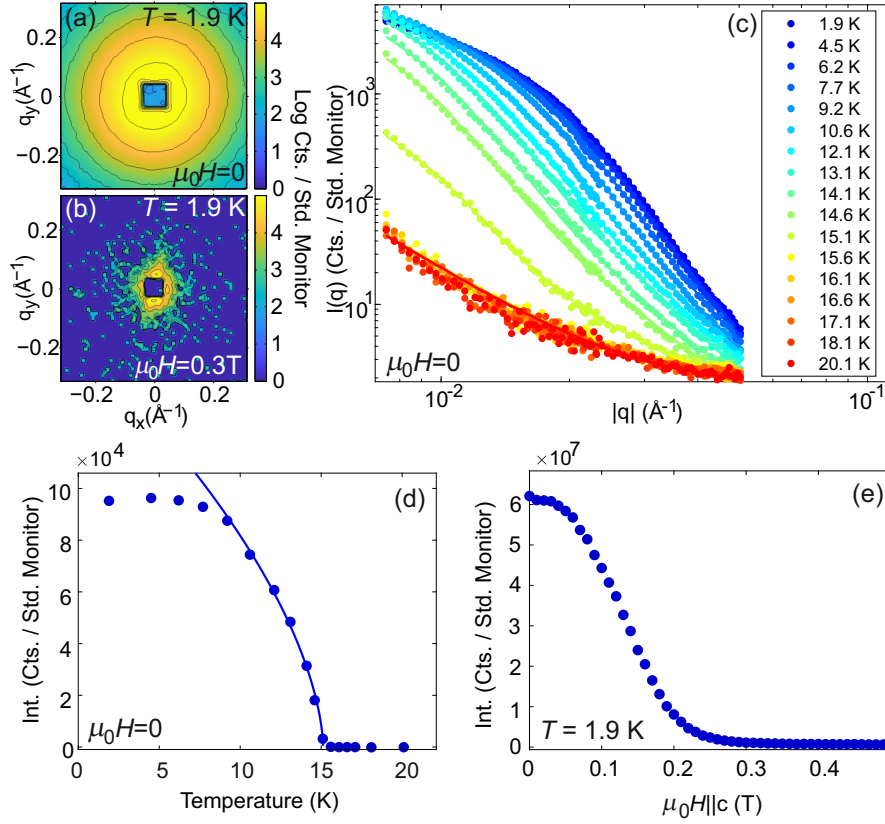


Fig. 7.17 Zero field SANS pattern (a) and SANS pattern above saturation (b) at base temperature after zero-field cooling along the [001] axis. The square pattern in the middle is due to the beam stop. (c) Zero-field azimuthally averaged intensity as function of $|q|$ for temperatures as indicated. The solid lines are fits to the model. (d) The contribution of magnetic scattering to the curves shown in (c). The solid line is a fit to a power law. (e) A scan with increasing B of the SANS intensity.

7.6 Discussion

In this section a closer look is taken at the results. Furthermore results from the different measurement and the theoretical calculations are compared and interpreted and an attempt at creating a unified picture of the magnetic properties of PrAlGe and its influence on the topology is made.

Further insight into the magnetic properties can be obtained by an Arrot plot. It is based on the Ginzburg-Landau mean field theory, according to which around the critical temperature the free energy of a system can be written in an expansion as

$$F(M) = -MH + \frac{aM^2}{2} + \frac{bM^4}{4} + \dots \quad (7.5)$$

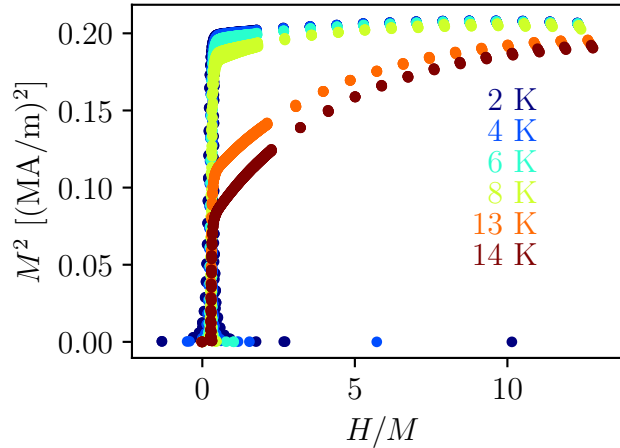


Fig. 7.18 Arrott plot of PrAlGe. The positive axis intercept indicates ferromagnetism.

with temperature dependent parameters a , and b . At the critical temperature the magnetization is then, assuming $\partial F/\partial M = 0$, expected to follow

$$M^2 = \frac{H}{bM} - \frac{a}{b}. \quad (7.6)$$

When plotting M^2 vs H/M , conclusions about the magnetic properties of the sample can be drawn. Such a plot is shown in figure 7.18. Inside a ferromagnetic state, a positive axis intercept is expected, opposed to a negative axis intercept for a paramagnet. At the critical temperature no axis intercept is expected. The data thus confirms the presence of ferromagnetism and indicates its weakening upon approach of T_c .

The magnetization and SANS data consistently show ferromagnetic behaviour once a magnetic field is aligned. Below saturation, the ferromagnetic properties are reduced and SANS starts to pick up a signal. Over a nanometric length-scale, the magnetization tilts away from the c -axis, most likely these are the domain walls. This picture is consistent with the formation of domains. No net magnetization is observed at zero magnetic field, meaning there is an equal amount of sample magnetized in both directions. An applied field then aligns the different domains which causes a decrease in the SANS as domain walls disappear. The Hall effect and Nernst effect measurements support this scenario. The different domains contribute with different sign to the total observed effects. At zero field, when the domains are equally distributed, no anomalous Hall or Nernst effects are observed. Upon aligning the domains, the components of opposite sign do no longer cancel

and finite anomalous contributions start to emerge. Once the saturation field is reached, the growth of the anomalous component stops and the further increase in the Hall and Nernst effects are caused by the quasiparticles. The SANS measurements further support this scenario when fitted with a model based on cycloidal tilting of the magnetic moments. The solid lines in figure 7.17(c) are based on this model. From these fits the length scale of the variation in magnetization can be obtained as 14 nm at 2 K and 25 nm close to T_c . The model used does not, however, determine the spin structure in a unique way and other more complicated models can describe the data as well. The origin of the magnetization tilting away from c can be attributed to different processes, such as the Dzyaloshinskii-Moriya interaction given by

$$H_{\text{DM}} = \vec{D}_{ij} \cdot (\vec{S}_i \times \vec{S}_j) \quad (7.7)$$

which favour spin canting. Another possible explanation is the interactions with in-plane antiferromagnetism.

In such a domain wall scenario as described before it is expected that a new conductivity channel forms due to Fermi arcs which exist between adjacent regions of different magnetization. The different magnetizations leads to different separation of the Weyl nodes. Between the projections Fermi arcs are expected, which increase the Fermi surface and thus add a new conductivity channel. The expectation would thus be that an increasing magnetic field, through aligning the domains, would increase the resistivity. However, the magnetoresistance data do not support this picture and instead the opposite effect is found.

An alternative explanation for the behaviour of the magnetoresistance is that less scattering occurs because of the alignment of the magnetization. This leads to a reduction of spin disorder scattering when less domain walls are present. A fully spin polarized sample is expected to experience less resistivity than a paramagnetic sample with random spin orientation. Such effects typically occur in magnetic materials [273]. The magnetoresistance is, however, not at its minimum for B_s but instead decreases further up to fields around 7 T for temperatures below T_c . Above T_c the decrease is present at least up to 9 T, the highest field available during the measurement. The eventual upturn expected for all curves is again consistent with the expectation of increased scattering due to cyclotron motion.

With its magnetic structure PrAlGe could be a material suitable for the investigations of axial gauge fields [274]. Such axial gauge fields have been realized in various systems, but never in a hard condensed matter system. The strong dependence of the domains on magnetic fields propagates to the axial gauge field, which could thus be tunable as well.

The temperature dependence of σ_{xy}^A can in a small temperature range below T_c be described by

$$\sigma_{xy}^A \propto \left(1 - \frac{T}{T_c}\right)^{2\beta}. \quad (7.8)$$

The fit to this equation is shown in figure 7.7(c). The exponent β is given by 0.28(4). The same formula can be used to fit the SANS data. This is done in figure 7.17(d), where the value $\beta = 0.30(1)$ is found in agreement with the anomalous Hall conductivity and the theoretical value of 0.325 for a three-dimensional Ising model.

The spin glass behaviour is another interesting phenomenon present in PrAlGe. How the magnetism is really influenced by it on a microscopic level can not be answered from the data presented in this chapter, but a connection to the domain walls seem likely. The observation of negative magnetoresistance together with anomalous Hall and, at lower temperature, even a spin glass, is not a very common occurrence, but it has been made, for example, in $\text{La}_{1-x}\text{Ca}_x\text{CoO}_3$ [275].

The comparison to other materials is shown in figure 7.19. The red diamonds are our values for PrAlGe: anomalous Hall angle $\Theta_H^A = 3.7\%$, anomalous Hall conductivity $\sigma_{xy}^A = -367 \Omega^{-1} \text{cm}^{-1}$, and anomalous Hall factor $S_H = \sigma_{xy}^A/M = 0.087 \text{V}^{-1}$. The blue points are values from the literature while blue ellipses indicate substitution systems or variations in measurement results for one material. The blue band in panel (c) indicates the region where many ferromagnets are situated. From panels (a) and (b) we can see that PrAlGe is a material with a rather high anomalous Hall effect. The anomalous Nernst effect as seen in panel (c) is in the range that is found for non-topological ferromagnetic materials, thus not unusually large. Other topological materials, such as $\text{Me}_{3+x}\text{Sn}_{1-x}$, $\text{Co}_3\text{Sn}_2\text{S}_2$, and Co_2MnGa have an anomalous Nernst effect that is multiple orders of magnitude larger than what is observed in PrAlGe.

The theoretical calculations of the anomalous Hall conductivity and their excellent agreement with the experimental findings clearly prove that the anomalous Hall effect is a purely intrinsic effect and topological in nature, originating from the Berry curvature due to the presence of Weyl nodes. A link between the anomalous thermoelectric coefficient α_{xy}^A and the anomalous Hall conductivity σ_{xy}^A is given by the Mott relation (equation 2.41) which is still valid in the case of anomalous transport coefficients [276]. By taking the data presented in figure 7.15(c) to evaluate $\partial\sigma/\partial\mu|_{E_F}$ we obtain the value $\alpha_{xy}^A/T = 6 \mu\text{V}/(\text{K} \Omega \text{cm})$. One major drawback of this relation is the dependence on the derivative $\partial\sigma_{xy}^A/\partial\mu$ at the Fermi level. Experimentally this value is unobtainable for us without any samples with small substitutions to change the chemical potential. Even from a theoretical standpoint this value is difficult to obtain, as the calculation of derivatives is always

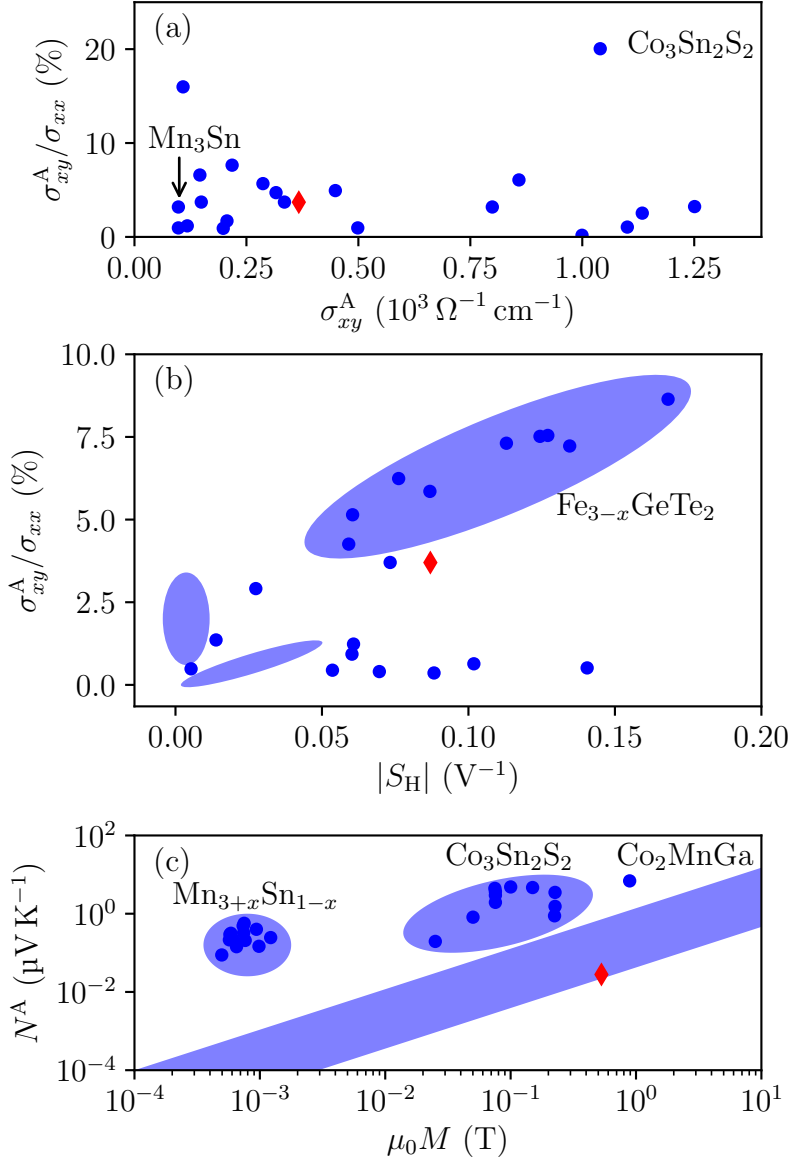


Fig. 7.19 Comparison of the anomalous responses of PrAlGe to other materials. (a) Anomalous Hall angle vs anomalous Hall conductivity. (b) Anomalous Hall angle vs anomalous Hall factor. Blue ellipses indicate substitution systems. (c) Anomalous Nernst signal vs magnetization. The blue band indicates the typical region for ferromagnets. The red diamonds indicated results from this study. Blue points are taken from the literature: Ref. [252] for panel (a), Ref. [253] for panel (b), and Refs. [255] and [257] for panel (c).

a bigger numerical challenge than the calculation of value itself. Publications in other materials are dealing with the same problems. Nonetheless it useful to

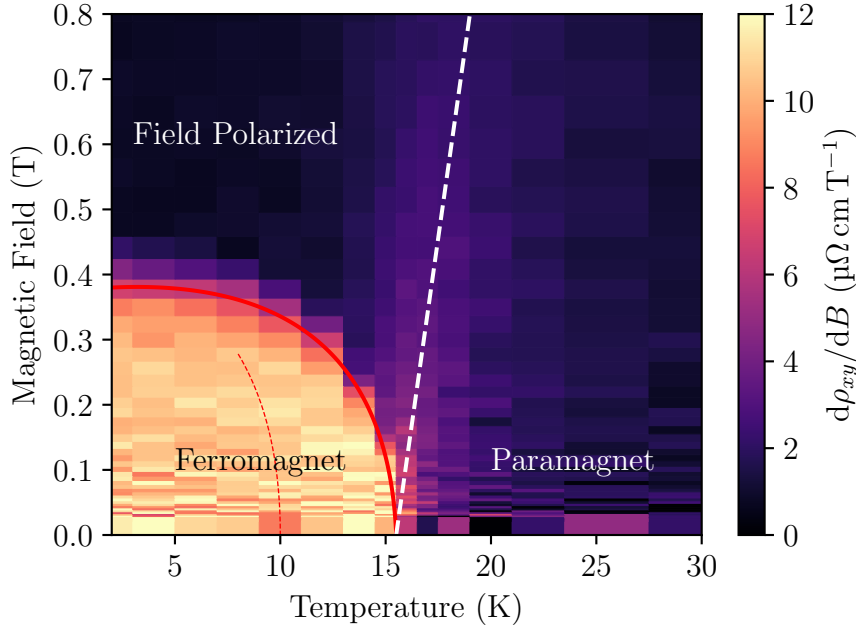


Fig. 7.20 Phase diagram of PrAlGe. The coloured background is obtained from the Hall effect measurements. The thick red line indicates the ferromagnetic ground state. The red dashed line indicates the glass transition. For higher fields and temperature, a field polarized state and paramagnetic state are found, respectively.

make the comparison between the experiment and the theory. The anomalous off-diagonal Peltier-coefficient can be connected to the anomalous Nernst response with [175, 277]

$$\alpha_{xy}^A = \sigma_{xx} N^A + \sigma_{xx} S \left(\frac{\sigma_{xy}^A}{\sigma_{xx}} + \frac{\kappa_{xy}^A}{\kappa_{xx}} \right). \quad (7.9)$$

Since we observe a zero crossing in S at 14 K the second term vanishes around this temperature range and the equation reduces to $\alpha_{xy}^A = \sigma_{xx} N^A$. At this temperature we thus get $\alpha_{xy}^A/T = 14 \mu\text{V}/(\text{K}^2 \Omega \text{cm})$ which is in reasonable agreement with the prediction given all the problems discussed above.

Taking all the measurements into account we draw again a phases diagram, this time based on real data, which is shown in figure 7.20. The background color is drawn according to the derivative of the Hall resistivity $d\rho_{xy}/dB$ and gives a very sharp phase boundary.

The compound PrAlGe offers many possibilities for future investigations into topological materials. As discussed, the full substitution of the rare-earth ion will result in different types of Weyl cones at the Fermi level and different magnetic

properties. A partial substitution can be expected to interpolate between different behaviours. A further road is the full or partial substitution of the non-magnetic atoms. This can open a new way of tuning the Weyl nodes and the topological properties, next to other methods such as the rotation of a uniform magnetization [278], photoinduction [279, 280], or pressure induction [281].

7.7 Conclusion

In this chapter a combined study of magnetism, electric transport, thermoelectric transport, small angle neutron scattering, and theoretical calculations has been presented. Together these results give a convincing and coherent picture of the magnetism and its links to the topology. The ground state is found to be a ferromagnet with domains which suppress the observation of anomalous transport properties. Upon alignment of the magnetization with an external magnetic field the anomalous transport is recovered. The experimental value of the anomalous Hall conductivity agrees perfectly with a first principle calculation, proving its topological origin.

The results of this chapter will be published by D. Destraz et al. The main contributions from the co-authors are as follows: The samples were grown by P. Puphal and E. Pomjakushina, the neutron experiments were performed by J. White, the thermoelectric transport by L. Das and the theoretical calculations by S. Tsirkin. Further theoretical support came from T. Neupert and A. Grushin. The paper was written jointly by the authors with dominant contributions from by D. Destraz, and J. White.

Chapter 8

Summary and Outlook

In this thesis multiple phenomena related to materials of contemporary interest and physical properties have been investigated with a focus on transport phenomena. In this last chapter the results are summarized and an outlook is given on how the field is expected to continue.

The first three science chapters presented results on NbN films of different thickness. In the thicker films, a sign change in the Hall resistivity is observed at low magnetic fields originating from superconducting fluctuations. All observed properties could be described well with Gaussian fluctuation theory. The paraconductivity follows the two-dimensional Aslamazov-Larkin behaviour and the Hall conductivity is well described by a recent theoretical calculation. This agreement is achieved without any adjustable parameters. In thinner films the picture is very different. A BKT transition is found in the resistivity and the paraconductivity follows the zero-dimensional Aslamazov-Larkin behaviour for some samples, while for others the two-dimensional behaviour is found. Multiple sign changes are observed in the Hall resistivity, showing a clear deviation from Gaussian fluctuation theory. The behaviour we find is strongly reminiscent of cuprate superconductors in the pseudogap. Further investigations in the conventional superconductor NbN might help to understand the pseudogap in the cuprates. Under very high magnetic fields at temperatures only reached by dilution refrigerators, a superconductor-insulator transition could be observed, extending the validity of the theory to films with relatively high T_c and a high B_{c2} . A very high value of $z\nu$ was found and investigations of films with medium thickness could help to explain the origin of the large value.

In the substitution compound $\text{Ca}_{1.8}\text{Sr}_{0.2}\text{RuO}_4$ strong evidence of a quantum critical point has been found. The magnetic-field- and temperature-dependent resistivity and exponent α follow the expectation for a quantum critical point and show clear maxima or minima at the quantum critical point. With this find-

ings $\text{Ca}_{1.8}\text{Sr}_{0.2}\text{RuO}_4$ could be linked more closely to its bilayer sister-compound $\text{Sr}_3\text{Ru}_2\text{O}_7$. This might lead to a better understanding of the nematic phase in $\text{Sr}_3\text{Ru}_2\text{O}_7$. Many properties of $\text{Ca}_{1.8}\text{Sr}_{0.2}\text{RuO}_4$ are also similar to the end member Sr_2RuO_4 and might lead to a better understanding of the electronic behaviour in this superconductor.

The compound PrAlGe was found to be a Weyl semimetal as predicted by theoretical calculations. The ground state is, however, hiding the anomalous transport properties due to the formation of domains. Upon alignment of the domains with an external magnetic field, the anomalous transport properties are recovered and excellent agreement between the experimentally observed Hall conductivity to the theoretically predicted one proves that the anomalous Hall effect stems from the Weyl nodes. Through SANS measurements it could be determined that the length scale over which the magnetization tilts away from the c -axis is around 20 nm. Furthermore, glassy behaviour was observed in the magnetization. By partially substituting either the rare earth atom or the nonmagnetic atoms it is expected that the topological properties in PrAlGe can be tuned. Such investigations into the substitution systems will certainly yield interesting results. As the field of topology is viewed favourably in terms of future applications such investigations are of great interest.

Acknowledgements

Foremost I want to thank my advisor Johan Chang. His help, guidance, and advice during my PhD project is greatly appreciated. He did an excellent job in supervising my research. Furthermore I want to thank the other members of Johan's research group, especially Lakshmi Das, who worked in the lab with me and became a good friend of mine.

With my office mate Xiaofu I had good discussions on thin films and measurement machinery. His experience of quantum critical behaviour in thin films was of great help.

During my visits at the high magnetic field laboratory in Grenoble I received a lot of help from David Le Boeuf. I am very grateful for his excellent technical and scientific support and the great hospitality, especially considering that we were always working the night shift. Many other members of the staff were also very supportive. I hope there will be more collaborations between our group and David in the future.

For the $\text{Ca}_{1.8}\text{Sr}_{0.2}\text{RuO}_4$ I received a lot of support from Jakub Vonka during the measurements in the dilution refrigerator at PSI. We worked long days and over the weekend right before Christmas but his happy personality and experience with dilution refrigerators made the experiment an exciting time.

To Jonathan White I want to express my gratitude for the great collaboration on the PrAlGe project. For theoretical support, simulations, and interesting discussions on this project I want to thank the theorists Titus Neupert and Stepan Tsirkin.

The samples I used for my measurements came from many places. I want to especially thank Konstantin Ilin from the Karlsruhe Institute of Technology for growing the NbN films, and discussions during the project, Pascal Puphal for growing the PrAlGe crystals, and Antonio Vecchione, Rosalba Fittipaldi, and Veronica Granata for the $\text{Ca}_{1.8}\text{Sr}_{0.2}\text{RuO}_4$ single crystals.

During the early stages of my PhD project I received a lot of help from Henrik Grundmann and Andreas Engel. For their support and motivation I thank them a lot. The discussions with them helped me greatly in figuring out what I want to do during my PhD and afterwards.

To the other members of my PhD committee, Andreas Schilling and Benoît Fauqué, I express my gratitude in their support during my time as a PhD student and the interesting discussions during the meetings of the PhD committee.

The members of the mechanical and electronics workshops supported my research tremendously by building and repairing all sorts of equipment. I want to thank especially Reto Maier, Achim Vollhardt, and Daniel Florin. Whenever something broke in our laboratory, which happens regularly, these people offered fast and uncomplicated help in fixing our machines, especially the two PPMS. The physics institute is blessed to have such great people working here.

Publications

Daniel Destraz, Lakshmi Das, Stepan S. Tsirkin, Y. Xu, Titus Neupert, J. Chang, A. Schilling, Adolfo G. Grushin, Joachim Kohlbrecher, L. Keller, Pascal Puphal, Ekaterina Pomjakushina, and J.S. White

“Magnetism and anomalous transport in the Weyl semimetal PrAlGe: Possible route to axial gauge fields”

under review at npj Quantum Materials

Ivica M. Bradarić, Vladimir M. Matić, Ilija Savić, Zlatko Rakočević, Maja Popović, Daniel Destraz, and Hugo Keller

“Anomalous magnetic properties of CaRuO_3 probed by AC and DC magnetic measurements and by low Ti impurity doping”

Phys. Rev. B **98**, 134436 (2018)

C. E. Matt, D. Sutter, A. M. Cook, Y. Sassa, M. Månsson, O. Tjernberg, L. Das, M. Horio, D. Destraz, C. G. Fatuzzo, K. Hauser, M. Shi, M. Kobayashi, V. N. Strocov, T. Schmitt, P. Dudin, M. Hoesch, S. Pyon, T. Takayama, H. Takagi, O. J. Lipscombe, S. M. Hayden, T. Kurosawa, N. Momono, M. Oda, T. Neupert & J. Chang

“Direct observation of orbital hybridisation in a cuprate superconductor”

Nature Communications **9**, 972 (2018)

O. Ivashko, L. Yang, D. Destraz, E. Martino, Y. Chen, C. Y. Guo, H. Q. Yuan, A. Pisoni, P. Matus, S. Pyon, K. Kudo, M. Nohara, L. Forró, H. M. Rønnow, M. Hücker, M. v. Zimmermann & J. Chang

“Charge-Stripe Order and Superconductivity in $\text{Ir}_{1-x}\text{Pt}_x\text{Te}_2$ ”

Scientific Reports **7**, 17157 (2017)

O. Ivashko, N. E. Shaik, X. Lu, C. G. Fatuzzo, M. Dantz, P. G. Freeman, D. E. McNally, D. Destraz, N. B. Christensen, T. Kurosawa, N. Momono, M. Oda, C. E. Matt, C. Monney, H. M. Rønnow, T. Schmitt, and J. Chang

“Damped spin excitations in a doped cuprate superconductor with orbital hybridization”

Phys. Rev. B **95**, 214508 (2017)

Daniel Destraz, Konstantin Ilin, Michael Siegel, Andreas Schilling, and Johan Chang

“Superconducting fluctuations in a thin NbN film probed by the Hall effect”
Phys. Rev. B **95**, 224501 (2017)

F. Laliberte, W. Tabis, S. Badoux, B. Vignolle, D. Destraz, N. Momono, T. Kurosawa, K. Yamada, H. Takagi, N. Doiron-Leyraud, C. Proust, Louis Taillefer

“Origin of the metal-to-insulator crossover in cuprate superconductors”
arXiv:1606.04491 (2016)

Bibliography

- [1] Matthias Vojta
“Quantum phase transitions”
Reports on Progress in Physics **66**, 2069 (2003)
- [2] J. Custers, P. Gegenwart, H. Wilhelm, K. Neumaier, Y. Tokiwa, O. Trovarelli, C. Geibel, F. Steglich, C. Pépin, and P. Coleman
“The break-up of heavy electrons at a quantum critical point”
Nature **424**, 524 (2003)
- [3] Heike Kamerlingh Onnes
“Further experiments with liquid helium. C. On the change of electric resistance of pure metals at very low temperatures etc. IV. The resistance of pure mercury at helium temperatures”
KNAW Proceedings **13**, 1274 (1911)
- [4] Heike Kamerlingh Onnes
“Further experiments with Liquid Helium. D. On the change of Electrical Resistance of Pure Metals at very low Temperatures, etc. V. The Disappearance of the resistance of mercury”
KNAW Proceedings **14**, 113 (1911)
- [5] Heike Kamerlingh Onnes
“Further experiments with Liquid Helium G. On the electrical resistance of Pure Metals etc. VI. On the Sudden Change in the Rate at which the Resistance of Mercury Disappears”
KNAW Proceedings **14**, 818 (1912)
- [6] Heike Kamerlingh Onnes
“Further experiments with liquid helium. H. On the electrical resistance of pure metals etc. VII. The potential difference necessary for the electric current through mercury below $4^{\circ}.19\text{K}$ ”
KNAW Proceedings **15**, 1406 (1913)
- [7] J. Bardeen, L. N. Cooper, and J. R. Schrieffer
“Microscopic Theory of Superconductivity”
Phys. Rev. **106**, 162 (1957)
- [8] J. Bardeen, L. N. Cooper, and J. R. Schrieffer
“Theory of Superconductivity”
Phys. Rev. **108**, 1175 (1957)
- [9] Leon N. Cooper
“Bound Electron Pairs in a Degenerate Fermi Gas”
Phys. Rev. **104**, 1189 (1956)
- [10] J. G. Bednorz and K. A. Müller
“Possible high T_c superconductivity in the Ba-La-Cu-O system”
Zeitschrift für Physik B Condensed Matter **64**, 189 (1986)

- [11] A. Schilling, M. Cantoni, J. D. Guo, and H. R. Ott
“Superconductivity above 130 K in the Hg-Ba-Ca-Cu-O system”
Nature **363**, 56 (1993)
- [12] Jun Nagamatsu, Norimasa Nakagawa, Takahiro Muranaka, Yuji Zenitani, and Jun Akimitsu
“Superconductivity at 39 K in magnesium diboride”
Nature **410**, 63 (2001)
- [13] Marvin L. Cohen and P. W. Anderson
“Comments on the Maximum Superconducting Transition Temperature”
AIP Conference Proceedings **4**, 17 (1972)
- [14] Denys Sutter
“Strong Electron Correlations in the Ruthenates — A Spectroscopic Study of Ca_2RuO_4 and $\text{Ca}_{1.8}\text{Sr}_{0.2}\text{RuO}_4$ ”
PhD Thesis, University of Zurich (2019)
- [15] B. Keimer, S. A. Kivelson, M. R. Norman, S. Uchida, and J. Zaanen
“From quantum matter to high-temperature superconductivity in copper oxides”
Nature **518**, 179 (2015)
- [16] S. Martin, A. T. Fiory, R. M. Fleming, L. F. Schneemeyer, and J. V. Waszczak
“Normal-state transport properties of $\text{Bi}_{2+x}\text{Sr}_{2-y}\text{CuO}_{6+\delta}$ crystals”
Phys. Rev. B **41**, 846 (1990)
- [17] Makoto Hashimoto, Inna M. Vishik, Rui-Hua He, Thomas P. Devereaux, and Zhi-Xun Shen
“Energy gaps in high-transition-temperature cuprate superconductors”
Nature Physics **10**, 483 (2014)
- [18] Aakash Pushp, Colin V. Parker, Abhay N. Pasupathy, Kenjiro K. Gomes, Shimpei Ono, Jinsheng Wen, Zhijun Xu, Genda Gu, and Ali Yazdani
“Extending Universal Nodal Excitations Optimizes Superconductivity in $\text{Bi}_2\text{Sr}_2\text{CaCu}_2\text{O}_{8+\delta}$ ”
Science **324**, 1689 (2009)
- [19] O. Cyr-Choinière, R. Daou, F. Laliberté, C. Collignon, S. Badoux, D. LeBoeuf, J. Chang, B. J. Ramshaw, D. A. Bonn, W. N. Hardy, R. Liang, J.-Q. Yan, J.-G. Cheng, J.-S. Zhou, J. B. Goodenough, S. Pyon, T. Takayama, H. Takagi, N. Doiron-Leyraud, and Louis Taillefer
“Pseudogap temperature T^* of cuprate superconductors from the Nernst effect”
Phys. Rev. B **97**, 064502 (2018)
- [20] Cyril Proust and Louis Taillefer
“The Remarkable Underlying Ground States of Cuprate Superconductors”
Annual Review of Condensed Matter Physics **10**, 409 (2019)
- [21] M. R. Norman, D. Pines, and C. Kallin
“The pseudogap: friend or foe of high T_c ?”
Advances in Physics **54**, 715 (2005)
- [22] A. P. Drozdov, M. I. Eremets, I. A. Troyan, V. Ksenofontov, and S. I. Shylin
“Conventional superconductivity at 203 kelvin at high pressures in the sulfur hydride system”
Nature **525**, 73 (2015)
- [23] Maddury Somayazulu, Muhtar Ahart, Ajay K. Mishra, Zachary M. Geballe, Maria Baldini, Yue Meng, Viktor V. Struzhkin, and Russell J. Hemley
“Evidence for Superconductivity above 260 K in Lanthanum Superhydride at Megabar Pressures”
Phys. Rev. Lett. **122**, 027001 (2019)

- [24] A. P. Drozdov, P. P. Kong, V. S. Minkov, S. P. Besedin, M. A. Kuzovnikov, S. Mozaffari, L. Balicas, F. F. Balakirev, D. E. Graf, V. B. Prakapenka, E. Greenberg, D. A. Knyazev, M. Tkacz, and M. I. Eremets
“Superconductivity at 250 K in lanthanum hydride under high pressures”
Nature **569**, 528 (2019)
- [25] F. Steglich, J. Aarts, C. D. Bredl, W. Lieke, D. Meschede, W. Franz, and H. Schäfer
“Superconductivity in the Presence of Strong Pauli Paramagnetism: CeCu_2Si_2 ”
Phys. Rev. Lett. **43**, 1892 (1979)
- [26] Yoichi Kamihara, Takumi Watanabe, Masahiro Hirano, and Hideo Hosono
“Iron-Based Layered Superconductor $\text{La}[\text{O}_{1-x}\text{F}_x]\text{FeAs}$ ($x = 0.05\text{-}0.12$) with $T_c = 26\text{ K}$ ”
Journal of the American Chemical Society **130**, 3296 (2008)
- [27] Z. A. Xu, N. P. Ong, Y. Wang, T. Kakeshita, and S. Uchida
“Vortex-like excitations and the onset of superconducting phase fluctuation in underdoped $\text{La}_{2-x}\text{Sr}_x\text{CuO}_4$ ”
Nature **406**, 486 (2000)
- [28] Anatoly Larkin and Andrei Varlamov
“Theory of Fluctuations in Superconductors”
Oxford University Press (2005)
- [29] H. Xiao, B. Gao, Y. H. Ma, X. J. Li, G. Mu, and T. Hu
“Superconducting fluctuation effect in $\text{CaFe}_{0.88}\text{Co}_{0.12}\text{AsF}$ ”
Journal of Physics: Condensed Matter **28**, 455701 (2016)
- [30] Iddo Ussishkin, S. L. Sondhi, and David A. Huse
“Gaussian Superconducting Fluctuations, Thermal Transport, and the Nernst Effect”
Phys. Rev. Lett. **89**, 287001 (2002)
- [31] M. N. Serbyn, M. A. Skvortsov, A. A. Varlamov, and Victor Galitski
“Giant Nernst Effect due to Fluctuating Cooper Pairs in Superconductors”
Phys. Rev. Lett. **102**, 067001 (2009)
- [32] K. Michaeli and A. M. Finkel’stein
“Fluctuations of the superconducting order parameter as an origin of the Nernst effect”
EPL (Europhysics Letters) **86**, 27007 (2009)
- [33] J. Chang, N. Doiron-Leyraud, O. Cyr-Choiniere, G. Grissonnanche, F. Laliberte, E. Hassinger, J-Ph. Reid, R. Daou, S. Pyon, T. Takayama, H. Takagi, and Louis Taillefer
“Decrease of upper critical field with underdoping in cuprate superconductors”
Nat. Phys. **8**, 751 (2012)
- [34] L. G. Aslamazov and A. I. Larkin
“Effect of Fluctuations on the Properties of a Superconductor Above the Critical Temperature”
Sov. Phys. Solid State **10**, 875 (1968)
- [35] B. O. Kerbikov and M. S. Lukashov
“Fluctuation sound absorption in quark matter”
Modern Physics Letters A **31**, 1650179 (2016)
- [36] Sean A. Hartnoll, Pavel K. Kovtun, Markus Müller, and Subir Sachdev
“Theory of the Nernst effect near quantum phase transitions in condensed matter and in dyonic black holes”
Phys. Rev. B **76**, 144502 (2007)
- [37] V. J. Emery and S. A. Kivelson
“Importance of phase fluctuations in superconductors with small superfluid density”
Nature **374**, 434 (1995)

- [38] Y. J. Uemura, G. M. Luke, B. J. Sternlieb, J. H. Brewer, J. F. Carolan, W. N. Hardy, R. Kadono, J. R. Kempton, R. F. Kiefl, S. R. Kreitzman, P. Mulhern, T. M. Riseman, D. L. Williams, B. X. Yang, S. Uchida, H. Takagi, J. Gopalakrishnan, A. W. Sleight, M. A. Subramanian, C. L. Chien, M. Z. Cieplak, Gang Xiao, V. Y. Lee, B. W. Statt, C. E. Stronach, W. J. Kossler, and X. H. Yu
 “Universal Correlations between T_c and $\frac{n_s}{m^*}$ (Carrier Density over Effective Mass) in High- T_c Cuprate Superconductors”
 Phys. Rev. Lett. **62**, 2317 (1989)
- [39] Masatoshi Sato and Yoichi Ando
 “Topological superconductors: a review”
 Reports on Progress in Physics **80**, 076501 (2017)
- [40] A. Bansil, Hsin Lin, and Tanmoy Das
 “Colloquium: Topological band theory”
 Rev. Mod. Phys. **88**, 021004 (2016)
- [41] Binghai Yan and Claudia Felser
 “Topological Materials: Weyl Semimetals”
 Annual Review of Condensed Matter Physics **8**, 337 (2017)
- [42] Frank Schindler, Ashley M. Cook, Maia G. Vergniory, Zhijun Wang, Stuart S. P. Parkin, B. Andrei Bernevig, and Titus Neupert
 “Higher-order topological insulators”
 Science Advances **4**, eaat0346 (2018)
- [43] Frank Schindler, Zhijun Wang, Maia G. Vergniory, Ashley M. Cook, Anil Murani, Shamashis Sengupta, Alik Yu Kasumov, Richard Deblock, Sangjun Jeon, Ilya Drozdov, Hélène Bouchiat, Sophie Guéron, Ali Yazdani, B. Andrei Bernevig, and Titus Neupert
 “Higher-order topology in bismuth”
 Nature Physics **14**, 918 (2018)
- [44] Hermann Weyl
 “Elektron und Gravitation. I”
 Zeitschrift für Physik **56**, 330 (1929)
- [45] Su-Yang Xu, Ilya Belopolski, Nasser Alidoust, Madhab Neupane, Guang Bian, Chenglong Zhang, Raman Sankar, Guoqing Chang, Zhujun Yuan, Chi-Cheng Lee, Shin-Ming Huang, Hao Zheng, Jie Ma, Daniel S. Sanchez, BaoKai Wang, Arun Bansil, Fangcheng Chou, Pavel P. Shibayev, Hsin Lin, Shuang Jia, and M. Zahid Hasan
 “Discovery of a Weyl fermion semimetal and topological Fermi arcs”
 Science **349**, 613 (2015)
- [46] B. Q. Lv, H. M. Weng, B. B. Fu, X. P. Wang, H. Miao, J. Ma, P. Richard, X. C. Huang, L. X. Zhao, G. F. Chen, Z. Fang, X. Dai, T. Qian, and H. Ding
 “Experimental Discovery of Weyl Semimetal TaAs”
 Phys. Rev. X **5**, 031013 (2015)
- [47] L. X. Yang, Z. K. Liu, Y. Sun, H. Peng, H. F. Yang, T. Zhang, B. Zhou, Y. Zhang, Y. F. Guo, M. Rahn, D. Prabhakaran, Z. Hussain, S.-K. Mo, C. Felser, B. Yan, and Y. L. Chen
 “Weyl semimetal phase in the non-centrosymmetric compound TaAs”
 Nature Physics **11**, 728 (2015)
- [48] Hiroyuki Inoue, András Gyenis, Zhijun Wang, Jian Li, Seong Woo Oh, Shan Jiang, Ni Ni, B. Andrei Bernevig, and Ali Yazdani
 “Quasiparticle interference of the Fermi arcs and surface-bulk connectivity of a Weyl semimetal”
 Science **351**, 1184 (2016)
- [49] Rajib Batabyal, Noam Morali, Nurit Avraham, Yan Sun, Marcus Schmidt, Claudia Felser, Ady Stern, Binghai Yan, and Haim Beidenkopf

- “Visualizing weakly bound surface Fermi arcs and their correspondence to bulk Weyl fermions”
Science Advances **2**, e1600709 (2016)
- [50] Stephen L. Adler
 “Axial-Vector Vertex in Spinor Electrodynamics”
Phys. Rev. **177**, 2426 (1969)
- [51] J. S. Bell and R. Jackiw
 “A PCAC puzzle: $\pi^0 \rightarrow \gamma\gamma$ in the σ -model”
Il Nuovo Cimento A **60**, 47 (1969)
- [52] A. A. Burkov
 “Chiral anomaly and transport in Weyl metals”
Journal of Physics: Condensed Matter **27**, 113201 (2015)
- [53] Cheng-Long Zhang, Su-Yang Xu, Ilya Belopolski, Zhujun Yuan, Ziquan Lin, Bingbing Tong, Guang Bian, Nasser Alidoust, Chi-Cheng Lee, Shin-Ming Huang, Tay-Rong Chang, Guoqing Chang, Chuang-Han Hsu, Horng-Tay Jeng, Madhab Neupane, Daniel S. Sanchez, Hao Zheng, Junfeng Wang, Hsin Lin, Chi Zhang, Hai-Zhou Lu, Shun-Qing Shen, Titus Neupert, M. Zahid Hasan, and Shuang Jia
 “Signatures of the Adler-Bell-Jackiw chiral anomaly in a Weyl fermion semimetal”
Nature Communications **7**, 10735 (2016)
- [54] R. D. dos Reis, M. O. Ajeesh, N. Kumar, F. Arnold, C. Shekhar, M. Naumann, M. Schmidt, M. Nicklas, and E. Hassinger
 “On the search for the chiral anomaly in Weyl semimetals: the negative longitudinal magnetoresistance”
New Journal of Physics **18**, 085006 (2016)
- [55] Alexey A. Soluyanov, Dominik Gresch, Zhijun Wang, QuanSheng Wu, Matthias Troyer, Xi Dai, and B. Andrei Bernevig
 “Type-II Weyl semimetals”
Nature **527**, 495 (2015)
- [56] V. L. Berezinskii
 “Destruction of Long-range Order in One-dimensional and Two-dimensional Systems having a Continuous Symmetry Group I. Classical Systems”
Journal of Experimental and Theoretical Physics **32**, 493 (1971)
- [57] V. L. Berezinskii
 “Destruction of Long-range Order in One-dimensional and Two-dimensional Systems Possessing a Continuous Symmetry Group. II. Quantum Systems”
Journal of Experimental and Theoretical Physics **34**, 610 (1972)
- [58] J. M. Kosterlitz and D. J. Thouless
 “Long range order and metastability in two dimensional solids and superfluids. (Application of dislocation theory)”
Journal of Physics C: Solid State Physics **5**, L124 (1972)
- [59] J. M. Kosterlitz and D. J. Thouless
 “Ordering, metastability and phase transitions in two-dimensional systems”
Journal of Physics C: Solid State Physics **6**, 1181 (1973)
- [60] Zoran Hadzibabic, Peter Krüger, Marc Cheneau, Baptiste Battelier, and Jean Dalibard
 “Berezinskii-Kosterlitz-Thouless crossover in a trapped atomic gas”
Nature **441**, 1118 (2006)
- [61] D. J. Resnick, J. C. Garland, J. T. Boyd, S. Shoemaker, and R. S. Newrock
 “Kosterlitz-Thouless Transition in Proximity-Coupled Superconducting Arrays”
Phys. Rev. Lett. **47**, 1542 (1981)

- [62] N. Reyren, S. Thiel, A. D. Caviglia, L. Fitting. Kourkoutis, G. Hammerl, C. Richter, C. W. Schneider, T. Kopp, A.-S. Rüetschi, D. Jaccard, M. Gabay, D. A. Muller, J.-M. Triscone, and J. Mannhart
“Superconducting Interfaces Between Insulating Oxides”
Science **317**, 1196 (2007)
- [63] A. D. Caviglia, S. Gariglio, N. Reyren, D. Jaccard, T. Schneider, M. Gabay, S. Thiel, G. Hammerl, J. Mannhart, and J.-M. Triscone
“Electric field control of the $\text{LaAlO}_3/\text{SrTiO}_3$ interface ground state”
Nature **456**, 624 (2008)
- [64] J. T. Ye, S. Inoue, K. Kobayashi, Y. Kasahara, H. T. Yuan, H. Shimotani, and Y. Iwasa
“Liquid-gated interface superconductivity on an atomically flat film”
Nature Materials **9**, 125 (2009)
- [65] Alexey Yu Mironov, Daniel M. Silevitch, Thomas Proslie, Svetlana V. Postolova, Maria V. Burdastyh, Anton K. Gutakovskii, Thomas F. Rosenbaum, Valerii V. Vinokur, and Tatyana I. Baturina
“Charge Berezinskii-Kosterlitz-Thouless transition in superconducting NbTiN films”
Scientific Reports **8**, 4082 (2018)
- [66] P. Drude
“Zur Elektronentheorie der Metalle; I. Teil.”
Annalen der Physik **306**, 566 (1900)
- [67] P. Drude
“Zur Elektronentheorie der Metalle; II. Teil. Galvanomagnetische und thermomagnetische Effecte”
Annalen der Physik **308**, 369 (1900)
- [68] P. Drude
“Zur Elektronentheorie der Metalle; Berichtigung”
Annalen der Physik **312**, 687 (1902)
- [69] J. J. Thomson
“Cathode Rays”
The Electrician **39**, 104 (1897)
- [70] J. J. Thomson
“Cathode Rays”
Philosophical Magazine **44**, 293 (1897)
- [71] H. A. Lorentz
“The motion of electrons in metallic bodies I”
KNAW Proceedings **7**, 438 (1905)
- [72] H. A. Lorentz
“The motion of electrons in metallic bodies II”
KNAW Proceedings **7**, 585 (1905)
- [73] H. A. Lorentz
“The motion of electrons in metallic bodies III”
KNAW Proceedings **7**, 684 (1905)
- [74] Rudolf Gross and Achim Marx
“Festkörperphysik”, 2nd ed.
de Gruyter (2014)
- [75] A. Sommerfeld
“Zur Elektronentheorie der Metalle”
Naturwissenschaften **15**, 825 (1927)

- [76] A. Sommerfeld
 “Zur Elektronentheorie der Metalle auf Grund der Fermischen Statistik”
 Zeitschrift für Physik **47**, 1 (1928)
- [77] A. Sommerfeld
 “Zur Elektronentheorie der Metalle auf Grund der Fermischen Statistik”
 Zeitschrift für Physik **47**, 43 (1928)
- [78] E. H. Hall
 “On a New Action of the Magnet on Electric Currents”
 American Journal of Mathematics **2**, 287 (1879)
- [79] Naoto Nagaosa, Jairo Sinova, Shigeki Onoda, A. H. MacDonald, and N. P. Ong
 “Anomalous Hall effect”
 Rev. Mod. Phys. **82**, 1539 (2010)
- [80] E. H. Hall
 “XVIII. On the “Rotational Coefficient” in nickel and cobalt”
 The London, Edinburgh, and Dublin Philosophical Magazine and Journal of Science **12**,
 157 (1881)
- [81] Michael Victor Berry
 “Quantal phase factors accompanying adiabatic changes”
 Proceedings of the Royal Society of London. A. Mathematical and Physical Sciences **392**,
 45 (1984)
- [82] Robert Karplus and J. M. Luttinger
 “Hall Effect in Ferromagnetics”
 Phys. Rev. **95**, 1154 (1954)
- [83] Albert von Ettingshausen and Walther Nernst
 “Ueber das Auftreten electromotorischer Kräfte in Metallplatten, welche von einem
 Wärmestrome durchflossen werden und sich im magnetischen Felde befinden”
 Annalen der Physik **265**, 343 (1886)
- [84] Thomas Johann Seebeck
 “Magnetische Polarisation der Metalle und Erze durch Temperatur-Differenz”
 Abhandlungen der Königlichen Akademie der Wissenschaften zu Berlin, 265 (1822)
- [85] Kamran Behnia
 “The Nernst effect and the boundaries of the Fermi liquid picture”
 Journal of Physics: Condensed Matter **21**, 113101 (2009)
- [86] Kamran Behnia and Herve Aubin
 “Nernst effect in metals and superconductors: a review of concepts and experiments”
 Reports on Progress in Physics **79**, 046502 (2016)
- [87] Kamran Behnia
 “Fundamentals of Thermoelectricity”
 Oxford University Press (2015)
- [88] R. C. Jaklevic, John Lambe, A. H. Silver, and J. E. Mercereau
 “Quantum Interference Effects in Josephson Tunneling”
 Phys. Rev. Lett. **12**, 159 (1964)
- [89] M. Sawicki, W. Stefanowicz, and A. Ney
 “Sensitive SQUID magnetometry for studying nanomagnetism”
 Semiconductor Science and Technology **26**, 064006 (2011)
- [90] B. D. Josephson
 “Possible new effects in superconductive tunnelling”
 Physics Letters **1**, 251 (1962)

- [91] P. W. Anderson and J. M. Rowell
“Probable Observation of the Josephson Superconducting Tunneling Effect”
Phys. Rev. Lett. **10**, 230 (1963)
- [92] Fausto Fiorillo
“DC and AC magnetization processes in soft magnetic materials”
Journal of Magnetism and Magnetic Materials **242-245**, 77 (2002)
- [93] W. Friedrich, P. Knipping, and M. Laue
“Interferenz-Erscheinungen bei Röntgenstrahlen”
Sitzungsberichte der mathematisch-physikalischen Klasse der Königlich-Bayerischen Akademie der Wissenschaften zu München, 303 (1912)
- [94] P. Marra, A. Nigro, Z. Li, G. F. Chen, N. L. Wang, J. L. Luo, and C. Noce
“Paraconductivity of the K-doped SrFe₂As₂ superconductor”
New Journal of Physics **14**, 043001 (2012)
- [95] Kazumi Maki
“The Critical Fluctuation of the Order Parameter in Type-II Superconductors”
Progress of Theoretical Physics **39**, 897 (1968)
- [96] Richard S. Thompson
“Microwave, Flux Flow, and Fluctuation Resistance of Dirty Type-II Superconductors”
Phys. Rev. B **1**, 327 (1970)
- [97] S. Hikami and A.I. Larkin
“Magnetoresistance of high temperature superconductors”
Modern Physics Letters B **02**, 693 (1988)
- [98] W. Lang, G. Heine, P. Schwab, X. Z. Wang, and D. Bäuerle
“Paraconductivity and excess Hall effect in epitaxial YBa₂Cu₃O₇ films induced by superconducting fluctuations”
Phys. Rev. B **49**, 4209 (1994)
- [99] B. I. Halperin and David R. Nelson
“Resistive transition in superconducting films”
Journal of Low Temperature Physics **36**, 599 (1979)
- [100] Mintu Mondal, Sanjeev Kumar, Madhavi Chand, Anand Kamlapure, Garima Saraswat, G. Seibold, L. Benfatto, and Pratap Raychaudhuri
“Role of the Vortex-Core Energy on the Berezinskii-Kosterlitz-Thouless Transition in Thin Films of NbN”
Phys. Rev. Lett. **107**, 217003 (2011)
- [101] Vsevolod F. Gantmakher and Valery T. Dolgoplov
“Superconductor–insulator quantum phase transition”
Physics-Uspekhi **53**, 1 (2010)
- [102] Mohit Randeria
“Ultracold Fermi gases: Pre-pairing for condensation”
Nat. Phys. **6**, 561 (2010)
- [103] S. Kasahara, T. Yamashita, A. Shi, R. Kobayashi, Y. Shimoyama, T. Watashige, K. Ishida, T. Terashima, T. Wolf, F. Hardy, C. Meingast, H. v. Löhneysen, A. Levchenko, T. Shibauchi, and Y. Matsuda
“Giant superconducting fluctuations in the compensated semimetal FeSe at the BCS-BEC crossover”
Nature Communications **7**, 12843 (2016)
- [104] Vadim M. Loktev, Rachel M. Quick, and Sergei G. Sharapov
“Phase fluctuations and pseudogap phenomena”
Physics Reports **349**, 1 (2001)

- [105] Yayu Wang, Lu Li, and N. P. Ong
“Nernst effect in high- T_c superconductors”
Phys. Rev. B **73**, 024510 (2006)
- [106] Lu Li, Yayu Wang, Seiki Komiya, Shimpei Ono, Yoichi Ando, G. D. Gu, and N. P. Ong
“Diamagnetism and Cooper pairing above T_c in cuprates”
Phys. Rev. B **81**, 054510 (2010)
- [107] P. G. Baity, Xiaoyan Shi, Zhenzhong Shi, L. Benfatto, and Dragana Popović
“Effective two-dimensional thickness for the Berezinskii-Kosterlitz-Thouless-like transition in a highly underdoped $\text{La}_{2-x}\text{Sr}_x\text{CuO}_4$ ”
Phys. Rev. B **93**, 024519 (2016)
- [108] A. Pourret, H. Aubin, J. Lesueur, C. A. Marrache-Kikuchi, L. Berge, L. Dumoulin, and K. Behnia
“Observation of the Nernst signal generated by fluctuating Cooper pairs”
Nat. Phys. **2**, 683 (2006)
- [109] F. Rullier-Albenque, H. Alloul, and G. Rikken
“High-field studies of superconducting fluctuations in high- T_c cuprates: Evidence for a small gap distinct from the large pseudogap”
Phys. Rev. B **84**, 014522 (2011)
- [110] B. Leridon, J. Vanacken, T. Wambeq, and V. V. Moshchalkov
“Paraconductivity of underdoped $\text{La}_{2-x}\text{Sr}_x\text{CuO}_4$ thin-film superconductors using high magnetic fields”
Phys. Rev. B **76**, 012503 (2007)
- [111] L. Perfetti, B. Scioffa, G. Biroli, C. J. van der Beek, C. Piovera, M. Wolf, and T. Kampfrath
“Ultrafast Dynamics of Fluctuations in High-Temperature Superconductors Far from Equilibrium”
Phys. Rev. Lett. **114**, 067003 (2015)
- [112] Yayu Wang, Lu Li, M. J. Naughton, G. D. Gu, S. Uchida, and N. P. Ong
“Field-Enhanced Diamagnetism in the Pseudogap State of the Cuprate $\text{Bi}_2\text{Sr}_2\text{CaCu}_2\text{O}_{8+\delta}$ Superconductor in an Intense Magnetic Field”
Phys. Rev. Lett. **95**, 247002 (2005)
- [113] N. P. Ong, Yayu Wang, Lu Li, and M. J. Naughton
“Ong et al. Reply:”
Phys. Rev. Lett. **98**, 119702 (2007)
- [114] Lucía Cabo, Jesús Mosqueira, and Félix Vidal
“Comment on “Field-Enhanced Diamagnetism in the Pseudogap State of the Cuprate $\text{Bi}_2\text{Sr}_2\text{CaCu}_2\text{O}_{8+\delta}$ Superconductor in an Intense Magnetic Field””
Phys. Rev. Lett. **98**, 119701 (2007)
- [115] Iulian Hetel, Thomas R. Lemberger, and Mohit Randeria
“Quantum critical behaviour in the superfluid density of strongly underdoped ultrathin copper oxide films”
Nature Physics **3**, 700 (2007)
- [116] Marcel Franz
“Importance of fluctuations”
Nature Physics **3**, 686 (2007)
- [117] Madhavi Chand, Garima Saraswat, Anand Kamlapure, Mintu Mondal, Sanjeev Kumar, John Jesudasan, Vivas Bagwe, Lara Benfatto, Vikram Tripathi, and Pratap Raychaudhuri
“Phase diagram of the strongly disordered s -wave superconductor NbN close to the metal-insulator transition”
Phys. Rev. B **85**, 014508 (2012)

- [118] Mintu Mondal, Anand Kamlapure, Madhavi Chand, Garima Saraswat, Sanjeev Kumar, John Jesudasan, L. Benfatto, Vikram Tripathi, and Pratap Raychaudhuri
“Phase Fluctuations in a Strongly Disordered *s*-Wave NbN Superconductor Close to the Metal-Insulator Transition”
Phys. Rev. Lett. **106**, 047001 (2011)
- [119] Benjamin Sacépé, Claude Chapelier, Tatyana I. Baturina, Valerii M. Vinokur, Mikhail R. Baklanov, and Marc Sanquer
“Pseudogap in a thin film of a conventional superconductor”
Nature Communications **1**, 140 (2010)
- [120] Benjamin Sacépé, Thomas Dubouchet, Claude Chapelier, Marc Sanquer, Maoz Ovadia, Dan Shahar, Mikhail Feigel’man, and Lev Ioffe
“Localization of preformed Cooper pairs in disordered superconductors”
Nature Physics **7**, 239 (2011)
- [121] Nicholas P. Breznay, Karen Michaeli, Konstantin S. Tikhonov, Alexander M. Finkel’stein, Mihir Tendulkar, and Aharon Kapitulnik
“Hall conductivity dominated by fluctuations near the superconducting transition in disordered thin films”
Phys. Rev. B **86**, 014514 (2012)
- [122] Nicholas P. Breznay and Aharon Kapitulnik
“Observation of the ghost critical field for superconducting fluctuations in a disordered TaN thin film”
Phys. Rev. B **88**, 104510 (2013)
- [123] Kazumasa Makise, Fusao Ichikawa, Takayuki Asano, and Bunju Shinozaki
“Field-tuned superconductor–insulator transitions and Hall resistance in thin polycrystalline MoN films”
Journal of Physics: Condensed Matter **30**, 065402 (2018)
- [124] Karen Michaeli, Konstantin S. Tikhonov, and Alexander M. Finkel’stein
“Hall effect in superconducting films”
Phys. Rev. B **86**, 014515 (2012)
- [125] R. Romestain, B. Delaet, P. Renaud-Goud, I. Wang, C. Jorel, J.-C. Villegier, and J.-Ph. Poizat
“Fabrication of a superconducting niobium nitride hot electron bolometer for single-photon counting”
New Journal of Physics **6**, 129 (2004)
- [126] Ivan Tretyakov, Sergey Ryabchun, Matvey Finkel, Anna Maslennikova, Natalia Kaurova, Anastasia Lobastova, Boris Voronov, and Gregory Gol’tsman
“Low noise and wide bandwidth of NbN hot-electron bolometer mixers”
Applied Physics Letters **98**, 033507 (2011)
- [127] G. N. Gol’tsman, O. Okunev, G. Chulkova, A. Lipatov, A. Semenov, K. Smirnov, B. Voronov, A. Dzardanov, C. Williams, and Roman Sobolewski
“Picosecond superconducting single-photon optical detector”
Applied Physics Letters **79**, 705 (2001)
- [128] Chandra M. Natarajan, Michael G. Tanner, and Robert H. Hadfield
“Superconducting nanowire single-photon detectors: physics and applications”
Superconductor Science and Technology **25**, 063001 (2012)
- [129] M. S. Wong, W. D. Sproul, X. Chu, and S. A. Barnett
“Reactive magnetron sputter deposition of niobium nitride films”
Journal of Vacuum Science & Technology A **11**, 1528 (1993)
- [130] D. Hazra, N. Tsavdaris, S. Jebari, A. Grimm, F. Blanchet, F. Mercier, E. Blanquet, C. Chapelier, and M. Hofheinz

- “Superconducting properties of very high quality NbN thin films grown by high temperature chemical vapor deposition”
Superconductor Science and Technology **29**, 105011 (2016)
- [131] Tomas Polakovic, Sergi Lendinez, John E. Pearson, Axel Hoffmann, Volodymyr Yefremenko, Clarence L. Chang, Whitney Armstrong, Kawtar Hafidi, Goran Karapetrov, and Valentine Novosad
 “Room temperature deposition of superconducting niobium nitride films by ion beam assisted sputtering”
APL Materials **6**, 076107 (2018)
- [132] Randolph E. Treece, James S. Horwitz, John H. Claassen, and Douglas B. Chrisey
 “Pulsed laser deposition of high-quality NbN thin films”
Applied Physics Letters **65**, 2860 (1994)
- [133] Garima Saraswat, Priti Gupta, Arnab Bhattacharya, and Pratap Raychaudhuri
 “Highly oriented, free-standing, superconducting NbN films growth on chemical vapor deposited graphene”
APL Materials **2**, 056103 (2014)
- [134] S. P. Chockalingam, Madhavi Chand, John Jesudasan, Vikram Tripathi, and Pratap Raychaudhuri
 “Superconducting properties and Hall effect of epitaxial NbN thin films”
Phys. Rev. B **77**, 214503 (2008)
- [135] Madhavi Chand, Archana Mishra, Y. M. Xiong, Anand Kamlapure, S. P. Chockalingam, John Jesudasan, Vivas Bagwe, Mintu Mondal, P. W. Adams, Vikram Tripathi, and Pratap Raychaudhuri
 “Temperature dependence of resistivity and Hall coefficient in strongly disordered NbN thin films”
Phys. Rev. B **80**, 134514 (2009)
- [136] A. Semenov, B. Günther, U. Böttger, H.-W. Hübers, H. Bartolf, A. Engel, A. Schilling, K. Ilin, M. Siegel, R. Schneider, D. Gerthsen, and N. A. Gippius
 “Optical and transport properties of ultrathin NbN films and nanostructures”
Phys. Rev. B **80**, 054510 (2009)
- [137] M. Beck, M. Klammer, S. Lang, P. Leiderer, V. V. Kabanov, G. N. Gol’tsman, and J. Demsar
 “Energy-Gap Dynamics of Superconducting NbN Thin Films Studied by Time-Resolved Terahertz Spectroscopy”
Phys. Rev. Lett. **107**, 177007 (2011)
- [138] Ryusuke Matsunaga and Ryo Shimano
 “Nonequilibrium BCS State Dynamics Induced by Intense Terahertz Pulses in a Superconducting NbN Film”
Phys. Rev. Lett. **109**, 187002 (2012)
- [139] M. Beck, I. Rousseau, M. Klammer, P. Leiderer, M. Mittendorff, S. Winnerl, M. Helm, G. N. Gol’tsman, and J. Demsar
 “Transient Increase of the Energy Gap of Superconducting NbN Thin Films Excited by Resonant Narrow-Band Terahertz Pulses”
Phys. Rev. Lett. **110**, 267003 (2013)
- [140] Ryusuke Matsunaga, Naoto Tsuji, Hiroyuki Fujita, Arata Sugioka, Kazumasa Makise, Yoshinori Uzawa, Hirotaka Terai, Zhen Wang, Hideo Aoki, and Ryo Shimano
 “Light-induced collective pseudospin precession resonating with Higgs mode in a superconductor”
Science **345**, 1145 (2014)

- [141] A. G. Aronov, S. Hikami, and A. I. Larkin
 “Gauge invariance and transport properties in superconductors above T_c ”
 Phys. Rev. B **51**, 3880 (1995)
- [142] N. R. Werthamer, E. Helfand, and P. C. Hohenberg
 “Temperature and Purity Dependence of the Superconducting Critical Field, H_{c2} . III. Electron Spin and Spin-Orbit Effects”
 Phys. Rev. **147**, 295 (1966)
- [143] Mitsumasa Suzuki, Masahiro Baba, and Takeshi Anayama
 “Critical Magnetic Fields of Superconducting NbN Films Prepared by Reactive Sputtering”
 Japanese Journal of Applied Physics **26**, 947 (1987)
- [144] Mintu Mondal, Madhavi Chand, Anand Kamlapure, John Jesudasan, Vivas C. Bagwe, Sanjeev Kumar, Garima Saraswat, Vikram Tripathi, and Pratap Raychaudhuri
 “Phase Diagram and Upper Critical Field of Homogeneously Disordered Epitaxial 3-Dimensional NbN Films”
 Journal of Superconductivity and Novel Magnetism **24**, 341 (2011)
- [145] Charles Kittel
 “Einführung in die Festkörperphysik”, 14th ed.
 Oldenbourg Wissenschaftsverlag GmbH (2006)
- [146] W. L. McMillan
 “Transition Temperature of Strong-Coupled Superconductors”
 Phys. Rev. **167**, 331 (1968)
- [147] P. Roedhammer, E. Gmelin, W. Weber, and J. P. Remeika
 “Observation of phonon anomalies in NbC_xN_{1-x} alloys”
 Phys. Rev. B **15**, 711 (1977)
- [148] A. Larkin
 “Superconductor-insulator transitions in films and bulk materials”
 Annalen der Physik **8**, 785 (1999)
- [149] A.I. Larkin and Yu.N. Ovchinnikov
 “Nonlinear fluctuation phenomena in the transport properties of superconductors”
 Zhurnal Eksperimentalnoi i Teoreticheskoi Fiziki **119**, 595 (2001)
- [150] Junyi Ge, Shixun Cao, Shujuan Yuan, Baojuan Kang, and Jincang Zhang
 “Three-dimensional superconductivity in nominal composition Fe_{1.03}Se with T_c^{zero} up to 10.9 K induced by internal strain”
 Journal of Applied Physics **108**, 053903 (2010)
- [151] R. I. Rey, A. Ramos-Álvarez, C. Carballeira, J. Mosqueira, F. Vidal, S. Salem-Sugui, A. D. Alvarenga, Rui Zhang, and Huiqian Luo
 “Measurements of the superconducting fluctuations in optimally doped BaFe_{2-x}Ni_xAs₂ under high magnetic fields: probing the 3D-anisotropic Ginzburg–Landau approach”
 Superconductor Science and Technology **27**, 075001 (2014)
- [152] Hidetoshi Fukuyama, Hiromichi Ebisawa, and Toshio Tsuzuki
 “Fluctuation of the Order Parameter and Hall Effect”
 Progress of Theoretical Physics **46**, 1028 (1971)
- [153] Konstantin S. Tikhonov, Georg Schwiete, and Alexander M. Finkel’stein
 “Fluctuation conductivity in disordered superconducting films”
 Phys. Rev. B **85**, 174527 (2012)
- [154] F. F. Tafti, F. Laliberté, M. Dion, J. Gaudet, P. Fournier, and Louis Taillefer
 “Nernst effect in the electron-doped cuprate superconductor Pr_{2-x}Ce_xCuO₄: Superconducting fluctuations, upper critical field H_{c2} , and the origin of the T_c dome”
 Phys. Rev. B **90**, 024519 (2014)

- [155] A. Pourret, H. Aubin, J. Lesueur, C. A. Marrache-Kikuchi, L. Bergé, L. Dumoulin, and K. Behnia
 “Length scale for the superconducting Nernst signal above T_c in $\text{Nb}_{0.15}\text{Si}_{0.85}$ ”
 Phys. Rev. B **76**, 214504 (2007)
- [156] A. Pourret, P. Spathis, H. Aubin, and K. Behnia
 “Nernst effect as a probe of superconducting fluctuations in disordered thin films”
 New Journal of Physics **11**, 055071 (2009)
- [157] P. R. Mandal, Tarapada Sarkar, J. S. Higgins, and Richard L. Greene
 “Nernst effect in the electron-doped cuprate superconductor $\text{La}_{2-x}\text{Ce}_x\text{CuO}_4$ ”
 Phys. Rev. B **97**, 014522 (2018)
- [158] Hervé Aubin and Kamran Behnia
 “Nernst effect studies of Cooper pair fluctuations”
 Physica C: Superconductivity and its Applications **552**, 38 (2018)
- [159] Indranil Roy, Rini Ganguly, Harkirat Singh, and Pratap Raychaudhuri
 “Robust pseudogap across the magnetic field driven superconductor to insulator-like transition in strongly disordered NbN films”
 The European Physical Journal B **92**, 49 (2019)
- [160] Igor Poboiko and Mikhail Feigel'man
 “Paraconductivity of pseudogapped superconductors”
 Phys. Rev. B **97**, 014506 (2018)
- [161] R. Koushik, Siddhartha Kumar, Kazi Rafsanjani. Amin, Mintu Mondal, John Jesudasan, Aveek Bid, Pratap Raychaudhuri, and Arindam Ghosh
 “Correlated Conductance Fluctuations Close to the Berezinskii-Kosterlitz-Thouless Transition in Ultrathin NbN Films”
 Phys. Rev. Lett. **111**, 197001 (2013)
- [162] C. Carbillet, S. Caprara, M. Grilli, C. Brun, T. Cren, F. Debontridder, B. Vignolle, W. Tabis, D. Demaille, L. Largeau, K. Ilin, M. Siegel, D. Roditchev, and B. Leridon
 “Confinement of superconducting fluctuations due to emergent electronic inhomogeneities”
 Phys. Rev. B **93**, 144509 (2016)
- [163] Y. Noat, V. Cherkez, C. Brun, T. Cren, C. Carbillet, F. Debontridder, K. Ilin, M. Siegel, A. Semenov, H.-W. Hübers, and D. Roditchev
 “Unconventional superconductivity in ultrathin superconducting NbN films studied by scanning tunneling spectroscopy”
 Phys. Rev. B **88**, 014503 (2013)
- [164] H. Bartolf, A. Engel, A. Schilling, K. Il'in, M. Siegel, H.-W. Hübers, and A. Semenov
 “Current-assisted thermally activated flux liberation in ultrathin nanopatterned NbN superconducting meander structures”
 Phys. Rev. B **81**, 024502 (2010)
- [165] V. A. Gasparov
 “Berezinskii-Kosterlitz-Thouless transition and fluctuation paraconductivity in $\text{Y}_1\text{Ba}_2\text{Cu}_3\text{O}_7$ single crystal films”
 Physica C: Superconductivity **178**, 449 (1991)
- [166] Q. Li, M. Hücker, G. D. Gu, A. M. Tsvelik, and J. M. Tranquada
 “Two-Dimensional Superconducting Fluctuations in Stripe-Ordered $\text{La}_{1.875}\text{Ba}_{0.125}\text{CuO}_4$ ”
 Phys. Rev. Lett. **99**, 067001 (2007)
- [167] Rufus Boyack, Xiaoyu Wang, Qijin Chen, and K. Levin
 “Combined effects of pairing fluctuations and a pseudogap in the cuprate Hall coefficient”
 Phys. Rev. B **99**, 134504 (2019)

- [168] F. Laliberté, W. Tabis, S. Badoux, B. Vignolle, D. Destraz, N. Momono, T. Kurosawa, K. Yamada, H. Takagi, N. Doiron-Leyraud, C. Proust, and Louis Taillefer
“Origin of the metal-to-insulator crossover in cuprate superconductors”
arXiv e-prints, arXiv:1606.04491 (2016)
- [169] S. Badoux, W. Tabis, F. Laliberté, G. Grissonnanche, B. Vignolle, D. Vignolles, J. Béard, D. A. Bonn, W. N. Hardy, R. Liang, N. Doiron-Leyraud, Louis Taillefer, and Cyril Proust
“Change of carrier density at the pseudogap critical point of a cuprate superconductor”
Nature **531**, 210 (2016)
- [170] G. Grissonnanche, A. Legros, S. Badoux, E. Lefrançois, V. Zatzko, M. Lizaire, F. Laliberté, A. Gourgout, J.-S. Zhou, S. Pyon, T. Takayama, H. Takagi, S. Ono, N. Doiron-Leyraud, and L. Taillefer
“Giant thermal Hall conductivity in the pseudogap phase of cuprate superconductors”
Nature **571**, 376 (2019)
- [171] H. G. Luo, Y. H. Su, and T. Xiang
“Scaling analysis of normal-state properties of high-temperature superconductors”
Phys. Rev. B **77**, 014529 (2008)
- [172] C. Meingast, V. Pasler, P. Nagel, A. Rykov, S. Tajima, and P. Olsson
“Phase Fluctuations and the Pseudogap in $\text{YBa}_2\text{Cu}_3\text{O}_x$ ”
Phys. Rev. Lett. **86**, 1606 (2001)
- [173] J. M. Harris, N. P. Ong, P. Matl, R. Gagnon, L. Taillefer, T. Kimura, and K. Kitazawa
“Additive quasiparticle and vortex Hall conductivities in $\text{La}_{2-x}\text{Sr}_x\text{CuO}_4$ and untwinned $\text{YBa}_2\text{Cu}_3\text{O}_{6.93}$ ”
Phys. Rev. B **51**, 12053 (1995)
- [174] Z. D. Wang, Jinming Dong, and C. S. Ting
“Unified theory of mixed state Hall effect in type-II superconductors: Scaling behavior and sign reversal”
Phys. Rev. Lett. **72**, 3875 (1994)
- [175] Y. Shiomi, N. Kanazawa, K. Shibata, Y. Onose, and Y. Tokura
“Topological Nernst effect in a three-dimensional skyrmion-lattice phase”
Phys. Rev. B **88**, 064409 (2013)
- [176] S. J. Hagen, C. J. Lobb, R. L. Greene, M. G. Forrester, and J. H. Kang
“Anomalous Hall effect in superconductors near their critical temperatures”
Phys. Rev. B **41**, 11630 (1990)
- [177] R. Jin and H. R. Ott
“Hall effect of $\text{YBa}_2\text{Cu}_3\text{O}_{7-\delta}$ single crystals”
Phys. Rev. B **57**, 13872 (1998)
- [178] A. M. Goldman
“Superconductor-insulator transitions”
International Journal of Modern Physics B **24**, 4081 (2010)
- [179] Kazumasa Makise, Hirotaka Terai, Yukihiro Tominari, Shukichi Tanaka, and Bunju Shinozaki
“Duality picture of Superconductor-insulator transitions on Superconducting nanowire”
Scientific Reports **6**, 27001 (2016)
- [180] A. F. Hebard and M. A. Paalanen
“Magnetic-field-tuned superconductor-insulator transition in two-dimensional films”
Phys. Rev. Lett. **65**, 927 (1990)
- [181] M. A. Paalanen, A. F. Hebard, and R. R. Ruel
“Low-temperature insulating phases of uniformly disordered two-dimensional superconductors”
Phys. Rev. Lett. **69**, 1604 (1992)

- [182] Ali Yazdani and Aharon Kapitulnik
“Superconducting-Insulating Transition in Two-Dimensional a -MoGe Thin Films”
Phys. Rev. Lett. **74**, 3037 (1995)
- [183] Philip Phillips, Yi Wan, Ivar Martin, Sergey Knysh, and Denis Dalidovich
“Superconductivity in a two-dimensional electron gas”
Nature **395**, 253 (1998)
- [184] Xiaofu Zhang and Andreas Schilling
“Sequential superconductor–Bose insulator–Fermi insulator phase transitions in quasi-two-dimensional α -WSi”
Phys. Rev. B **97**, 214524 (2018)
- [185] Vsevolod F. Gantmakher and Valery T. Dolgoplov
“Superconductor–insulator quantum phase transition”
Physics-Uspekhi **53**, 1 (2010)
- [186] A. M. Goldman
“Superconductor–insulator transitions in the two-dimensional limit”
Physica E: Low-dimensional Systems and Nanostructures **18**, 1 (2003)
- [187] Nicholas P. Breznay, Mihir Tendulkar, Li Zhang, Sang-Chul Lee, and Aharon Kapitulnik
“Superconductor to weak-insulator transitions in disordered tantalum nitride films”
Phys. Rev. B **96**, 134522 (2017)
- [188] A. Roy, E. Shimshoni, and A. Frydman
“Quantum Criticality at the Superconductor-Insulator Transition Probed by the Nernst Effect”
Phys. Rev. Lett. **121**, 047003 (2018)
- [189] Ying Xing, Hui-Min Zhang, Hai-Long Fu, Haiwen Liu, Yi Sun, Jun-Ping Peng, Fa Wang, Xi Lin, Xu-Cun Ma, Qi-Kun Xue, Jian Wang, and X. C. Xie
“Quantum Griffiths singularity of superconductor-metal transition in Ga thin films”
Science **350**, 542 (2015)
- [190] Shengchun Shen, Ying Xing, Pengjie Wang, Haiwen Liu, Hailong Fu, Yangwei Zhang, Lin He, X. C. Xie, Xi Lin, Jiakai Nie, and Jian Wang
“Observation of quantum Griffiths singularity and ferromagnetism at the superconducting LaAlO₃/SrTiO₃(110) interface”
Phys. Rev. B **94**, 144517 (2016)
- [191] Zhuoyu Chen, Adrian G. Swartz, Hyeok Yoon, Hisashi Inoue, Tyler A. Merz, Di Lu, Yanwu Xie, Hongtao Yuan, Yasuyuki Hikita, Srinivas Raghu, and Harold Y. Hwang
“Carrier density and disorder tuned superconductor-metal transition in a two-dimensional electron system”
Nature Communications **9**, 4008 (2018)
- [192] Yu Saito, Tsutomu Nojima, and Yoshihiro Iwasa
“Quantum phase transitions in highly crystalline two-dimensional superconductors”
Nature Communications **9**, 778 (2018)
- [193] Enze Zhang, Jinhua Zhi, Yi-Chao Zou, Zefang Ye, Linfeng Ai, Jiacheng Shi, Ce Huang, Shanshan Liu, Zehao Lin, Xinyuan Zheng, Ning Kang, Hongqi Xu, Wei Wang, Liang He, Jin Zou, Jinyu Liu, Zhiqiang Mao, and Faxian Xiu
“Signature of quantum Griffiths singularity state in a layered quasi-one-dimensional superconductor”
Nature Communications **9**, 4656 (2018)
- [194] Thomas Vojta
“Quantum Griffiths Effects and Smeared Phase Transitions in Metals: Theory and Experiment”
Journal of Low Temperature Physics **161**, 299 (2010)

- [195] Nicholas P. Breznay, Myles A. Steiner, Steven Allan Kivelson, and Aharon Kapitulnik
 “Self-duality and a Hall-insulator phase near the superconductor-to-insulator transition in indium-oxide films”
 Proceedings of the National Academy of Sciences, 201522435 (2015)
- [196] Nicholas P. Breznay and Aharon Kapitulnik
 “Particle-hole symmetry reveals failed superconductivity in the metallic phase of two-dimensional superconducting films”
 Science Advances **3**, e1700612 (2017)
- [197] S. N. Ruddlesden and P. Popper
 “New compounds of the K_2NiF_4 type”
 Acta Crystallographica **10**, 538 (1957)
- [198] S. N. Ruddlesden and P. Popper
 “The compound $Sr_3Ti_2O_7$ and its structure”
 Acta Crystallographica **11**, 54 (1958)
- [199] Chris Ablitt, Arash A. Mostofi, Nicholas C. Bristowe, and Mark S. Senn
 “Control of Uniaxial Negative Thermal Expansion in Layered Perovskites by Tuning Layer Thickness”
 Frontiers in Chemistry **6**, 455 (2018)
- [200] J. P. Carlo, T. Goko, I. M. Gat-Malureanu, P. L. Russo, A. T. Savici, A. A. Aczel, G. J. MacDougall, J. A. Rodriguez, T. J. Williams, G. M. Luke, C. R. Wiebe, Y. Yoshida, S. Nakatsuji, Y. Maeno, T. Taniguchi, and Y. J. Uemura
 “New magnetic phase diagram of $(Sr, Ca)_2RuO_4$ ”
 Nature Materials **11**, 323 (2012)
- [201] S. Nakatsuji and Y. Maeno
 “Quasi-Two-Dimensional Mott Transition System $Ca_{2-x}Sr_xRuO_4$ ”
 Phys. Rev. Lett. **84**, 2666 (2000)
- [202] O. Friedt, M. Braden, G. André, P. Adelman, S. Nakatsuji, and Y. Maeno
 “Structural and magnetic aspects of the metal-insulator transition in $Ca_{2-x}Sr_xRuO_4$ ”
 Phys. Rev. B **63**, 174432 (2001)
- [203] Y. Maeno, H. Hashimoto, K. Yoshida, S. Nishizaki, T. Fujita, J. G. Bednorz, and F. Lichtenberg
 “Superconductivity in a layered perovskite without copper”
 Nature **372**, 532 (1994)
- [204] T. M. Rice and M. Sigrist
 “ Sr_2RuO_4 : an electronic analogue of 3He ?”
 Journal of Physics: Condensed Matter **7**, L643 (1995)
- [205] K. Ishida, H. Mukuda, Y. Kitaoka, K. Asayama, Z. Q. Mao, Y. Mori, and Y. Maeno
 “Spin-triplet superconductivity in Sr_2RuO_4 identified by ^{17}O Knight shift”
 Nature **396**, 658 (1998)
- [206] J. A. Duffy, S. M. Hayden, Y. Maeno, Z. Mao, J. Kulda, and G. J. McIntyre
 “Polarized-Neutron Scattering Study of the Cooper-Pair Moment in Sr_2RuO_4 ”
 Phys. Rev. Lett. **85**, 5412 (2000)
- [207] K. Ishida, M. Manago, T. Yamanaka, H. Fukazawa, Z. Q. Mao, Y. Maeno, and K. Miyake
 “Spin polarization enhanced by spin-triplet pairing in Sr_2RuO_4 probed by NMR”
 Phys. Rev. B **92**, 100502 (2015)
- [208] Catherine Kallin
 “Chiral p-wave order in Sr_2RuO_4 ”
 Reports on Progress in Physics **75**, 042501 (2012)

- [209] E. Hassinger, P. Bourgeois-Hope, H. Taniguchi, S. René de Cotret, G. Grissonnanche, M. S. Anwar, Y. Maeno, N. Doiron-Leyraud, and Louis Taillefer
“Vertical Line Nodes in the Superconducting Gap Structure of Sr_2RuO_4 ”
Phys. Rev. X **7**, 011032 (2017)
- [210] Andrew P. Mackenzie, Thomas Scaffidi, Clifford W. Hicks, and Yoshiteru Maeno
“Even odder after twenty-three years: the superconducting order parameter puzzle of Sr_2RuO_4 ”
npj Quantum Materials **2**, 40 (2017)
- [211] Wan-Sheng Wang, Cong-Cong Zhang, Fu-Chun Zhang, and Qiang-Hua Wang
“Theory of Chiral p -Wave Superconductivity with Near Nodes for Sr_2RuO_4 ”
Phys. Rev. Lett. **122**, 027002 (2019)
- [212] H. Won and K. Maki
“Possible f -wave superconductivity in Sr_2RuO_4 ?”
Europhysics Letters (EPL) **52**, 427 (2000)
- [213] A. Pustogow, Yongkang Luo, A. Chronister, Y. -S. Su, D. A. Sokolov, F. Jerzembeck, A. P. Mackenzie, C. W. Hicks, N. Kikugawa, S. Raghu, E. D. Bauer, and S. E. Brown
“Pronounced drop of ^{17}O NMR Knight shift in superconducting state of Sr_2RuO_4 ”
arXiv e-prints, arXiv:1904.00047 (2019)
- [214] Yuan-Chun Liu, Fu-Chun Zhang, Thomas Maurice Rice, and Qiang-Hua Wang
“Theory of the evolution of superconductivity in Sr_2RuO_4 under anisotropic strain”
npj Quantum Materials **2**, 12 (2017)
- [215] D. Sutter, C. G. Fatuzzo, S. Moser, M. Kim, R. Fittipaldi, A. Vecchione, V. Granata, Y. Sassa, F. Cossalter, G. Gatti, M. Grioni, H. M. Rønnow, N. C. Plumb, C. E. Matt, M. Shi, M. Hoesch, T. K. Kim, T.-R. Chang, H.-T. Jeng, C. Jozwiak, A. Bostwick, E. Rotenberg, A. Georges, T. Neupert, and J. Chang
“Hallmarks of Hund’s coupling in the Mott insulator Ca_2RuO_4 ”
Nature Communications **8**, 15176 (2017)
- [216] S. A. Grigera, P. Gegenwart, R. A. Borzi, F. Weickert, A. J. Schofield, R. S. Perry, T. Tayama, T. Sakakibara, Y. Maeno, A. G. Green, and A. P. Mackenzie
“Disorder-Sensitive Phase Formation Linked to Metamagnetic Quantum Criticality”
Science **306**, 1154 (2004)
- [217] Shin-Ichi Ikeda, Yoshiteru Maeno, Satoru Nakatsuji, Masashi Kosaka, and Yoshiya Uwatoko
“Ground state in $\text{Sr}_3\text{Ru}_2\text{O}_7$: Fermi liquid close to a ferromagnetic instability”
Phys. Rev. B **62**, R6089 (2000)
- [218] Shin-Ichi Ikeda, Naoki Shirakawa, Takashi Yanagisawa, Yoshiyuki Yoshida, Shigeru Koikegami, Soh Koike, Masashi Kosaka, and Yoshiya Uwatoko
“Uniaxial-Pressure Induced Ferromagnetism of Enhanced Paramagnetic $\text{Sr}_3\text{Ru}_2\text{O}_7$ ”
Journal of the Physical Society of Japan **73**, 1322 (2004)
- [219] C. Stingl, R. S. Perry, Y. Maeno, and P. Gegenwart
“Symmetry-Breaking Lattice Distortion in $\text{Sr}_3\text{Ru}_2\text{O}_7$ ”
Phys. Rev. Lett. **107**, 026404 (2011)
- [220] A.P. Mackenzie, J.A.N. Bruin, R.A. Borzi, A.W. Rost, and S.A. Grigera
“Quantum criticality and the formation of a putative electronic liquid crystal in $\text{Sr}_3\text{Ru}_2\text{O}_7$ ”
Physica C: Superconductivity **481**, 207 (2012)
- [221] R. A. Borzi, S. A. Grigera, J. Farrell, R. S. Perry, S. J. S. Lister, S. L. Lee, D. A. Tennant, Y. Maeno, and A. P. Mackenzie
“Formation of a Nematic Fluid at High Fields in $\text{Sr}_3\text{Ru}_2\text{O}_7$ ”
Science **315**, 214 (2007)

- [222] A. W. Rost, R. S. Perry, J.-F. Mercure, A. P. Mackenzie, and S. A. Grigera
 “Entropy Landscape of Phase Formation Associated with Quantum Criticality in $\text{Sr}_3\text{Ru}_2\text{O}_7$ ”
Science **325**, 1360 (2009)
- [223] R. S. Perry, K. Kitagawa, S. A. Grigera, R. A. Borzi, A. P. Mackenzie, K. Ishida, and Y. Maeno
 “Multiple First-Order Metamagnetic Transitions and Quantum Oscillations in Ultrapure $\text{Sr}_3\text{Ru}_2\text{O}_7$ ”
Phys. Rev. Lett. **92**, 166602 (2004)
- [224] Daniel O. Brodsky, Mark E. Barber, Jan A. N. Bruin, Rodolfo A. Borzi, Santiago A. Grigera, Robin S. Perry, Andrew P. Mackenzie, and Clifford W. Hicks
 “Strain and vector magnetic field tuning of the anomalous phase in $\text{Sr}_3\text{Ru}_2\text{O}_7$ ”
Science Advances **3**, e1501804 (2017)
- [225] S. A. Grigera, R. S. Perry, A. J. Schofield, M. Chiao, S. R. Julian, G. G. Lonzarich, S. I. Ikeda, Y. Maeno, A. J. Millis, and A. P. Mackenzie
 “Magnetic Field-Tuned Quantum Criticality in the Metallic Ruthenate $\text{Sr}_3\text{Ru}_2\text{O}_7$ ”
Science **294**, 329 (2001)
- [226] R. S. Perry, L. M. Galvin, S. A. Grigera, L. Capogna, A. J. Schofield, A. P. Mackenzie, M. Chiao, S. R. Julian, S. I. Ikeda, S. Nakatsuji, Y. Maeno, and C. Pfleiderer
 “Metamagnetism and Critical Fluctuations in High Quality Single Crystals of the Bilayer Ruthenate $\text{Sr}_3\text{Ru}_2\text{O}_7$ ”
Phys. Rev. Lett. **86**, 2661 (2001)
- [227] C. Lester, S. Ramos, R. S. Perry, T. P. Croft, R. I. Bewley, T. Guidi, P. Manuel, D. D. Khalyavin, E. M. Forgan, and S. M. Hayden
 “Field-tunable spin-density-wave phases in $\text{Sr}_3\text{Ru}_2\text{O}_7$ ”
Nature Materials **14**, 373 (2015)
- [228] A. W. Rost, S. A. Grigera, J. A. N. Bruin, R. S. Perry, D. Tian, S. Raghu, Steven Allan. Kivelson, and A. P. Mackenzie
 “Thermodynamics of phase formation in the quantum critical metal $\text{Sr}_3\text{Ru}_2\text{O}_7$ ”
Proceedings of the National Academy of Sciences **108**, 16549 (2011)
- [229] Y. Tokiwa, M. Mchawat, R. S. Perry, and P. Gegenwart
 “Multiple Metamagnetic Quantum Criticality in $\text{Sr}_3\text{Ru}_2\text{O}_7$ ”
Phys. Rev. Lett. **116**, 226402 (2016)
- [230] D. Sun, A. W. Rost, R. S. Perry, A. P. Mackenzie, and M. Brando
 “Low temperature thermodynamic investigation of the phase diagram of $\text{Sr}_3\text{Ru}_2\text{O}_7$ ”
Phys. Rev. B **97**, 115101 (2018)
- [231] A. Tamai, M. P. Allan, J. F. Mercure, W. Meevasana, R. Dunkel, D. H. Lu, R. S. Perry, A. P. Mackenzie, D. J. Singh, Z.-X. Shen, and F. Baumberger
 “Fermi Surface and van Hove Singularities in the Itinerant Metamagnet $\text{Sr}_3\text{Ru}_2\text{O}_7$ ”
Phys. Rev. Lett. **101**, 026407 (2008)
- [232] B. Binz and M. Sgrist
 “Metamagnetism of itinerant electrons in multi-layer ruthenates”
Europhysics Letters (EPL) **65**, 816 (2004)
- [233] A. M. Berridge
 “Role of band structure in the thermodynamic properties of itinerant metamagnets”
Phys. Rev. B **83**, 235127 (2011)
- [234] A. M. Berridge
 “Thermodynamics of itinerant metamagnetic transitions”
Journal of Physics: Condensed Matter **23**, 094202 (2011)

- [235] B. S. Shivaram, Jing Luo, Gia-Wei Chern, Daniel Phelan, R. Fittipaldi, and A. Vecchione
“Nonlinear Pauli susceptibilities in $\text{Sr}_3\text{Ru}_2\text{O}_7$ and universal features of itinerant metamagnetism”
Phys. Rev. B **97**, 100403 (2018)
- [236] S. Licciardello, J. Buhot, J. Lu, J. Ayres, S. Kasahara, Y. Matsuda, T. Shibauchi, and N. E. Hussey
“Electrical resistivity across a nematic quantum critical point”
Nature **567**, 213 (2019)
- [237] M. Bendele, A. Amato, K. Conder, M. Elender, H. Keller, H.-H. Klauss, H. Luetkens, E. Pomjakushina, A. Raselli, and R. Khasanov
“Pressure Induced Static Magnetic Order in Superconducting FeSe_{1-x} ”
Phys. Rev. Lett. **104**, 087003 (2010)
- [238] L. Balicas, S. Nakatsuji, D. Hall, T. Ohnishi, Z. Fisk, Y. Maeno, and D. J. Singh
“Severe Fermi Surface Reconstruction at a Metamagnetic Transition in $\text{Ca}_{2-x}\text{Sr}_x\text{RuO}_4$ (for $0.2 \leq x \leq 0.5$)”
Phys. Rev. Lett. **95**, 196407 (2005)
- [239] M. E. Barber, A. S. Gibbs, Y. Maeno, A. P. Mackenzie, and C. W. Hicks
“Resistivity in the Vicinity of a van Hove Singularity: Sr_2RuO_4 under Uniaxial Pressure”
Phys. Rev. Lett. **120**, 076602 (2018)
- [240] S. Nakatsuji, D. Hall, L. Balicas, Z. Fisk, K. Sugahara, M. Yoshioka, and Y. Maeno
“Heavy-Mass Fermi Liquid near a Ferromagnetic Instability in Layered Ruthenates”
Phys. Rev. Lett. **90**, 137202 (2003)
- [241] J. Baier, T. Zabel, M. Kriener, P. Steffens, O. Schumann, O. Friedt, A. Freimuth, A. Revcolevschi, S. Nakatsuji, Y. Maeno, T. Lorenz, and M. Braden
“Thermodynamic properties of $(\text{Ca}, \text{Sr})_2\text{RuO}_4$ in magnetic fields”
Physica B: Condensed Matter **378-380**, 497 (2006)
- [242] N. E. Hussey
“Non-generality of the Kadowaki–Woods Ratio in Correlated Oxides”
Journal of the Physical Society of Japan **74**, 1107 (2005)
- [243] B. Burganov, C. Adamo, A. Mulder, M. Uchida, P. D. C. King, J. W. Harter, D. E. Shai, A. S. Gibbs, A. P. Mackenzie, R. Uecker, M. Bruetzam, M. R. Beasley, C. J. Fennie, D. G. Schlom, and K. M. Shen
“Strain Control of Fermiology and Many-Body Interactions in Two-Dimensional Ruthenates”
Phys. Rev. Lett. **116**, 197003 (2016)
- [244] I.M. Lifshitz
“Anomalies of Electron Characteristics of a Metal in the High Pressure Region”
Journal of Experimental and Theoretical Physics **11**, 1130 (1960)
- [245] L. Capogna, A. P. Mackenzie, R. S. Perry, S. A. Grigera, L. M. Galvin, P. Raychaudhuri, A. J. Schofield, C. S. Alexander, G. Cao, S. R. Julian, and Y. Maeno
“Sensitivity to Disorder of the Metallic State in the Ruthenates”
Phys. Rev. Lett. **88**, 076602 (2002)
- [246] A. Karkin, S. Nakatsuji, Y. Maeno, and B. Goshchitskii
“Neutron irradiation effects on anisotropic transport in $\text{Ca}_{2-x}\text{Sr}_x\text{RuO}_4$ ($x = 0.2, 0.5$)”
Physica B: Condensed Matter **378-380**, 492 (2006)
- [247] D. Sutter, M. Kim, C. E. Matt, M. Horio, R. Fittipaldi, A. Vecchione, V. Granata, K. Hauser, Y. Sassa, G. Gatti, M. Grioni, M. Hoesch, T. K. Kim, E. Rienks, N. C. Plumb, M. Shi, T. Neupert, A. Georges, and J. Chang
“Orbitally selective breakdown of Fermi liquid quasiparticles in $\text{Ca}_{1.8}\text{Sr}_{0.2}\text{RuO}_4$ ”
Phys. Rev. B **99**, 121115 (2019)

- [248] Satoru Nakatsuji, Naoki Kiyohara, and Tomoya Higo
“Large anomalous Hall effect in a non-collinear antiferromagnet at room temperature”
Nature **527**, 212 (2015)
- [249] K. Kuroda, T. Tomita, M.-T. Suzuki, C. Bareille, A. A. Nugroho, P. Goswami, M. Ochi, M. Ikhlas, M. Nakayama, S. Akebi, R. Noguchi, R. Ishii, N. Inami, K. Ono, H. Kumigashira, A. Varykhalov, T. Muro, T. Koretsune, R. Arita, S. Shin, Takeshi Kondo, and S. Nakatsuji
“Evidence for magnetic Weyl fermions in a correlated metal”
Nature Materials **16**, 1090 (2017)
- [250] Tomoki Ikeda, Masakiyo Tsunoda, Mikihiro Oogane, Seungjun Oh, Tadashi Morita, and Yasuo Ando
“Anomalous Hall effect in polycrystalline Mn_3Sn thin films”
Applied Physics Letters **113**, 222405 (2018)
- [251] Tomoya Higo, Danru Qu, Yufan Li, C. L. Chien, Yoshichika Otani, and Satoru Nakatsuji
“Anomalous Hall effect in thin films of the Weyl antiferromagnet Mn_3Sn ”
Applied Physics Letters **113**, 202402 (2018)
- [252] Enke Liu, Yan Sun, Nitesh Kumar, Lukas Muechler, Aili Sun, Lin Jiao, Shuo-Ying Yang, Defa Liu, Aiji Liang, Qiunan Xu, Johannes Kroder, Vicky Süß, Horst Borrmann, Chandra Shekhar, Zhaosheng Wang, Chuanying Xi, Wenhong Wang, Walter Schnelle, Steffen Wirth, Yulin Chen, Sebastian T. B. Goennenwein, and Claudia Felser
“Giant anomalous Hall effect in a ferromagnetic kagome-lattice semimetal”
Nature Physics **14**, 1125 (2018)
- [253] Kyoo Kim, Junho Seo, Eunwoo Lee, K.-T. Ko, B. S. Kim, Bo Gyu. Jang, Jong Mok. Ok, Jinwon Lee, Youn Jung. Jo, Woun Kang, Ji Hoon. Shim, C. Kim, Han Woong. Yeom, Byung Il Min, Bohm-Jung Yang, and Jun Sung. Kim
“Large anomalous Hall current induced by topological nodal lines in a ferromagnetic van der Waals semimetal”
Nature Materials **17**, 794 (2018)
- [254] Akito Sakai, Yo Pierre Mizuta, Agustinus Agung Nugroho, Rombang Sihombing, Takashi Koretsune, Michi-To Suzuki, Nayuta Takemori, Rieko Ishii, Daisuke Nishio-Hamane, Ryotaro Arita, Pallab Goswami, and Satoru Nakatsuji
“Giant anomalous Nernst effect and quantum-critical scaling in a ferromagnetic semimetal”
Nature Physics **14**, 1119 (2018)
- [255] Satya N. Guin, Kaustuv Manna, Jonathan Noky, Sarah J. Watzman, Chenguang Fu, Nitesh Kumar, Walter Schnelle, Chandra Shekhar, Yan Sun, Johannes Gooth, and Claudia Felser
“Anomalous Nernst effect beyond the magnetization scaling relation in the ferromagnetic Heusler compound Co_2MnGa ”
NPG Asia Materials **11**, 16 (2019)
- [256] Muhammad Ikhlas, Takahiro Tomita, Takashi Koretsune, Michi-To Suzuki, Daisuke Nishio-Hamane, Ryotaro Arita, Yoshichika Otani, and Satoru Nakatsuji
“Large anomalous Nernst effect at room temperature in a chiral antiferromagnet”
Nature Physics **13**, 1085 (2017)
- [257] Haiyang Yang, Wei You, Jialu Wang, Junwu Huang, Chuanying Xi, Chao Cao, Mingliang Tian, Zhu-An Xu, Jianhui Dai, and Yuke Li
“Giant anomalous Nernst effect in the magnetic Weyl semimetal $\text{Co}_3\text{Sn}_2\text{S}_2$ ”
arXiv e-prints, arXiv:1811.03485 (2018)
- [258] Sarah J. Watzman, Timothy M. McCormick, Chandra Shekhar, Shu-Chun Wu, Yan Sun, Arati Prakash, Claudia Felser, Nandini Trivedi, and Joseph P. Heremans
“Dirac dispersion generates unusually large Nernst effect in Weyl semimetals”
Phys. Rev. B **97**, 161404 (2018)

- [259] Nitesh Kumar, Satya N. Guin, Claudia Felser, and Chandra Shekhar
“Planar Hall effect in the Weyl semimetal GdPtBi”
Phys. Rev. B **98**, 041103 (2018)
- [260] Yoshinori Tokura, Masashi Kawasaki, and Naoto Nagaosa
“Emergent functions of quantum materials”
Nature Physics **13**, 1056 (2017)
- [261] E.I. Gladyshevskii, N.Z. Nakonechna, K. Cenzual, R.E. Gladyshevskii, and J.-L. Jorda
“Crystal structures of $\text{PrAl}_x\text{Ge}_{2-x}$ compounds”
Journal of Alloys and Compounds **296**, 265 (2000)
- [262] Koichi Momma and Fujio Izumi
“*VESTA3* for three-dimensional visualization of crystal, volumetric and morphology data”
Journal of Applied Crystallography **44**, 1272 (2011)
- [263] Su-Yang Xu, Nasser Alidoust, Guoqing Chang, Hong Lu, Bahadur Singh, Ilya Belopolski, Daniel S. Sanchez, Xiao Zhang, Guang Bian, Hao Zheng, Marius-Adrian Husanu, Yi Bian, Shin-Ming Huang, Chuang-Han Hsu, Tay-Rong Chang, Horng-Tay Jeng, Arun Bansil, Titus Neupert, Vladimir N. Strocov, Hsin Lin, Shuang Jia, and M. Zahid Hasan
“Discovery of Lorentz-violating type II Weyl fermions in LaAlGe ”
Science Advances **3**, e1603266 (2017)
- [264] Guoqing Chang, Bahadur Singh, Su-Yang Xu, Guang Bian, Shin-Ming Huang, Chuang-Han Hsu, Ilya Belopolski, Nasser Alidoust, Daniel S. Sanchez, Hao Zheng, Hong Lu, Xiao Zhang, Yi Bian, Tay-Rong Chang, Horng-Tay Jeng, Arun Bansil, Han Hsu, Shuang Jia, Titus Neupert, Hsin Lin, and M. Zahid Hasan
“Magnetic and noncentrosymmetric Weyl fermion semimetals in the RAlGe family of compounds ($R = \text{rare earth}$)”
Phys. Rev. B **97**, 041104 (2018)
- [265] S.K. Dhar, S.M. Pattalwar, and R. Vijayaraghavan
“Magnetic and thermal behavior of CeAlX ($X=\text{Si}$ and Ge) compounds”
Journal of Magnetism and Magnetic Materials **104-107**, 1303 (1992)
- [266] S.K. Dhar and S.M. Pattalwar
“Structural and magnetic properties of $\text{CeAl}_x\text{Si}_{2-x}$ and $\text{CeAl}_x\text{Ge}_{2-x}$ alloys”
Journal of Magnetism and Magnetic Materials **152**, 22 (1996)
- [267] H. Hodovanets, C. J. Eckberg, P. Y. Zavalij, H. Kim, W.-C. Lin, M. Zic, D. J. Campbell, J. S. Higgins, and J. Paglione
“Single-crystal investigation of the proposed type-II Weyl semimetal CeAlGe ”
Phys. Rev. B **98**, 245132 (2018)
- [268] Pascal Puphal, Charles Mielke, Neeraj Kumar, Y. Soh, Tian Shang, Marisa Medarde, Jonathan S. White, and Ekaterina Pomjakushina
“Bulk single-crystal growth of the theoretically predicted magnetic Weyl semimetals RAlGe ($R = \text{Pr, Ce}$)”
Phys. Rev. Materials **3**, 024204 (2019)
- [269] V.K. Anand, Anupam, Z. Hossain, S. Ramakrishnan, A. Thamizhavel, and D.T. Adroja
“Magnetic and transport properties of $\text{Pr}_2\text{Pt}_3\text{Si}_5$ ”
Journal of Magnetism and Magnetic Materials **324**, 2483 (2012)
- [270] P. D. Mitchler, R. M. Roshko, and W. Ruan
“Non-equilibrium relaxation dynamics in the spin glass and ferromagnetic phases of CrFe ”
Philosophical Magazine B **68**, 539 (1993)
- [271] V. K. Anand, D. T. Adroja, and A. D. Hillier
“Ferromagnetic cluster spin-glass behavior in PrRhSn_3 ”
Phys. Rev. B **85**, 014418 (2012)

- [272] G. Kresse and J. Furthmüller
 “Efficient iterative schemes for ab initio total-energy calculations using a plane-wave basis set”
 Phys. Rev. B **54**, 11169 (1996)
- [273] Pramod Kumar, Puneet Jain, and Rachana Kumar
 “Pressure dependent magnetic, AC susceptibility and electrical properties of Nd₇Pd₃”
 RSC Adv. **5**, 58928 (2015)
- [274] Adolfo G. Grushin, Jörn W. F. Venderbos, Ashvin Vishwanath, and Roni Ilan
 “Inhomogeneous Weyl and Dirac Semimetals: Transport in Axial Magnetic Fields and Fermi Arc Surface States from Pseudo-Landau Levels”
 Phys. Rev. X **6**, 041046 (2016)
- [275] S. A. Baily, M. B. Salamon, Y. Kobayashi, and K. Asai
 “Anomalous Hall effect in La_{1-x}Ca_xCoO₃”
 Applied Physics Letters **80**, 3138 (2002)
- [276] Di Xiao, Yugui Yao, Zhong Fang, and Qian Niu
 “Berry-Phase Effect in Anomalous Thermoelectric Transport”
 Phys. Rev. Lett. **97**, 026603 (2006)
- [277] Y. Onose, Lu Li, C. Petrovic, and N. P. Ong
 “Anomalous thermopower and Nernst effect in CeCoIn₅: Loss of entropy current in precursor state”
 Europhysics Letters (EPL) **79**, 17006 (2007)
- [278] Madhav Prasad Ghimire, Jorge I. Facio, Jih-Shih You, Linda Ye, Joseph G. Checkelsky, Shiang Fang, Efthimios Kaxiras, Manuel Richter, and Jeroen van den Brink
 “Creating Weyl nodes and controlling their energy by magnetization rotation”
 arXiv e-prints, arXiv:1903.03179 (2019)
- [279] Hannes Hübener, Michael A. Sentef, Umberto De Giovannini, Alexander F. Kemper, and Angel Rubio
 “Creating stable Floquet-Weyl semimetals by laser-driving of 3D Dirac materials”
 Nature Communications **8**, 13940 (2017)
- [280] Anirudha Menon, Debashree Chowdhury, and Banasri Basu
 “Photoinduced tunable anomalous Hall and Nernst effects in tilted Weyl semimetals using Floquet theory”
 Phys. Rev. B **98**, 205109 (2018)
- [281] Yonghui Zhou, Pengchao Lu, Yongping Du, Xiangde Zhu, Ganghua Zhang, Ranran Zhang, Dexi Shao, Xuliang Chen, Xuefei Wang, Mingliang Tian, Jian Sun, Xiangang Wan, Zhaorong Yang, Wenge Yang, Yuheng Zhang, and Dingyu Xing
 “Pressure-Induced New Topological Weyl Semimetal Phase in TaAs”
 Phys. Rev. Lett. **117**, 146402 (2016)

